Molecular simulation method development and implementation for fuel cell catalyst layers

Peter Vanya
Magdalene College
University of Cambridge

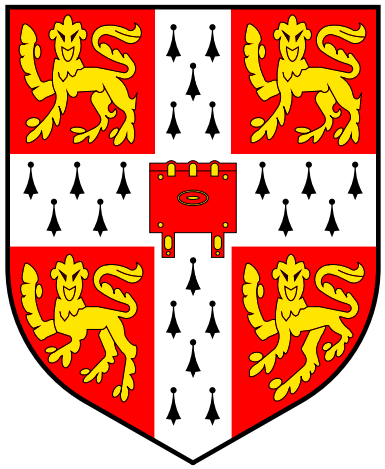

The thesis submitted for the degree of
Doctor of Philosophy
September 2018
Supervisor: Prof James Elliott

Preface

This thesis is the result of my own work and includes nothing which is the outcome of work done in collaboration except as declared in the Preface and specified in the text.

It is not substantially the same as any that I have submitted, or, is being concurrently submitted for a degree or diploma or other qualification at the University of Cambridge or any other University or similar institution except as declared in the Preface and specified in the text. I further state that no substantial part of my dissertation has already been submitted, or, is being concurrently submitted for any such degree, diploma or other qualification at the University of Cambridge or any other University or similar institution except as declared in the Preface and specified in the text.

The work does not exceed 60k words, including tables, footnotes, bibliography and appendices, but excluding photographs and diagrams.

Peter Vanya
Cambridge, Summer 2018

Abstract

Good is the enemy of perfect.

Voltaire, probably.
The motto of this thesis.

This thesis attempts to bridge science with technology applications by developing two lines of research, one theoretical and one practical.

On the practical side, we describe the microscopic behaviour of a fuel cell, specifically a catalyst layer where the oxygen reduction reaction (ORR) takes place. The processes taking place in the catalyst layer are inefficient at ambient conditions and so this fuel cell component is, together with high price of platinum as the catalyst, the main bottleneck inhibiting large-scale deployment of fuel cell electric vehicles and competition with internal combustion engines. There has been an ongoing debate in the literature about the resistance in the catalyst layer the origin of which is unknown and exact microscopic mechanism not properly understood. The candidate causes include not only the catalysis of the ORR on the surface of platinum nanoparticles, but also the thin ionomer film inhibiting mass transport of protons, oxygen or water.

The aim of this thesis is to understand the structure of thin ionomer films in the catalyst layer. To this end, we employ mesoscale dissipative particle dynamics (DPD), a well-established coarse-grained molecular dynamics method, to model such thin film confined from both sides. Our results summarised in Chapter 2 reveal a confinement-induced water clustering as well as a diffusivity anisotropy increasing with decreasing film thickness, confirming that the behaviour of a thin film is significantly different from the bulk membrane. The percolation network of water clusters and channels in the ionomer film is strongly dependent on the hydrophobicity of the confining material.

In Chapter 3, we return to the bulk membrane and explore using DPD its structure and behaviour under different preparation paths. These results enable us to address the experiments by Gebel [1] and update this author's proposed microscopic models.

On the theory side, having realised that currently available computational methods such as DPD were inadequate for simulating truly realistic settings in the catalyst layer on the scale of tens of nanometres, in Chapter 6 we present our work on many-body dissipative particle dynamics (MDPD), a method suitable for simulating porous environments but so far poorly understood and impossible to apply to real systems. By varying a wide range of input parameters we uncover a rich phase diagram and devise a top-down parametrisation method based on compressibility and surface tension that enables to capture the correct behaviour of real liquids

as well as mixtures. We thoroughly discuss the role of coarse-graining degree as a simulation input and present a way to adjust simulation parameters in order to consistently predict material properties across scales. Testing on a few simple mixtures yields reasonable agreement with experiment.

Besides our work on MDPD, we revisit some of the older theory behind standard DPD. In Chapter 4, we restate the role of reduced units in a clearer manner and rederive the temperature dependence of the interaction parameter. We also explain in general terms how simulation inputs need to be adjusted with respect to coarse-graining degree in order to make the outputs, which are compared with experiment, invariant across scales. In Chapter 5 we present an attempt to develop a bottom-up parametrisation for standard DPD based on clustering molecules and matching radial distribution functions. In the present form, this work should be viewed as a playground for ideas rather than a proven simulation tool.

Finally, to demonstrate the power of MDPD, in Chapter 7 we apply the newly developed parametrisation method to an unconfined thin Nafion film with free space on one side, a setting inaccessible by standard DPD. These simulations should provide a more reliable view on the structure of the thin ionomer film in the catalyst layer. We find out that films of thickness of 5 nm or less cannot accommodate water inside and, as a result, have hydrophilic outer surfaces. Surface hydrophobicity increases with film thickness and decreases with water content, with important consequences for fuel cell operation.

Some chapters of this thesis are based on the following manuscripts published in or submitted to journals.

I. Vanya, Sharman and Elliott: Mesoscale simulations of confined Nafion thin films.

   The Journal of Chemical Physics 147, 214904, 2017, doi:10.1063/1.4996695. Chapter 2.

II. Vanya, Crout, Sharman and Elliott: Liquid phase parametrisation and solidification in many-body dissipative particle dynamics.

   Physical Review E 98, 033310, 2018, doi:10.1103/PhysRevE.98.033310. Chapter 5.

III. Vanya, Sharman and Elliott: Invariance of experimental observables with respect to coarse-graining in standard and many-body dissipative particle dynamics.

   The Journal of Chemical Physics 150, 064101, 2019, doi:10.1063/1.5046851. Chapters 3 and 5.

Acknowledgments

Writing a thesis makes one fall for a cognitive dissonance. On one hand, one cannot escape the feeling that only four people in the world will ever read it, including myself and my supervisor, so what is the point. It looks like a grim prospect, but one has simply has to do it in order to move on with life. On the other hand, one wants to do a good job for the sake of it, produce something worth reading.

Notwithstanding this internal debate, I absolutely appreciate the importance of the acknowledgements section. Firstly, one can write here (almost) whatever one has in mind. A PhD is a struggle, and there many are things to write about besides pure science. Secondly, research showed that keeping a gratitude journal makes one more happy;[1] consider this a condensed version. Thirdly, this is an important opportunity to look back and think about how one got where one happens to be, who and what mattered in his life and also who or what did not. After the manuscripts have been submitted and some of them even published, I regard the acknowledgements the most important part of the thesis.

For the start, I gratefully acknowledge financial support from EPSRC, Johnson Matthey and Sir Colin Corness scholarship of Magdalene College.

On the academic side, first and foremost I would like to thank my supervisor James for plenty of support and space for independent exploration. It is extremely important to be on the same wavelength with one's manager, and I consider myself lucky to be guided by James. Secondly, I am grateful to my industrial supervisors from Johnson Matthey, Jonathan Sharman and Dash Fongalland, for many fruitful conversations and patience with my sometimes slow progress. Our common meetings always left me full of inspiration and enthusiasm. Thirdly, I benefited from interactions with my colleagues, notably Patrick Kiley. Patrick knows answers to (almost) every question, either computational, experimental, on food, general biology, or poo. Furthermore, Thurid, Andrew, Georg, Chunlei, Geronimo, Cezar, Angelika, Chris, Adarsh, Alan and other colleagues made our morning coffees at 11:23am a pleasant start of the day.

In my research, the vast majority of software I used was open-source, essentially free to download. I would like to thank the people who keep writing and updating wonderful projects such as Linux, Python and its libraries, and specialised scientific packages such as LAMMPS.

Outside of my immediate work, I am especially indebted to Jan Hermann. Being both an exquisite scientist and a kind person, Honza always patiently listened to my frequent technical questions and was also able to answer them. He has been massively contributing to my education since we have known each other, since I met him at 17. Fortran, Python, Unix, Mathematica,

[1] https://80000hours.org/career-guide/how-to-be-successful/

parallelisation, data structures, DFT and many-body theory are a few of the topics with which I annoyed him nearly every day. Furthermore, Ľuboš, Ondrej and Boris provided the right blend of highly intellectual and utterly profane conversations. I thank Boris for interesting discussions on chemistry and impact[2] and Christine for our friendship.

Besides academia, sport is an unacknowledged simulator of life in defining goals, achieving them, failing, getting frustrated and processing pain. I was fortunate to be part of the first men's boat of Magdalene Boat Club coached by George Wallace, who, albeit only 20 years old, showed remarkable leadership and will to excel, which I was inspiring. Dedicating at times about 20 hours per week to rowing, I learned a few important things about myself.[3] I also thank Perran Ziar, our senior coach, for his kindness and sacrifice.

Looking deeper into my history, I think my family is probably the most important reason for where I am in life. My parents, grandparents, and my aunt had gently pressed me for academic performance since early age and always supported my aspirations, even if it meant leaving home at 16. Having gained a perspective by emigrating to a more developed country and meeting people from all around the world, I do not take this for granted any more.

I also thank Aranka for cultivating me, perhaps making me less aggressive, and certainly more punctual. On average at least.

Finally, I am grateful to people who keep the European Union project running.

[2] An important management consulting concept, or so he says, having left academia for McKinsey.
[3] For example, I will never ever want to become a professional sportsman.

Abbreviations

ICE	internal combustion engine
FCEV	fuel cell electric vehicle
BEV	battery electric vehicle
FC	fuel cell
PEMFC	proton exchange membrane fuel cell
PFSA	perfluorosulfonic acid
ORR	oxygen reduction reaction
PGM	platinum group metal
NP	nanoparticle
DFT	density functional theory
MD	molecular dynamics
DPD	dissipative particle dynamics
MDPD	many-body dissipative particle dynamics
SPC	simple point charge
GW	Groot and Warren
WSG	Wijmans, Smit and Groot
CG	coarse-graining
LJ	Lennard-Jones
EOS	equation of state
PBC	periodic boundary conditions
CN	coordination number
RDF	radial distribution function
CoM	centre of mass
RMSE	root-mean square error
SAXS	small angle X-ray scattering
NMR	nuclear magnetic resonance
FP	first-peak
MO	maximum-overlap

Contents

Chapter 1

Introduction

> Falling in love with a woman like you
> happens so quickly, there's nothing to do
> it's only natural
> but why did it have to be me?
>
> *ABBA*

1.1 Motivation

The fragile existence of human life on earth is permanently in danger. Historically, most serious threats were natural risks, such as extreme droughts, colds, or epidemics. However, the greatest problems of the past century as well as the future are due to human activity. As of 2017, there are several rankings of the most pressing problems humanity has to solve in order to survive. For example, the non-profit organisation 80000 hours has compiled the list in Table 1.1.[1] A (less ambitious) alternative is made by the World Economic Forum.[2]

Some of these problems are political, meaning that the path towards the solution would involve access to and persuasion of someone elected, either directly or through a massive campaign. In other cases, deep thought along scientific lines would help. This is where natural sciences and mathematics can significantly contribute towards the solutions. For example, the risk from artificial intelligence comes from our current inability to explain to computers the meaning of human life and the need to protect it, which stems from unsatisfactory understanding of how deep neural networks process inputs.[3] Similarly, factory farming is an important moral as well as environmental concern resulting from current incapability to produce cheap and tasty enough artificial meat. Biochemical research should help achieve this ambitious target.

One of the pre-eminent problems for the 21st century is climate change, which has been, as of 2018, unambiguously proved to be the result of human activity in the past 200-300 years, or since the industrial revolution ushered in steam engines and coal burning.[4]

Each year, the world economy releases huge amounts of CO_2 and other gases even more potent than CO_2 into the atmosphere. In 1990, it was 22 gigatons, in 2015 it was 36 and this

[1] https://80000hours.org/articles/cause-selection/
[2] Available on Business Insider
[3] https://waitbutwhy.com/2015/01/artificial-intelligence-revolution-1.html
[4] A nice visualisation: https://www.bloomberg.com/graphics/2015-whats-warming-the-world/

Problem	Score
Risks from artificial intelligence	27
Promoting effective altruism	26
Global priorities research	26
Improving institutional decision-making	24
Factory farming	23
Biosecurity	23
Nuclear security	23
Developing world health	21
Climate change (extreme risks)	20
Land use reform	20
Smoking in the developing world	20

Table 1.1: Most urgent global issues according to 80000 hours (source: see Footnote 1).

number is expected to rise, as emerging economies, such as India, keep emerging.[5] As a result, the International Panel on Climate Change estimates that the atmosphere is expected, according to the worst-case scenario, to warm up by 2.6 to 4.8 °C.[6] The consequences for humanity could be disastrous, including severe food and freshwater shortages and massive spread of infections.

An important, if not the only source of CO_2 in the atmosphere, is burning of fossil fuels, which is key to provide transport, electricity and heat production for households and industry, and consumer goods. Hence, the challenge to find sustainable sources of energy has been at the forefront of scientific interest. Currently, fossil fuels form a massive part to the energy production amounting to 87% in 2015 and their overall consumption keeps rising,[7] so any significant reduction in the near future looks like a utopia. However, it has already been demonstrated by back of the envelope calculations how it might be possible to significantly reduce energy from fossil fuels in the United Kingdom, not even accounting for expensive nuclear energy.[8]

In the field of transport, a promising technology is fuel cells (FC). This simple mechanism to convert chemical energy to electricity and, finally, to kinetic energy, is, together with batteries, expected to supersede internal combustion engines (ICEs) and revolutionise the transport industry.

1.1.1 Hydrogen fuel cells

Broadly speaking, there are several types of fuel cells, which use different fuels and operate at different temperatures. An everyday example is a breathalyser for estimating blood alcohol content, where ethanol is the fuel and the resulting voltage can be related to the amount of alcohol in blood. Most suitable for transport purposes are proton exchange membrane fuel cells (PEMFC, also called polymer electrolyte membrane fuel cells), operating below 100 °C, which

[5] The progress can be viewed here: http://edgar.jrc.ec.europa.eu/overview.php?v=CO2ts1990-2015
[6] See pages 89-90 in the IPCC 2015 report.
[7] See pages 2-5 in the BP statistical review.
[8] David MacKay: Without hot air. Freely available at https://www.withouthotair.com/

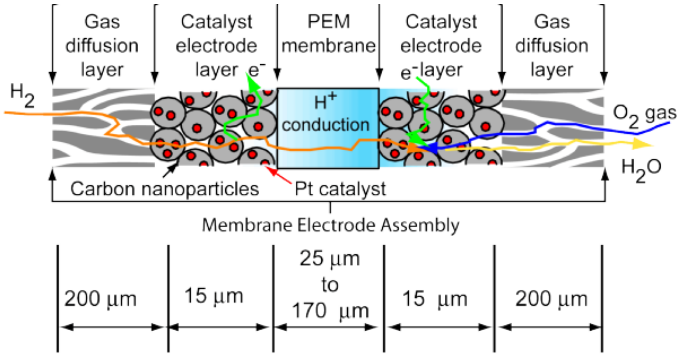

Figure 1.1: A scheme of a proton exchange membrane fuel cell showing the membrane with electrodes and the gas diffusion layer on both sides. Source: Carbon Trust.

use hydrogen as the fuel. On the anode, hydrogen molecules are split into protons and electrons:

$$2H_2 \rightarrow 4H^+ + 4e^-, \tag{1.1}$$

The protons then migrate through the polymer membrane. After arriving at the cathode, they meet with oxygen from air on the surface of a catalytic nanoparticle from a precious metal, most often platinum, and form water which leaves the system. This process is known as the oxygen reduction reaction (ORR):

$$O_2 + 4H^+ + 4e^- \rightarrow 2H_2O. \tag{1.2}$$

The operation of fuel cell electric vehicles (FCEVs) produces zero emissions (only water) and so this technology is a perfect candidate for superseding internal combustion engines in order to meet the target to cut the CO_2 emissions by 80% by 2050. The production of hydrogen is thus the only source of CO_2. This is discussed in the following sections.

The key advantages of FCEVs are fast refuelling in the order of minutes, comparable with ICEs and in contrast to battery electric vehicles (BEVs), and the driving range rivalling ICEs and by far superseding that of the BEVs. Hence, this technology is ideal for long-haul transport of goods (trucking), which accounts for a significant portion of emissions and which cannot afford for economic reasons long refuelling stops. Under an optimistic scenario, FCEVs could cover as much as 50% of the transport market, the rest being split into BEVs, plug-in hybrids and ICEs.[9]

1.1.2 Practical challenges

To make FCEVs competitive, several obstacles need to be overcome. The most important one is price, which is, as of 2018, still relatively high compared to alternatives. The primary cause is the high price of platinum-group-metals (PGM) used as a catalyst for the ORR. Cost is considered the main driver of mass adoption and the cause of the current (2018) rather limited traction of FCEVs.[10] Secondly, the hydrogen infrastructure is still incomparably sparse compared with the network of conventional petrol stations or battery charging points.

[9] See Fig. 6 in the McKinsey report available at http://www.eesi.org/files/europe_vehicles.pdf
[10] See this FT opinion (under paywall).

Hydrogen production and distribution

An important obstacle in mass deployment of FCEVs in transport is the production and distribution of hydrogen as the fuel. In 2012, about 60bn kg of hydrogen were produced annually, and this number is expected to rise roughly twofold if a significant portion of the vehicle market will be covered by FCEVs. This brings about new challenges in production scaling.[11]

Currently, about 95% of hydrogen is produced via steam-methane reforming.[12] This process requires temperature of 700-1100 °C, pressure of 3-25 bar, and nickel as a catalyst, and involves two steps. Firstly, steam-methane reforming reaction (endothermic, $\Delta H = 205$ kJ/mol):

$$\mathrm{CH_4 + H_2O \rightarrow CO + 3H_2}, \tag{1.3}$$

and, secondly, water-gas shift reaction (exothermic, $\Delta H = -41$ kJ/mol):

$$\mathrm{H_2O + CO \rightarrow CO_2 + H_2}. \tag{1.4}$$

Clearly, this production route requires natural gas and so is not a clean technology per se. Hence, a gradual transition to alternative routes, such as water electrolysis, is anticipated, assuming electricity would come from renewable sources.[13] Alternatively, in the future the CO_2 from reforming might be captured and stored, or converted to some industrially useful product.

Price of the catalyst

The ORR in a fuel cell, in which the protons, electrons and oxygen from air meet to produce water, requires catalysts for full performance. This process is inherently inefficient due to the relatively low temperature and pressure (compare with the steam-methane reforming conditions above). Hence, expensive PGMs need to be used. (Fig. 1.2 shows the prices of precious metals.) To make FCEVs competitive in terms of price, it is key to figure out how to (i) reduce the amount of catalyst required for smooth operation, or (ii) find alternative metals or alloys delivering similar performance at reduced cost.

The most common catalyst used in FCEVs today is platinum (Pt). The price of a gram of Pt is 29.6 USD, only about 30% less than the price of gold.[14] Currently, one FCEV requires about 17 g of Pt; in order to compete with ICEs, this number should fall to 4 g.[15]

Only 150 tonnes of platinum are mined annually, and estimated world reserves are at 30000 tonnes.[16] Assuming about only 10 g of Pt per vehicle and annual production of 37 million of FCEVs around 2050, this would require mining 370 tonnes of Pt per year for this purpose only. Besides increasing the mining rate, Pt from the used FCEVs would have to be recycled.

Having described the challenges in FCEV mass deployment, we now discuss how computer modelling can help addressing them.

[11] For more information, see the report by the Carbon Trust.
[12] https://www.energy.gov/eere/fuelcells/hydrogen-production-natural-gas-reforming
[13] https://www.energy.gov/eere/fuelcells/hydrogen-production-electrolysis
[14] Source: Money Metals Exchange, accessed 4 April 2018.
[15] Source Carbon Trust.
[16] PGM market report, May 2017.

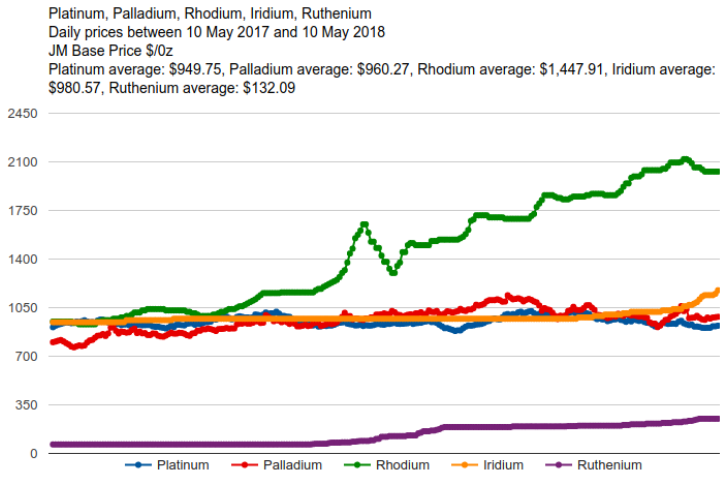

Figure 1.2: The price of platinum and other precious metals in the past year from 10 May 2018. The price units are USD/ounce, where an ounce is equal to 28.34 g. Source: http://www.platinum.matthey.com/prices/price-charts

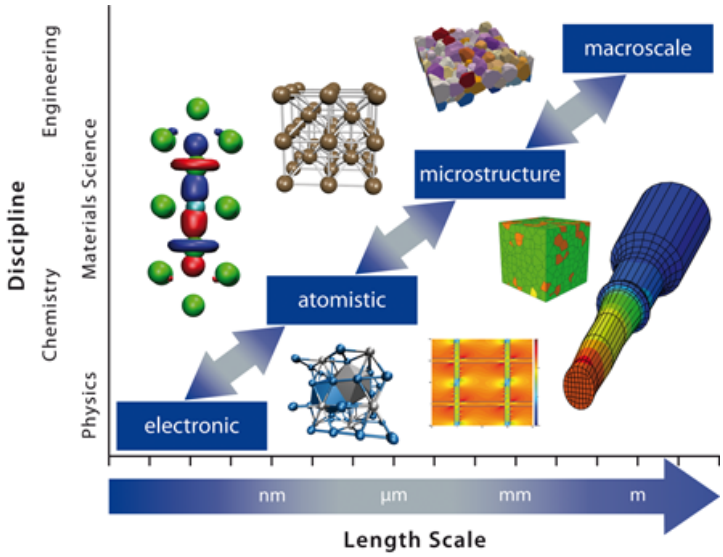

Figure 1.3: A bird's-eye view of materials methods, from electronic structure up to the continuum. Source: http://www.icams.de/content/research/

1.2 The role of computer modelling

Computer simulations can provide insight into microscopic mechanisms at a fraction of cost and time required for experiments. Over the past decades, an immense number of methods has been developed to cover a wide range of length and time scales and levels of precision. There is a well-established hierarchy of computational methods in physics, chemistry, material science and engineering, ranging from those able to capture at a few atoms, through aerodynamics describing flows around airplanes, up to schemes to model galactic evolution. Here, we briefly describe the methods applied in the microscale.

1.2.1 Quantum

The aim is to obtain as precise picture about the behaviour of a system as possible. Starting from the theoretical bottom, many-body electronic states governed by a certain effective Hamiltonian[17] occupy the Fock space. The Hamiltonian can be expressed as a matrix in this space and diagonalised to obtain exact ground and excited states,[18] a process known as exact

[17] The best example of such Hamiltonian is the Hubbard model.
[18] Exact within the given basis. In practice, the basis of, e.g., a hydrogen atom, is infinite.

diagonalisation.

Due to exponential scaling, current state-of-the-art exact diagonalisation simulations on largest computer clusters can accommodate up to 50 atoms. More benevolent and approximate is density-matrix renormalisation group (DMRG), which now also starts to appear in chemistry.[19]

To generate more practical results, one has to resort to all sorts of approximations. Quantum chemistry offers a wide range of methods, starting from the mean-field Hartree-Fock theory, which does not account for electron correlation due to Coulomb repulsion, up to coupled cluster (CC) and configuration interaction (CI), which an adjusted form of exact diagonalisation. The scaling of these methods, N^6 to N^8 for CC and N^6 to N^{10} for CI with the number of orbitals (electronic states) N, is still unfavourable for systems of about 100-1000 atoms, and so both of these have very limited use in practical simulations.

To capture real material properties and potentially sample the phase space to compute entropy and free energy, one needs to reject these wavefunction methods and resort to density functional theory (DFT), which scales as N^3. However, even DFT is expensive and systems of 100-1000 atoms are accessible only on supercomputers, especially if dynamics is involved.

1.2.2 Molecular dynamics via force fields

To overcome the computational expense of these ab initio (quantum) methods and get enough sampling, either in the form of the number of particles (atoms or electrons) or simulation time (amount of phase space visited), atomistic force fields are the next step. For each particle i, which interacts with its neighbours j via a pre-defined potential $V(r)$, the dynamics is generated by simply solving Newton's equations:

$$m\mathbf{a}_i = -\sum_{j\neq i} \nabla_i V(r_{ij}). \tag{1.5}$$

The function $V(r)$ is expected to capture the van der Waals attraction at longer scales and Pauli repulsion at shorter scales, as well as bond, angle, and dihedral/torsional interactions to represent chemical bonds. Most common force fields are shown in Table 1.2.

A typical number of atoms in a MD simulation using force fields is 10k-100k, timestep is 1 fs, and simulation time several ns. This can be achieved on computers of several cores, and it is possible to scale up to millions of atoms on supercomputing clusters.

1.3 Coarse-graining and dissipative particle dynamics

To target even larger length and time scales than those allowed by the classical MD, we need to resort to coarse-graining, which means grouping a few atoms or molecules and evolving these as an effective particle via Newton's equations. A popular representative, on which the research in this thesis is built, is dissipative particle dynamics (DPD), which uses soft potentials and the bead-spring model of polymers to accelerate the dynamics.

In DPD, a few molecules are packed at the start of the simulation into a particle (*bead*),

[19] For example: arxiv:1407.2040.

Type	Name	Potential energy $V(r)$
Pair	Lennard-Jones	$4\epsilon\left[\left(\frac{\sigma}{r}\right)^{12}-\left(\frac{\sigma}{r}\right)^{6}\right]$
	Buckingham	$Ae^{-r/\rho}-\frac{C}{r^6}$
Pair many-body	EAM	$V_i = f_\alpha(\sum_{j\neq i}\rho_\beta(r_{ij})) + \frac{1}{2}\sum_{j\neq i}\phi_{\alpha\beta}(r_{ij})$
	Tersoff	[Complex]
Bond	Harmonic	$k(r-r_0)^2$
	Morse	$D(1-e^{a(r-r_e)})^2$
	FENE	$-\frac{1}{2}K\Delta r_{\max}^2 \ln\left[1-\left(\frac{r-r_0}{\Delta r_{\max}}\right)^2\right]$

Table 1.2: Most common force fields for pair and bond interactions. Standard sources: [2, 3].

and these beads are made to interact via a quadratic potential with cutoff r_c:

$$V(r) = \begin{cases} \frac{ar_c}{2}\left(1-\frac{r}{r_c}\right)^2, & r \leq r_c, \\ 0, & r > r_c. \end{cases} \tag{1.6}$$

This simple force field is controlled by only one parameter, a, in the case where the reduced units $r_c = 1$ are used.

First introduced by Hoogerbrugge and Koelman to simulate suspension flows for the petroleum industry [4, 5], DPD was subsequently theoretically substantiated by Español and Warren, who linked it to the Fokker-Planck equation and the fluctuation-dissipation theorem [6]. The most influential contribution is by Groot and Warren (GW) [7], who slightly reformulated DPD and demonstrated how to apply it to soft matter systems by developing a protocol for calculating interaction parameters between like particles from compressibility and those between unlike particles from the Flory-Huggins theory. Later, it was demonstrated that DPD is capable of preserving hydrodynamics [8].

In the past 20 years since the appearance of the GW paper, DPD has been extensively applied to multiple families of soft matter systems, most static [9] and dynamic properties of polymers [10], phases of block copolymers [11], surfactant solutions [12, 13], and ionomer membranes [11, 14, 15, 16, 17, 18, 19, 20, 21, 22, 23, 24, 25]. For a more thorough summary of the method we recommend the reviews [26, 27].

1.3.1 The DPD force field

As mentioned above, the key idea behind the fast dynamics of DPD is to combine a few molecules into a bead. For simplicity, beads have approximately the same mass m and diameter r_c. Then we can define reduced units $r_c = 1, m_c = 1, k_B T_c = 1$, where T_c is some chosen reference temperature, e.g. 300 K. The conservative force between beads derived from eq. (1.6) is:

$$\mathbf{F}^C(\mathbf{r}_{ij}) = \begin{cases} a(1-r)\hat{\mathbf{r}}_{ij}, & r \leq 1, \\ 0, & r > 1, \end{cases} \tag{1.7}$$

where $\mathbf{r}_{ij} = \mathbf{r}_i - \mathbf{r}_j$, $r = |\mathbf{r}_{ij}|$ is the distance, $\hat{\mathbf{r}}_{ij} = \mathbf{r}_{ij}/r$ is the unit vector in the direction of the interaction, and a is the only interaction parameter. This force is complemented with a Langevin-type thermostat providing a dissipative and a random force:

$$\mathbf{F}^{\mathrm{D}}(\mathbf{r}_{ij}) = -\gamma w(r)^2(\hat{\mathbf{r}}_{ij} \cdot \mathbf{v}_{ij})\hat{\mathbf{r}}_{ij}, \tag{1.8}$$

$$\mathbf{F}^{\mathrm{R}}(\mathbf{r}_{ij}) = \sigma w(r)\frac{\theta}{\sqrt{\Delta t}}\hat{\mathbf{r}}_{ij}, \tag{1.9}$$

where γ is the friction parameter, σ the noise parameter, $\mathbf{v}_{ij} = \mathbf{v}_i - \mathbf{v}_j$ a mutual velocity, θ a Gaussian random number with zero mean and unit variance, i.e. $\theta \in \mathcal{N}(0,1)$, and Δt a simulation time step. The term $\theta\sqrt{\Delta t}$ represents the Wiener process [28].

There is a freedom to choose the weight function $w(r)$ in the dissipative and random term [6]. For simplicity, a linear function has always been chosen:

$$w(r) = \begin{cases} (1-r), & r < 1, \\ 0, & r \geq 1. \end{cases} \tag{1.10}$$

Hence, the conservative potential between the beads in reduced units is quadratic:

$$V(r) = \begin{cases} a(1-r)^2\,/\,2, & r < 1, \\ 0, & r \geq 1, \end{cases} \tag{1.11}$$

σ and γ are essentially a single quantity, as they are related via the fluctuation-dissipation theorem, a general feature of all thermodynamic systems: $\sigma = \sqrt{2\gamma k_{\mathrm{B}}T}$. In practice, σ is chosen to be 3, and setting $k_{\mathrm{B}}T = 1$ yields $\gamma = 4.5$.[20]

To simulate polymers, one can add bonds between beads and thus obtain a bead-spring model. A common example of a chemical bond is a harmonic spring:

$$\mathbf{F}^{\mathrm{B}}_{ij} = -k(r - r_0)\hat{\mathbf{r}}_{ij}. \tag{1.12}$$

where k is stiffness and r_0 equilibrium distance. Sometimes, angular terms are used as well [29].

The dynamics is then generated from the Newton's equation of motion:[21]

$$\frac{d\mathbf{v}_i}{dt} = \sum_{i \neq j} \mathbf{F}^{\mathrm{C}}_{ij} + \mathbf{F}^{\mathrm{D}}_{ij} + \mathbf{F}^{\mathrm{R}}_{ij} + \mathbf{F}^{\mathrm{B}}_{ij}. \tag{1.13}$$

Equilibrium properties

As mentioned above, DPD preserves hydrodynamics, i.e. the motion of beads follows the Navier-Stokes equations. This is an important advantage over e.g. the Brownian dynamics as another representative of coarse-grained methods [8]. On the other hand, a well-understood disadvantage of DPD, and soft potentials in general, is inaccurate prediction of dynamic quantities, such as the self-diffusivity [26]. We will provide a more thorough investigation of the dynamic behaviour

[20] Since in practice $k_{\mathrm{B}}T = 1$ is always used, we will henceforth refer to γ only and save the letter σ for surface tensions.

[21] There is no mass in the equation, since all particle masses are approximately equal to the mass scale, $m_{\mathrm{c}} = 1$.

in Chapter 4.

GW showed that the DPD potential leads to the quadratic equation of state (EOS), which holds for number densities $\rho > 3$ (setting $k_\mathrm{B}T$ to $k_\mathrm{B}T_\mathrm{c} = 1$):

$$p = \rho + \alpha a \rho^2, \tag{1.14}$$

where $\alpha = 0.101$ is a fitting constant.

To ensure that the simulated liquid corresponds to the experiment, the interaction parameter a is derived from compressibility defined as $\kappa = -1/V(\partial V/\partial p)_T$ [7], which can be derived from the EOS:

$$\kappa^{-1} = \rho \left(\frac{\partial p}{\partial \rho} \right)_{N,T} = \rho + 2\alpha a \rho^2. \tag{1.15}$$

Hence:

$$a = \frac{\kappa^{-1} - \rho}{2\alpha\rho^2}, \tag{1.16}$$

where κ^{-1} is experimental compressibility[22] of the simulated liquid. Considering, e.g., water, for which $\kappa = 4.54 \times 10^{-10}$ Pa^{-1}, yields $a = 25$ in reduced units.

On top of the usual parameters to fine-tune the simulations, such as repulsion a and friction γ, CG simulations offer another freedom, which is the number of atoms/molecules. This CG degree offers a trade off between speed and spatial or temporal resolution. However, since this is only a theoretical construct, measurable quantities, such as temperature, pressure or compressibility, must remain invariant with respect to it.

In DPD, this has been a topic of discussion for years. Finally, Füchslin *et al.* [30] have shown that all simulation parameters remain scale-invariant in reduced units, i.e. if water serves as the solvent, $a = 25$ should always be used regardless of the number of molecules in a bead. CG degree only affects the way the quantities of interest are converted to the SI units after the simulation.

Mixtures in DPD

The derivation of cross interaction terms Δa_{ij} between unlike beads representing specific materials is based on the framework of the Flory-Huggins theory [31, 32]. GW showed that the EOS can be matched to this theory [7], and derived that the relationship between excess repulsion Δa depends approximately linearly on the χ-parameter, a universal property of mixtures, at density $\rho = 3$ and in the regime when $2 < \chi < 10$ covering common mixtures:

$$\Delta a = 3.27\chi. \tag{1.17}$$

This approximation was further improved on by Wijmans *et al.* [33], who used a slightly more precise quadratic fit. Furthermore, this coefficient of proportion increases with the density.

The scaling of Δa with the CG degree N_m has so far been unresolved. We derived (see Chapter 4) that, in order to keep the surface tension scale-invariant, the χ-parameter must

[22] Note that inverse compressibility is in fact the bulk modulus.

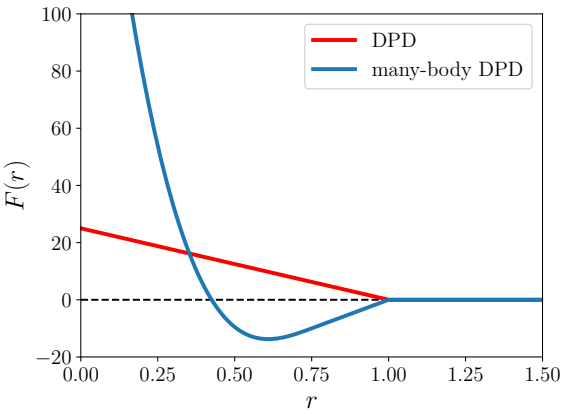

Figure 1.4: Comparison of standard and many-body DPD force fields for two isolated particles with parameters $a = 25$ and $A = -40, B = 25$ respectively. The many-body DPD force field has a local density term, so in case of a liquid the repulsion would be even higher due to increased value of the local densities.

scale as:

$$\chi(N_\mathrm{m}) = \chi(1)N_\mathrm{m}^{-0.2} \tag{1.18}$$

Several ways to calculate the χ-parameter for a specific mixture have been proposed and tested. Common choices are a simple relation based on molar volume V_m and Hildebrand solubility parameters δ_i, where i denotes species:

$$\chi_{ij} = \frac{V_\mathrm{m}}{RT}(\delta_i - \delta_j)^2. \tag{1.19}$$

An alternative is a more complex Monte Carlo sampling developed by Fan *et al.* [34] and applied in [17, 14].

In conclusion, DPD is a very simple but powerful method to efficiently simulate soft matter systems. Unfortunately, due to its purely repulsive force field, it cannot simulate multiphase environments and porous structures, such as the catalyst layer of a fuel cell. To overcome this deficiency, we now introduce a modified version of DPD.

1.4 Many-body dissipative particle dynamics

Since the inception of DPD there has been a motivation to modify it to describe a wider range of phenomena, such as the liquid-vapour coexistence. The result is the many-body version of DPD.

First presented by Pagonabarraga *et al.* and Trofimov *et al.* [35, 36] and thoroughly explored by Warren [37], the many-body DPD (MDPD) builds on top of the classical DPD by adding a density-dependent interaction with a different length cutoff $r_\mathrm{d} < 1$. This modification leads to an EOS with a van der Waals loop, which enables the formation of a liquid-vapour interface and increases the applicability to free surfaces. Compared with standard DPD, which allows only repulsive interactions resulting in gas-like behaviour of spreading to the whole simulation cell, MDPD, which has an additional attractive force term, can support simulations in which the bead density varies widely across the cell.

Adopting again reduced units $r_\mathrm{c} = m_\mathrm{c} = k_\mathrm{B}T_\mathrm{c} = 1$, as in standard DPD, the MDPD force field is:

$$\mathbf{F}_{ij}(\mathbf{r}_{ij}) = Aw(r_{ij})\hat{\mathbf{r}}_{ij} + B(\bar{\rho}_i + \bar{\rho}_j)w_\mathrm{d}(r_{ij})\hat{\mathbf{r}}_{ij}, \tag{1.20}$$

where A and B are interaction parameters, $r = |\mathbf{r}_{ij}|$, $\hat{\mathbf{r}}_{ij} = \mathbf{r}_{ij}/r$. $w(r)$ and $w_\mathrm{d}(r)$ are the weight functions differing from one another only by the cutoff:

$$w(r) = \begin{cases} 1 - r, & r \leq 1, \\ 0, & r > 1, \end{cases} \tag{1.21}$$

$$w_\mathrm{d}(r) = \begin{cases} 1 - r/r_\mathrm{d}, & r \leq r_\mathrm{d} \\ 0, & r > r_\mathrm{d}. \end{cases} \tag{1.22}$$

While the force is pairwise, the energy is inherently many-body and cannot be decomposed into pair contributions. A visual comparison of the two force fields is shown on Fig. 1.4.

The local density $\bar{\rho}_i$ of particle i is defined such that it smoothly decreases from maximum value at zero separation down to zero at $r = r_\mathrm{d}$:

$$\bar{\rho}_i = \sum_{j \neq i} \frac{15}{2\pi r_\mathrm{d}^3} w_\mathrm{d}(r_{ij})^2 \quad \text{for} \quad r_{ij} \leq r_\mathrm{d}, \tag{1.23}$$

where we stress that index j runs over *all* the particles, not just those of the same species as ith particle. Also, the local density is normalised, such that $\int_0^\infty \rho(r) 4\pi r^2 \, dr = 1$. In the simulation, the system is thermostatted as in standard DPD via the dissipative and random force.

Warren showed that for $A < 0$ and $B > 0$ this force field leads to the liquid-vapour coexistence, and derived the EOS [37]:

$$p = \rho k_\mathrm{B} T + \alpha A \rho^2 + 2\alpha B r_\mathrm{d}^4 (\rho^3 - c\rho^2 + d), \tag{1.24}$$

with fitting constants $\alpha = 0.1, c = 4.16$, and $d = 18$. This EOS was revisited by Jamali [38], who came with a slightly different and arguably more precise form:

$$p = \rho k_\mathrm{B} T + \alpha A \rho^2 + 2\alpha B r_\mathrm{d}^4 (\rho^3 - c'\rho^2 + d'\rho) - \frac{\alpha B r_\mathrm{d}^4}{|A|^{1/2}} \rho^2, \tag{1.25}$$

where $c' = 4.69$ and $d' = 7.55$. In practice, the difference between these two EOS's is small for typical liquid densities, e.g. at $A = -40, B = 25, \rho = 6$ it is about 5%.

In standard DPD, the simulation density is decided a priori, most often as the lowest possible number at which the EOS is still quadratic, $\rho = 3$. This value then remains fixed throughout the simulation by the constraint of constant volume. However, the density in an MDPD liquid can arise naturally by choosing the parameters A, B and r_d at which the liquid forms a droplet with a surface. In this sense, it is more resemblant of a classical molecular dynamics force field. In fact, the equilibrium density of an MDPD liquid can be fully determined A and B and the many-body cutoff r_d.

In varying A, B, r_d there are several obvious constraints. Firstly, we choose $0 < r_\mathrm{d} < 1$, $A < 0$, $B > 0$ to make the interaction attractive near $r = 1$ and repulsive at the core near $r = 0$. In fact, to ensure that $F(0) > 0$, it follows from eq. (1.20) that $B > -A 2\pi r_\mathrm{d}^3/15$. Even values close to this boundary might lead to poor temperature conservation. Henceforth we will call this a *no-go* region.

Many-body DPD has so far been applied only to very simple systems in order to probe vapour-liquid coexistence, such as pure water [39, 40, 41] or a mixture of salt and water [42]. Polymer behaviour briefly was explored, including the computations of end-to-end distance and radius of gyration and surface tension and investigation of the coil-globule transition [43], and surface angles and interactions [10]. In all the cases, the interaction parameters (A, B, r_d) were guessed rather than rigorously matched to real liquids. Furthermore, the scaling with CG degree derived by Füchslin *et al.* [30] was not enforced in the following publications [42, 40, 41]. Resolving these problems is the topic of Chapter 6.

Having described the simulation methods, we now turn to the discussion some practical aspects of atomistic computer simulations, which might be valuable for students beginning in the field.

1.5 Technical aspects of a simulation

To gain a feel for atomistic or CG simulations, it is vital to understand the practicalities before the start. Here, we will restrict the discussion to atomistic simulations using force fields.

Nowadays, one does not need to write one's own MD simulation package, as several large-scale and heavily optimised codes are available for free, including LAMMPS,[23] Gromacs,[24] NAMD[25] or DL_POLY[26]. Indeed, it would be extremely inefficient, even futile, to reproduce the thousands of man-hours that were invested into the development of these packages. Instead, a viable route for testing new ideas is to add or modify the code of already existing packages.

Inputs and outputs

An atomistic simulation cannot start without well-defined inputs. These are:

- particle positions, types, masses and charges (here, "type" means not only atomic type, but a type of atom in a specific chemical environment),
- bonds as connections between two or more particles,
- force field and its parameters between distinct particle and bond types,
- initial box size,
- thermodynamic ensemble, most often NVT or NpT,
- global simulation details, such as time step, number of steps, and integration method.

A simulation typically outputs one or more of the following:

- snapshots of particle positions (trajectories), velocities and forces,
- total pressure or the pressure tensor,

[23] http://lammps.sandia.gov
[24] http://www.gromacs.org
[25] http://www.ks.uiuc.edu/Research/namd/
[26] https://www.ccp5.ac.uk/DL_POLY_C

- energies (kinetic, van der Waals, bond, electrostatic).

From these outputs a range of experimental observables can be computed, either automatically within the software package or at the end by manual post-processing.

i. density and density profiles for a given atom type,

ii. mean-square displacement, which yields self-diffusivity, assuming steady-state Einstein behaviour:

$$D = \lim_{t\to\infty} \frac{\langle(\mathbf{r}(t) - \mathbf{r}(0))^2\rangle}{3\,d\,t}, \tag{1.26}$$

where d is the number of dimensions,

iii. surface tension, which can be computed from pressure tensor components (assuming the interface is across x-coordinate):

$$\sigma = \frac{L}{2}\left(\langle p_{xx}\rangle - \frac{\langle p_{yy}\rangle + \langle p_{zz}\rangle}{2}\right), \tag{1.27}$$

iv. radial distribution function (RDF), which is a normalised histogram of distances of pairs of atoms, and structure factor, an observable of X-ray diffraction experiments that can be computed from RDF as follows for a 3D system:

$$S(k) = 1 + \rho\int_0^\infty [(g(r) - 1]\frac{\sin kr}{kr} 4\pi r^2 dr. \tag{1.28}$$

v. autocorrelation functions yielding self-diffusivity, vibrational spectrum or electric conductivity, if charges are present. For example, self-diffusivity can be computed from the velocity autocorrelation function (VACF):

$$c_{vv}(t) = \langle \mathbf{v}(0)\cdot\mathbf{v}(t)\rangle, \qquad D = \frac{1}{3}\int_0^\infty c_{vv}(t)dt, \tag{1.29}$$

vi. chemical potential in excess to the ideal $\mu^{\mathrm{id}} = -k_{\mathrm{B}}T\ln(\rho\lambda^3)$, where ρ is number density and λ de Broglie wavelength, which can be computed via Widom particle insertion [3]:

$$\mu^{\mathrm{ex}} = -k_{\mathrm{B}}T\ln\langle e^{-\Delta U_{N,N+1}/k_{\mathrm{B}}T}\rangle. \tag{1.30}$$

Tools for pre- and post-processing

Before the simulation, one must (nearly) always create the input files containing the coordinates of the atoms. Here, I provide a short overview of generating an input file for LAMMPS (other packages have workflows that are conceptually similar but different in details). Unfortunately, each package has a different format for the input file, and I have not found so far any tool for a simple conversion between these. The only common link is the use of ancient formats pdb and psf.

For simpler systems, one can generate the input file manually using Python by randomly generating particle positions in a box and appropriately formatting it for a given package. For

more complex systems, `Packmol`[27] automatically packs a number of molecules into a pre-defined volume such that they do not overlap too much. Consequently, `charmm2lammps` assigns the force field parameters with the types in the coordinate files (in pdb and psf format) and creates a LAMMPS-compatible data file containing initial coordinates and bonds. Should one want to create a lattice, this can be achieved very simply within the LAMMPS input file.

The emergence of high-throughput simulations for materials screening have brought about the need for simulation workflows to systematically keep track of what has been done and what is to be done. Two such tools are now available: `AIIDA`[28] and `Caf`[29].

To post-process the output for the sake of computing experimental observables such as RDF or self-diffusion constant, one can exploit excellent scientific computing infrastructure created around Python in the form of Numpy, Scipy, Matplotlib, Pandas and many other packages. Finally, let me mention the obvious. A most suitable environment for atomistic simulations or any scientific computing in general is Linux together with the command line (Bash) and tools like Sed and Awk. The command line in Linux is an indispensable tool for any sophisticated scientific work, and many scientific packages are built for easy installation in Linux.

Miscellaneous points

Having clarified the technical aspects, here I summarise a few technical points to mention should anyone want to write an MD package on their own to test ideas.[30] Even if one would not, these things do not come naturally and should be mentioned, as they are not obvious at the beginning of a project. These points are purely subjective, and there is no order of importance. A Python code snippet is provided where appropriate.

1. Potential (e.g. LJ) should be finite-ranged for the sake of efficiency, i.e. should have some cutoff. The energy and force should be made continuous at the cutoff. Choosing the cutoff r_c, beyond which the potential is set to zero, the continuity in energy can be enforced by the following shift:

$$V_{\mathrm{e-shift}}(r) = \begin{cases} V_{\mathrm{LJ}}(r) - V_{\mathrm{LJ}}(r_c), & r \leq r_c, \\ 0, & r > r_c. \end{cases} \tag{1.31}$$

   To enforce continuity in force at $r = r_c$, we need to shift derivatives as well:

$$V_{\mathrm{f-shift}}(r) = V_{\mathrm{LJ}}(r) - V_{\mathrm{LJ}}(r_c) - V'_{\mathrm{LJ}}(r_c)(r - r_c). \tag{1.32}$$

2. Periodic boundary conditions (PBC) should be enforced to account for the continuum and eliminate potentially unphysical effects of the walls. This involves the search for the nearest neighbours at each timestep [44].

```
"""
box: (3, 3) matrix, simulation box
```

[27] http://m3g.iqm.unicamp.br/packmol/home.shtml
[28] aiida.net
[29] github.com/azag0/caf
[30] ... and which I had to learn the hard way.

```
    inv_box: (3, 3) matrix, inverse simulation box
    rij: (3, 1) vector of distance of two atoms
    """
    def pbc(rij, box, inv_box):
        inv_box = np.linalg.pinv(box)
        g = inv_box @ rij
        g = g - np.round(g)
        r_new = box @ g
        return r_new
```

3. Initial velocities should be sampled from normal distribution with zero mean and variance equal to $k_{\mathrm{B}}T/m$, where $k_{\mathrm{B}}T$ is thermal energy and m particle mass. Also, total momentum should be set to zero:

```
    """
    N: number of particles
    """
    V = np.random.randn(N, 3) * np.sqrt(kB * T / m)
    V -= np.sum(V, 0) / N
```

4. To account for electrostatic forces from the charges, Ewald summation is used [3].

5. For integration, use Verlet scheme, as RK4 is not simplectic and too inefficient:

```
    for i in range(1, Nsteps-1):
        a = force(r[i]) / m      # compute acceleration
        r[i+1] = 2 * r[i] - r[i-1] + a * dt**2
```

6. Pressure in a simulation box with PBC is calculated via the virial theorem [3]:

$$p = \rho k_{\mathrm{B}}T + \left\langle \frac{1}{3V} \sum_{i<j} \mathbf{F}_{ij} \cdot \mathbf{r}_{ij} \right\rangle. \tag{1.33}$$

7. Prior to an MD simulation, the energy of the box should be minimised to eliminate any divergences due to particle overlap. Minimisation is essentially the same as a run at a very low temperature.

8. Bonds and angles in molecules are often fixed by SHAKE or RATTLE algorithms [3] in order to eliminate fast degrees of freedom and so enables a greater time step. A common example are the hydrogens in a water molecule.

Having addressed the theory and practice of computer simulations, let us now discuss how these can be used in gaining insight into the behaviour of hydrogen fuel cells.

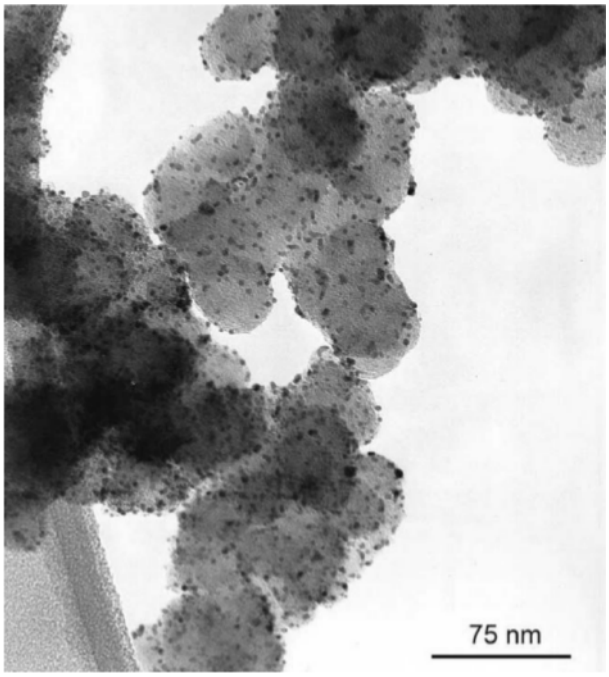

Figure 1.5: TEM image of the catalyst layer of a hydrogen fuel cell. The large round grey structures are the carbon support, and the small black dots are Pt nanoparticles. Around these is the layer of thin Nafion film (not visible on this figure). Source: [55].

1.6 Modelling membrane electrode assemblies

1.6.1 Membrane

At the heart of each FC is a perfluorosulfonic acid (PFSA) membrane, which serves as an electrode separator. Nafion, the most prominent representative, was invented by DuPont in late 1960s, followed by derivations synthesised by other companies.

There have been ongoing debates about the structure and morphology of Nafion and other perfuorosulfonic acid (PFSA) membranes summarised in a number of review articles focusing on structure [45], transport properties [46, 47, 48], and overall behaviour [49].

In trying to understand the nanoscopic structure of the water-rich ionic domains in PFSA membranes, many different models have been proposed. The first was the cluster-network model of Hsu and Gierke [50]. Whilst unable to describe quantitatively the X-ray scattering from Nafion, this model captures the essential qualitative feature of nanophase separation between ionic and fluorocarbon phases with a characteristic length scale of 3 to 5 nm. Gebel *et al.* [51] claimed that a fibrillar model, in which extended fluorocarbon chains decorated by ionic side groups and water, gave a better match to small-angle X-ray (SAXS) data. In 2008, Schmidt-Rohr proposed a parallel cylinder model [52], claiming that the SAXS scattering curve best supports a system where the backbone forms cylinders a few Angstroms wide and a few hundred nanometres long. Subsequently, Kreuer refuted Schmidt-Rohr's model and argued for flat and narrow water domains [53]. The discussion about the morphology is still far from resolved, but recent mesoscale modelling results tend to favour structures which more resemble ion-clustered models for bulk ionomer [54].

Most of the studies carried out so far have focused on bulk Nafion. However, studies of its role within catalyst layers in real membrane-electrode assemblies are limited. The hydrogen oxidation and oxygen reduction reactions take place within the anode and cathode catalyst layers respectively, which are complex structures comprising catalyst nanoparticles, thin films

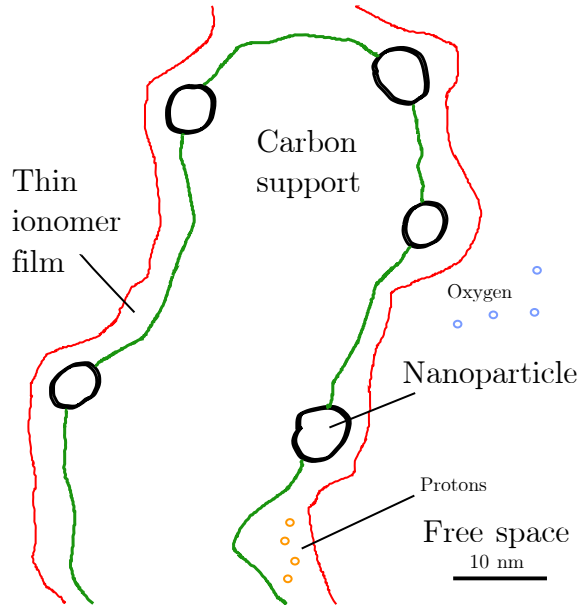

Figure 1.6: A more detailed schematic view of Fig. 1.5 showing the structures in the catalyst layer on the scale of 1 to 10 nm.

of ionomer, and free space, through which reactant gases flow in and product water, unreacted gases, and water vapour flow out.

It has been found that Nafion confined into a thin film has a structure vastly different from the bulk. The effect of confinement on structure has been experimentally studied by the NIST group using X-ray and neutron reflectometry. Dura *et al.* observed lamellae in a hydrated Nafion thin film deposited on SiO_2 surface, but not on Pt or Au surfaces [56]. Similarly, DeCaluwe *et al.* discovered oscillations in composition between layers rich in water and those rich in fluorocarbon groups, effectively producing a lamellar structure close to the Nafion-substrate interface [57]. Eastman showed that a significant change in properties occurs at film thicknesses below 60 nm [58]. In a different study [59], a Nafion thin film deposited on a silica substrate and explored using neutron reflectivity revealed an anisotropy in that water was ordered in layers parallel to the substrate. Modestino *et al.* observed thickness-dependent proton conductivity in a Nafion thin film [60]. All these studies suggest that the ionomer films within catalyst layers have very different structure and properties to bulk membranes. Interpretations based on the assumption that catalyst layer ionomer behaves like very thin membrane material are likely to be misleading.

Many simulations have been done on bulk membranes using various theoretical frameworks [61]. Among these, dissipative particle dynamics played a prominent role due to its fast equilibration and ability to cover a system size of several tens of nanometres, a length scale necessary to observe the effects of water clustering. The most prominent studies have been carried out by Yamamoto & Hyodo [17], Wu *et al.* [14, 15, 16], and Dorenbos *et al.* [21, 22, 24, 19, 25, 18, 23, 62]. All the workers were been able to reproduce structures qualitatively resembling the cluster-network model, with water cluster size of several nanometres, demonstrating that mesoscale methods offer a reliable insight into complicated polymer-solvent systems.

In comparison to bulk ionomers, there have been far fewer attempts to model a thin film version. Kendrick *et al.* compared IR spectroscopy of a Nafion thin film deposited on a Pt {111} surface with DFT calculations [63]. Nouri-Khorasani used classical molecular dynamics

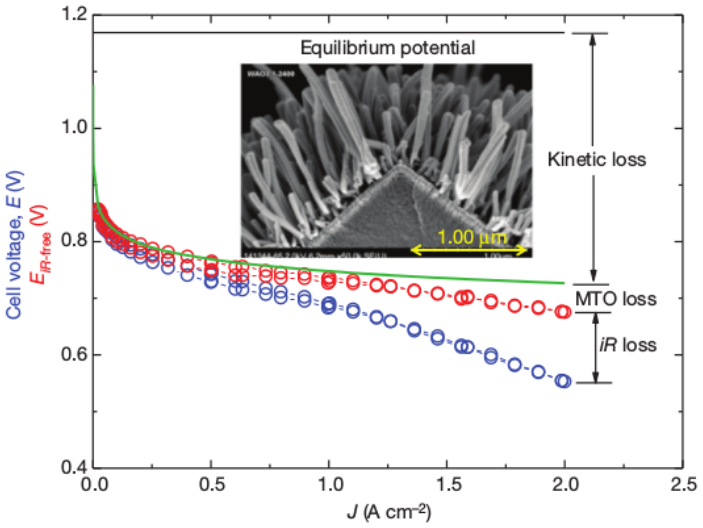

Figure 1.7: The polarisation curve showing the largest voltage losses. The kinetic loss is due to the slow oxygen reduction reaction. Source: [68].

to calculate hydronium ion distribution and self-diffusion of water in a nanochannel [64] as well as in a film on a PtO substrate [65]. Borges used the same method to gain insight into the hydrophobicity of Nafion surface [66, 67]. On the mesoscale level, Dorenbos *et al.* simulated Nafion confined by carbon surfaces at various hydrophobicities, which were controlled by the solubility parameter [20], revealing anisotropy in water diffusion, with a greater tendency for water to move parallel to the film. The authors claimed that the increased hydrophobicity of the carbon increased this anisotropy.

1.6.2 Nanoparticles and catalysis

Heterogeneous catalysis, where the phase of the catalyst is different from the phase of the catalysed compound, is one of the central topics of trillion-dollar industries producing oil and gas, fertilisers or food. Generally, it is performed under extreme temperatures (700-1000 °C) and pressures (around 20 bar).

Central to fuel cell research is the ORR, in which hydrogen protons from the membrane join the electrons from the outer circuit and together react with oxygen from air to form water. For practical purposes, the ORR in FCEVs happens at nearly ambient conditions (atmospheric pressure and temperature of 80 °C), which are far less suitable than those in, e.g., oil refineries, and hence is the main rate-limiting step in the overall FC performance.

Even though it is difficult to break this process down into constituents and figure out their individual contributions towards the overall performance, the consensus is that ORR taking place at the cathode side of the catalyst layer is responsible for the most significant operational voltage drop of a single MEA from the theoretical value of 1.23 V (Fig. 1.7) [69]. Breaking down this process, there are several candidate suspects: the chemical constitution or the size of the catalytic nanoparticles (NP) as well as the NP support, the coverage of the NP by a pool of water preventing the access of oxygen to the NP surface, or some complex interplay of the ionomer covering the NP with a pool of water right at the interface.

Catalysis takes place on the surface of the NPs. Hence, the basic aim of catalyst design is to make the NPs as small as possible, in order to maximise the surface to volume ratio as well as minimise the amount of inactive but expensive atoms at the core of the NP. However,

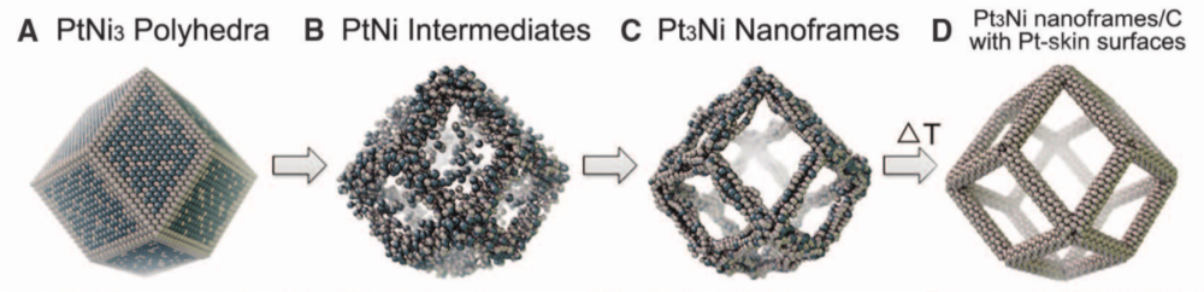

Figure 1.8: Experimental evolution of NP nanoframe synthesis. Source: [76].

if the NP size is too small, the NPs tend to wander around the support and merge together (a phenomenon known as sintering), thus reverting the effort.

Several routes have been explored to address this challenge [68, 70]. One possibility to save expensive Pt is to create alloyed NPs, where the core is composed of a cheaper metal and only the shell would predominantly contain active PGM [71, 72, 73, 74, 75]. A heavily explored example is an alloy Pt_3M, where M is Ni, Co, Fe, Ti or V [72]. Another way is to create NP frames, thus maximising the surface area [76] (see Fig. 1.8). Finally, one can also a search for a fundamentally new metal as a catalyst to supersede Pt. Lefèvre *et al.* synthesised an porous iron-based catalyst on carbon support approaching the performace of Pt NPs [77].

Despite the dramatic progress in catalyst design in the past few decades, there is plenty of scope for improvement. Materials simulations are either imperfect, if classical force fields, such as the embedded-atom model, are used, or expensive, if quantum-resolved simulations, such as the DFT, are employed. This obstacle could be overcome by new force fields with parameters machine-learned from DFT but with simulation complexity in the same order as classical molecular dynamics [78, 79, 80, 81, 82]. A systematic computational screening of a range of possible combinations might uncover unexpected catalytic alloys.

1.7 The scope of this thesis

This thesis attempts to tackle a small subproblem in the grand scheme of enabling the fuel cell technology to enter the transport industry. We devise and employ mesoscale simulation methods to gain insight into the behaviour of the thin ionomer films covering the carbon support and platinum nanoparticles in the catalyst layer. We first apply standard DPD to a thin Nafion film confined from both sides by carbon and quartz support (Chapter 2). Consequently, we devise a parametrisation method for many-body DPD to be able to simulate the free-space setting of a thin Nafion film on a carbon support, which can be directly compared with experiment and expected to capture the real behaviour of the catalyst layer. Finally, we outline possible avenues in future research based on the ideas presented in this thesis and the accompanying papers.

Chapter 2

Mesoscale simulations of confined Nafion

A weighty argument for the intellectual
is the most ordinary slap in the face.

Varlam Shalamov

Here we present simulations of thin Nafion films, investigating the effects of confinement on the water diffusivity and clustering. Exploring a large parameter space of water uptakes, film thicknesses and two confining materials, we discover that the clustering of water is strongly driven by the film thickness as well as the hydrophobicity of the confining material, and that the anisotropy in diffusivity increases with the decreasing film thickness. These findings have important consequences for the movement of water in the catalyst layer of the fuel cells, where thin Nafion films cover the carbon support with the catalytic nanoparticles.

We explore a Nafion thin film via simulation with the aim to mimic the structure formed within the catalyst layer at correct length scales. We investigate the changes in water morphology and transport properties for a wide range of operational water contents, from a very dry state to the membrane effectively immersed in water, and for a range of film thicknesses. For the confining substrates, we chose carbon and quartz as two opposite extremes in terms of hydrophobicity. Carbon is well-established as a fuel cell electrode material; quartz is often used as a substrate in neutron reflectometry studies [57, 56, 59].

In this chapter, we first briefly review the parameterisation procedure for ionomer thin film simulations, before presenting results on water distribution, diffusivity and connectivity. We then relate these results to the effects of confinement as a thin film on ionomer structure.

2.1 Simulation Method

2.1.1 Parametrisation

The general presentation of the DPD force field is provided Section 1.3; here, we summarise only vital points.

The default interaction parameter a for all particle (bead) types is set to 25. This number is derived from water compressibility, since water is treated as the default material in the simulation. For simplicity, this value is kept the same for beads representing bits of PTFE backbone and side chains. The chosen number density is the smallest possible for the sake of simulation efficiency, $\rho = 3$, and the friction parameter is chosen in line with most of the literature, $\gamma = 4.5$. The choice of these three parameters, a, ρ and γ, concludes the unique definition of a pure DPD liquid.

The behaviour between chemically different constituents, such as water, PTFE backbone and side chains, is accounted for by the cross interaction terms Δa_{ij} between unlike beads. These are derived from the χ-parameter, as the DPD equation of state can be matched to the Flory-Huggins theory [7]. The relationship between Δa and χ-parameter is linear: $\Delta a = 3.27\chi$ at density $\rho = 3$.

Several methods are available to calculate the χ-parameters. Common choices are a simple relation based on molar volume V_m and Hildebrand solubility parameters δ_i of component i:

$$\chi_{ij} = \frac{V_\mathrm{m}}{RT}(\delta_i - \delta_j)^2, \tag{2.1}$$

or more sophisticated Monte Carlo sampling developed by Fan *et al.* [34]. We chose the mixture of these approaches: taking the more precise χ parameters derived by Wu *et al.* via the Monte Carlo sampling, where available, and the more approximate eq (2.1) in case of the interactions containing the substrate beads.

2.1.2 System under investigation

We set the DPD length scale r_c as follows: starting from the approximate volume of one water molecule $V_0 = 30$ Å^3, number of water molecules per bead $N_\mathrm{m} = 6$ and DPD density $\rho = 3$, the bead diameter for our simulation is $r_\mathrm{c} = (V_0 N_\mathrm{m}\rho)^{1/3} = 8.14$ Å. The box size is $40 \times 40 \times 40$ (in DPD units), corresponding to 32.5 nm in SI units and accommodating in total 192,000 beads.

The time scale $\tau = \sqrt{m_\mathrm{c} r_\mathrm{c}^2 / k_\mathrm{B} T_\mathrm{c}}$ is 5.35 ps. The simulation step was set to $\Delta t = 0.04\,\tau$. One simulation ran for 40,000 steps (8.6 ns), from which the first 30,000 served as equilibration. A few nanoseconds of equilibration are sufficient for a DPD simulation due to the softness of the interparticle potential.

The coarse-graining degree is six water molecules per bead. Common DPD parametrizations involve three [83] or four [17] water molecules per bead. Following Wu *et al.* [14] we coarse-grained further in order to simulate larger boxes at the same computational overhead. In contrast with the workers [18, 17], we also put three water molecules in the C bead containing mainly the backbone and the sulfonic acid group to represent the strong binding between the acidic group and water. Some water is thus bound to polymer chains and its movement is more

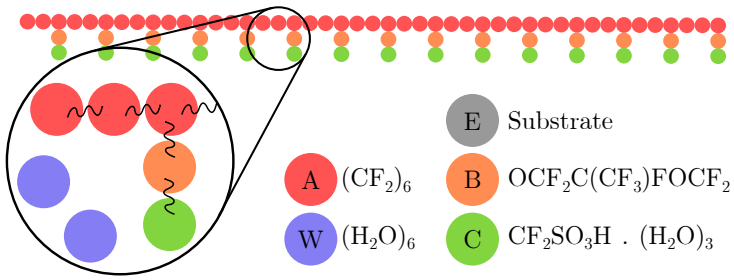

Figure 2.1: DPD beads used in the simulation. Each polymer chain has 15 segments, each segment has five beads. Water beads (blue) are freely floating around.

	δ (MPa$^{1/2}$)	χ (no units)			
		A	B	C	W
A	12.7	0			
B	13.6	1.23	0		
C	23.0	7.44	2.70	0	
W	47.8	3.36	1.53	1.48	0
E (Carbon)	25.0	1.10	0.94	0.03	3.77
E (Quartz)	35.0	3.60	3.32	1.04	1.19

Table 2.1: Flory-Huggins χ-parameters defined between pairs of beads used in the simulation. Excess repulsions $\Delta a_{ij} = 3.27\chi_{ij}$ were added to the default value $a = 25$.

restricted. The water content λ is defined as the number of water molecules per sulfonic acid group $N_{H_2O}/N_{SO_3H^+}$ with respect to the whole simulation box.

The polymerisation of the PTFE chain is 15 (Fig. 2.1) and each segment has five beads. Overall our polymer-solvent system contains five bead types: A, B, C, W, and E. To get the χ-parameters For A, B, C, and W beads, we used the data from Wu *et al.* [14], who employed the method by Fan *et al.* [34]. Otherwise, we used eq. (2.1). The solubilities of A, B, and C beads were taken from Dorenbos [20] and those for water, graphite and quartz were derived from the cohesive energy density (Table 3.2). The molar volume of water in molecular form was considered for all beads $V_m = 18$ cm^3 mol^{-1}, since all DPD beads are expected to have similar size and mass. The full cross-interaction parameter is:

$$a_{ij} = 25 + 3.27\chi_{ij}. \tag{2.2}$$

To understand and quantify the behaviour of confined Nafion we measured multiple characteristics: distribution of water in the direction parallel to the film, clustering of water in the film using percolation theory, and self-diffusion coefficient of the W beads.

The simulations were run in the DL_MESO package [84]. Box initialisation as well as post-processing of water distribution, diffusivity, and clustering were done using home-made Python scripts. Two confining materials with four film thicknesses and the bulk, plus eleven water contents, amounts to 99 different configurations in total. Each configuration was averaged over 3 to 6 independent trials differing by the random seed used for the box initialisation. The confining substrate beads were frozen for convenience during the simulation, since the substrate is solid and thus not expected to move on the same time scale as the thin film.

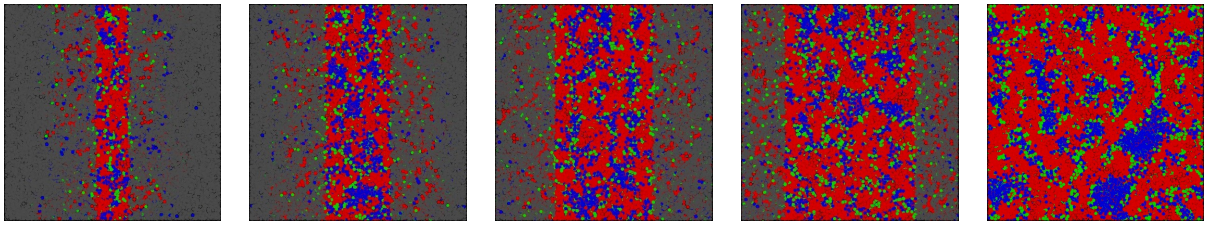

Figure 2.2: Equilibrated boxes of Nafion thin film confined by carbon for thicknesses $d = 5, 10, 15, 20$ nm, respectively and the bulk, at water content $\lambda = 16$. Red: backbone (A and B beads). Green: sulfonic acid groups (C). Blue: water (W). Grey: electrode (E).

2.1.3 Dynamics

We calculated the diffusivity via the mean square displacement (MSD) defined as

$$D_d = \frac{\langle |\mathbf{r}(t_\mathrm{f}) - \mathbf{r}(t_\mathrm{i})|^2 \rangle}{2\,d\,(t_\mathrm{f} - t_\mathrm{i})}, \tag{2.3}$$

where $d \in \{1, 2, 3\}$ is the dimensionality of the system. It is known that polymer systems possess different regimes of diffusion at various time scales. We chose the initial and final times t_i and t_f respectively to so as to capture the linear regime, which we identified by plotting the MSD on a logarithmic scale. For carbon confinement, this regime takes place between 0.2 and 2τ and for quartz between 2 and 19τ.

As a check we also recalculated the diffusivity via the velocity autocorrelation function, a different method using bead velocities instead positions: $D_\mathrm{3d} = 1/3 \int_0^\infty \langle \mathbf{v}(0) \cdot \mathbf{v}(t) \rangle dt$. These two approaches yield the same results up to fluctuations, so one can remain confident in exploiting the MSD route.

DPD is known to overstate the dynamical properties due to its very soft force field. Tto put the water diffusion in a polymeric system into a meaningful perspective we compared all our calculations to the diffusivity $D_0 = 0.3$ of a pure liquid at standard simulation parameters mimicking pure water: $a = 25$, $\rho = 3$, and $\gamma = 4.5$.

2.2 Results

2.2.1 Water distribution

Our first step is to understand how water distribution in Nafion changes under the influence of confinement. Visual observation of the equilibrated boxes shows that clustering is established for carbon as well as quartz substrate (Fig. 2.2) for all water contents. For quartz, water is more dispersed in the backbone phase. A certain fraction of water has leaked into the confining material, which is expected due to the soft interparticle potential.

Despite the clustering created under the confinement of carbon, the size and structure of water clusters varies with the amount of water or film thickness. This is revealed by plotting the water distribution in the direction perpendicular to the Nafion film for carbon (Figs. 2.3) and quartz (Figs. 2.4). Here we observe different numbers of peaks in the water profile for each pair of (d, λ). For low film thickness 5 nm, increasing water content creates a massive peak in

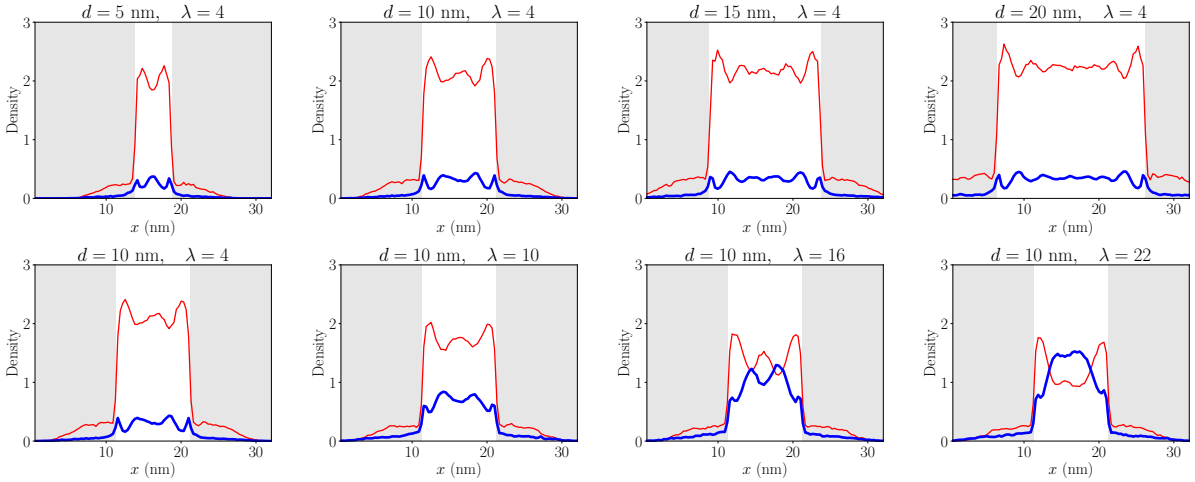

Figure 2.3: Top row: Profiles of water (blue) and PTFE backbone (red) confined by carbon for a range of film thicknesses $d = 5, 10, 15, 20$ nm at water content $\lambda = 4$. Bottom row: Profiles of water (blue) and PTFE backbone (red) confined by carbon for a range of water contents $\lambda = 4, 10, 16, 22$ at film thickness $d = 10$ nm.

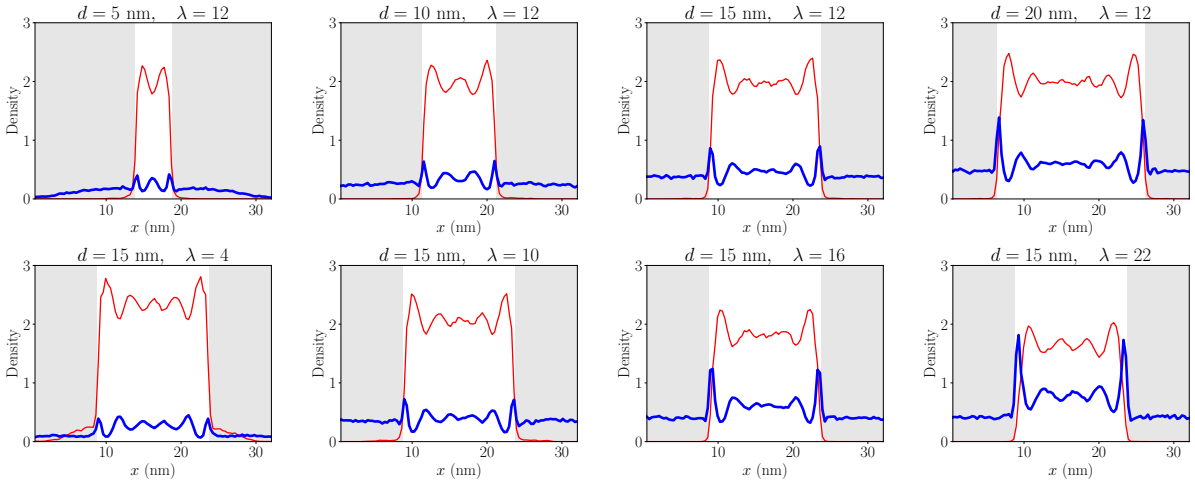

Figure 2.4: Top row: Profiles of water (blue) and PTFE backbone (red) confined by quartz for a range of film thicknesses $d = 5, 10, 15, 20$ nm at water content $\lambda = 16$. Bottom row: Profiles of water (blue) and PTFE backbone (red) confined by quartz for a range of water contents $\lambda = 4, 10, 16, 22$ at film thickness $d = 15$ nm.

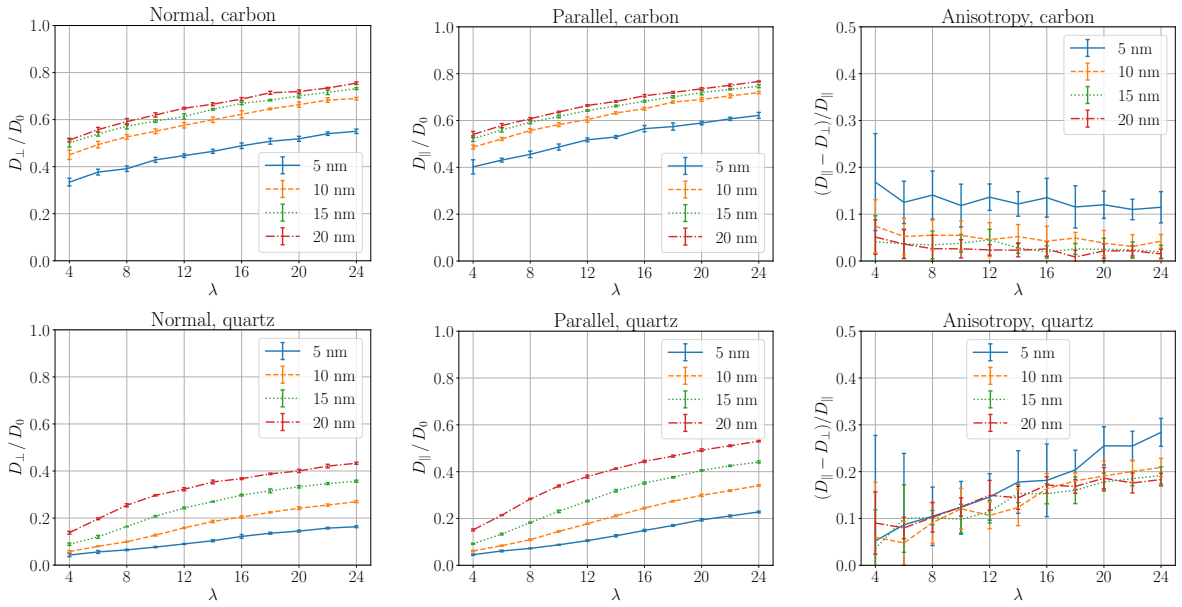

Figure 2.5: Parallel $D_{\parallel}$ and normal $D_{\perp}$ diffusivities of water for Nafion film confined by carbon (top row) and quartz (bottom row) as a fraction of the self-diffusion coefficient D_0 of a pure DPD liquid at $a = 25$. Right column: Percentage difference between parallel and normal diffusivity.

the middle of the film. For larger thicknesses, notably 20 nm, the profile passes from as many as five peaks at $\lambda = 4$ to one large peak at $\lambda = 24$. We can deduce that at low λ's water is clustered into peaks of typical size 4-5 nm, whereas for high λ's most water concentrates in the middle of the film. All the profiles are shown in the supplementary material of Ref. [85].

In contrast to carbon, hydrophilic quartz produces large peaks of water at the ionomer-substrate interface. Water peaks inside the ionomer are relatively smaller and keep their size with increasing amount of water, but their number changes with both film thickness and water content. For 20 nm, this number goes from five at $\lambda = 4$ to three at $\lambda = 24$.

Above $\lambda = 16$, a distinct water depletion zone is formed at the ionomer-carbon interface, and a water saturation zone appears at the ionomer-quartz interface for all film thicknesses and water contents. Both these effects are an unambiguous sign of the hydrophobicity and hydrophilicity of carbon and quartz, respectively.

2.2.2 Diffusivity

Having analysed the static properties of water in confined Nafion films we proceed with the dynamics. It would be too much to expect exact quantitative agreement from DPD, but the overall trends in behaviour, such as increasing diffusivity with water content, are well captured, as can be confirmed by NMR measurements [46] shown on Fig. 2.6.

To understand the dynamics of our system we calculated the self-diffusion coefficient of W beads as a function of film thickness and water content. Figs 2.5 (top) show curves of water self-diffusion w.r.t. λ for multiple film thicknesses between carbon substrates. The gaps between these curves become narrower as the film thickness increases: the widest gap is between curves at 5 and 10 nm and the narrowest between 15 and 20 nm. More importantly, the asymmetry between normal and parallel diffusivities is most pronounced at 5 nm film, and

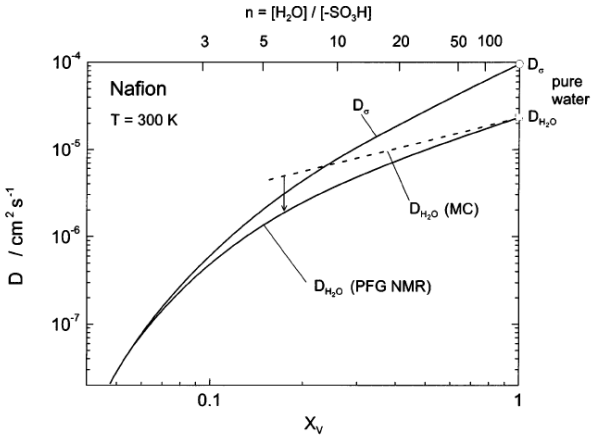

Figure 2.6: NMR measurements of the self-diffusivity of water in Nafion at a range of water contents λ (denoted in the figure as $n = [H_2O]/[-SO_3H]$). Taken from [46].

gradually decreases as the thickness increases. The diffusivity of water between quartz substrates (Figs. 2.5, bottom) shows different features: the curves of same film thickness are separated by the same distance at larger water contents, and the gap between parallel and perpendicular diffusivity narrows.

We define the measure $\eta = (D_{\parallel} - D_{\perp})/D_{\parallel}$ to quantify the anisotropy between parallel and normal diffusivities. Figs. 2.5 show strong dependence of η on film thickness in case of carbon confinement. This effect is much smaller in case of quartz and is only present at high water contents $\lambda > 20$. For carbon, there is weak depependence of η on the water content, whereas in case of quartz η rises linearly with λ. The error bars at $\lambda = 4$ and 6 suggest insufficient sampling due to low number of water beads in the simulation box, but they do not prevent from deducing the overall trend.

We note that the diffusivity anisotropy of a film confined by quartz does not disappear with increasing film thickness, in sharp contrast with carbon. We attribute this phenomenon to the excess water at the film-quartz interfrace creating a layer in which the W beads can move relatively freely in parallel to the film. As the water profiles on Fig. 2.4 demonstrate, this layer becomes more pronounced with rising water content and irrespective of the film width, which also explains the steady increase of η.

These findings suggest explanations for behaviour in the catalyst layer of fuel cells. Water freshly formed from protons and oxygen on the surface of platinum nanoparticles has a number of transport routes: it can either remain within the ionomer phase and move directly into the membrane (water back-diffusion); it can pass through the ionomer film covering the Pt and emerge as liquid water within the pore space of the catalyst layer, or it can evaporate from the surface of the ionomer film into the pore space. The balance of these pathways will depend on the operating conditions of the cell (relative humidity, current density, pressure) and the position of the Pt within the catalyst layer in x, y and z directions. Clearly, the water content within, under and on top of the ionomer film will have a significant impact on the transport of oxygen to the Pt surface and it may not be necessary to suppose that the thin film of ionomer has inherently lower oxygen permeability as others have done [86, 87]; or it may be that both water build up and low ionomer permeability, caused by unusual structuring of the thin films, account for the local oxygen transport issue. In this context however, simulations of thin Nafion films on platinum surfaces would be highly desirable to clarify which of these explanations is

more likely.

2.2.3 Water connectivity

The diffusivity of water is one of the ways to describe general transport properties, but is insufficient if the particles move around by quantum tunnelling. This is exactly what the hydrogen protons in ionomer membranes do. Mesoscale methods cannot directly capture protonic conductivity, as they do not contain the concept of a proton or even a single atom. However, the percolation of water network in the membrane is a suitable proxy. Hsu *et al.* argued that percolation can explain the insulator-to-conductor transition in Nafion [88], and showed that the conductivity σ satisfies a simple power law: $\sigma = \sigma_0(\lambda - \lambda_c)^s$, where λ is the water content[1] and s the critical exponent.

According to the percolation theory, the same scaling applies to the percolation cluster strength [89, 90, 91]. Assuming the lattice in two or more dimensions and filling the sites with probability λ, a macroscopic *percolation cluster* spanning the whole lattice starts appearing for $\lambda > \lambda_c$ and its size, the percolation cluster strength P_∞, defined as the ratio of sites belonging to this cluster to the overall size of the lattice, grows as a power law:

$$P_\infty \sim (\lambda - \lambda_c)^s, \tag{2.4}$$

where s is between 0.3 and 0.4 regardless of the lattice type (cubic, hexagonal or other) [91].

We have used the ideas from percolation theory in order understand the trends in the protonic conductivity in confined Nafion. Our aim was the water clusters onto a cubic (in 3D) or square (in 2D) lattice and compute the percolation cluster strength P_∞. We then used the flood fill algorithm based on a stack[2] to count the cluster sizes.

We generated a water density map on a grid and set the cutoff for which a grid site still contains some water at 0.3, which is one tenth of the natural DPD density used in simulations. We then employed the flood fill algorithm to count the size of thus formed water clusters and observe how the largest one, the percolating cluster, varies with film thickness and water content. The code snipped is listed in the appendix.

We evaluated two site percolations: on a two-dimensional grid formed from density profile of a slice through the middle of the thin film, and on a three-dimensional grid spanning the whole simulation box. 2D percolation channels and clusters can be easily visualised and so offer more intuition about the effect of the confining material on the thin film; 3D percolation should be a suitable approximation for the channels through which the protons move, based on the assumption that the protons will follow the best-hydrated pathways. The nominal value of the percolation cluster strength scales with the box size and is therefore not a good measure to compare across various film thicknesses. Therefore, we rescaled this value by the ratio of film thickness and the box size.

Figs. 2.7 and 2.8 show 2D water clusters of a slice through a thin ionomer film confined by carbon and quartz, respectively. The 2D and 3D water percolation cluster strengths are shown in Fig. 3.8. In case of carbon confinement, the 2D percolation does not depend strongly on the

[1] Qualitatively, it does not matter if it is a water content or volume fraction of water.

[2] In my opinion, the best source I can provide is Wikipedia, but this of course cannot be officially referenced.

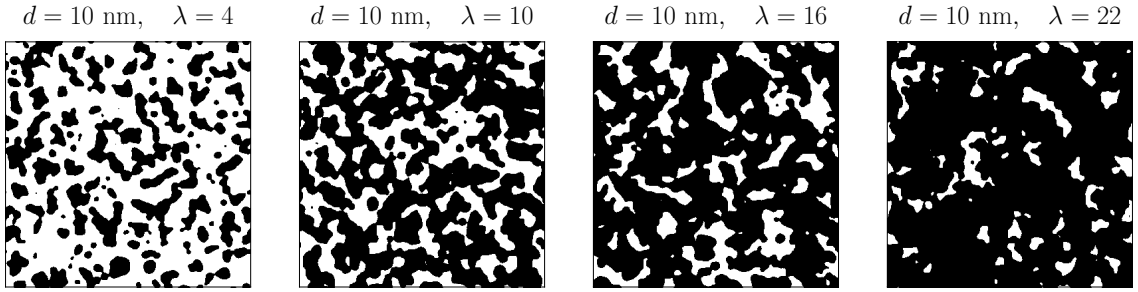

Figure 2.7: Water clusters in thin film confined by carbon for film thickness 10 nm and water contents $\lambda = 4, 10, 16, 22$ respectively.

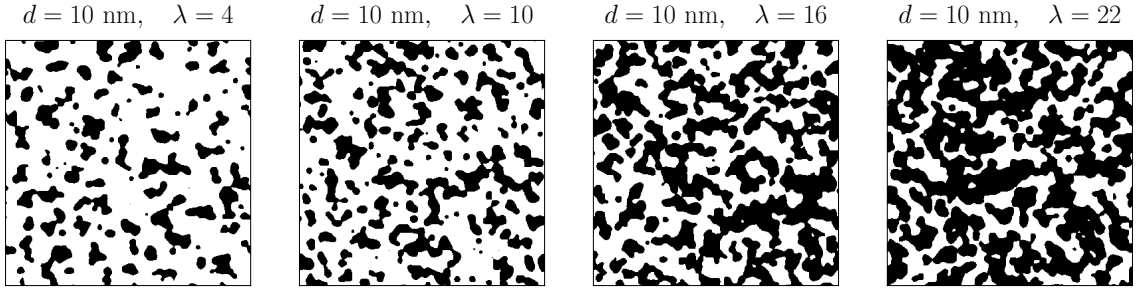

Figure 2.8: Water clusters in thin film confined by quartz for film thickness 10 nm and water contents $\lambda = 4, 10, 16, 22$ respectively.

film thickness, but 3D percolation is qualitatively similar to the diffusivity curves in Fig. 2.5, showing the same spacing of the equal film thickness curves. This suggests that the diffusivity of DPD beads computed in the previous section might be, after all, a good approximation for protonic conductivity. On the other hand, the 2D percolation of quartz demonstrates strong dependence on film thickness and, contrary to the intuition, the 5 nm film shows very high 2D percolation at low water uptakes. This can be confirmed by inspecting the clusters for e.g. $\lambda = 4$ in Fig. 7 in the supplementary material [85], which shows visibly better connectivity at 5 nm than 10 or 15 nm.

Following the insights by Hsu [88] and Kirkpatrick [91], our percolation analysis shows that in order to optimise for protonic conductivity or transport properties in general, hydrophobicity of the confining substrate is a key parameter. This conclusion was also reached by recent experiments [92].

2.3 Conclusion

We have simulated Nafion thin films confined by two materials, carbon and quartz, using dissipative particle dynamics. This well-established mesoscale method enabled the use of a large box size and rapid equilibration, compared with classical molecular dynamics. We used film thicknesses likely to be found in the catalyst layer of fuel cells, ranging between 5 and 20 nm.

Our simulations show that the clustering of water and the PTFE backbone in the direction normal to the thin film is driven by the confinement scale, water content and the hydrophobicity of the confining material. The number of clusters increases with film thickness, and the

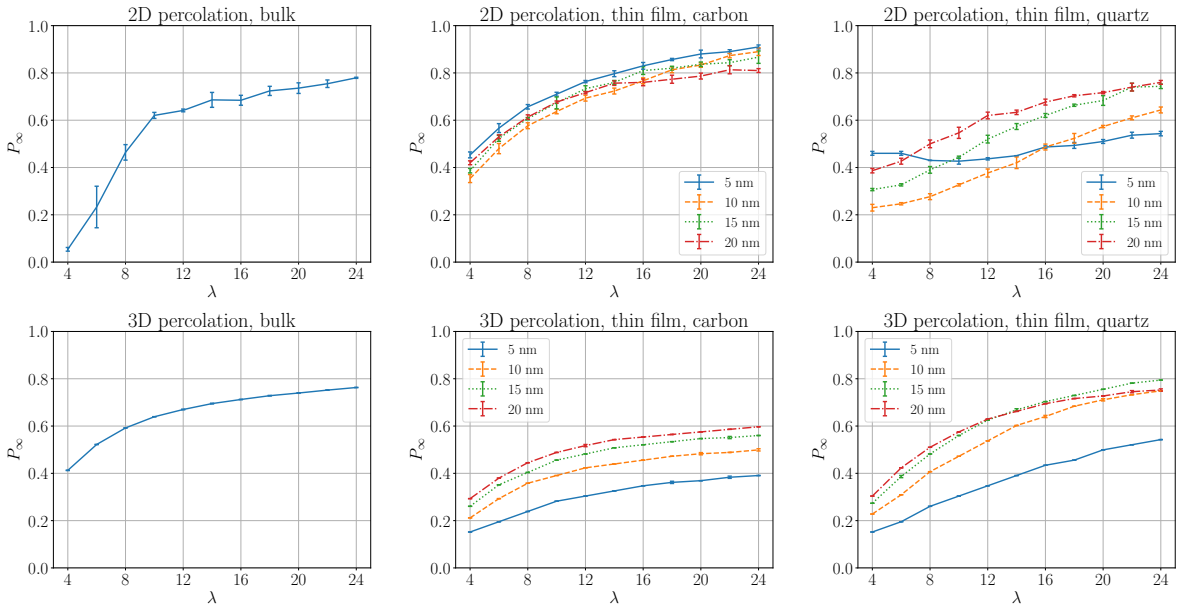

Figure 2.9: (Color online.) Percolation cluster strength P_∞ of water network in Nafion bulk and thin film confined by carbon and quartz, serving as a quantitative measure for water cluster connectivity.

cluster size depends on the water content but not the ionomer film thickness. For hydrophobic carbon, a depletion zone with little water is formed at the ionomer-carbon interface, whereas for hydrophilic quartz, water accumulates at the quartz-ionomer interface. These findings are in accord with the experiments performed by the NIST group [57, 56, 59].

Percolation analysis of water in the thin ionomer films reveals patterns in cluster size and connectivity that change with the confining material. Both carbon and quartz establish a well-connected network of channels. Water diffusivity shows significant anisotropy, regardless the of confining material. The liquid moves up to 20% more readily in the direction parallel to the thin film, compared to in the normal direction. This anisotropy increases with decreasing film thickness.

Our findings offer a perspective on the role of surface hydrophobicity of electrode materials deployed in the catalyst layer of fuel cells, and the direction of the flow of water formed on catalyst nanoparticles from protons and oxygen.

2.4 Appendix: The flood fill algorithm

Implementation of the flood fill algorithm in 3D for counting water clusters. Full working script is available here.[3]

```
def flood_fill(A, coord, old, new):
    """
    Counted fields in "old" are replaced by "new".
    Variables
    =========
    * A: input matrix
    * coord: (i, j, k)
    """
    N = len(A)
    i, j, k = coord
    if A[coord] == new: return  # security check
    if A[coord] != old: return

    A[coord] = new
    flood_fill(A, ((i+1) % N, j, k), old, new)
    flood_fill(A, ((i-1) % N, j, k), old, new)
    flood_fill(A, (i, (j+1) % N, k), old, new)
    flood_fill(A, (i, (j-1) % N, k), old, new)
    flood_fill(A, (i, j, (k+1) % N), old, new)
    flood_fill(A, (i, j, (k-1) % N), old, new)
    return
```

[3] https://github.com/petervanya/PhDcode/blob/master/PTFE_code/clustering_3d.py

Chapter 3

Nafion swelling and drying

> Talk is cheap. Show me the code.
>
> *Linus Torvalds*

Having described the properties of thin Nafion film confined from two sides by a carbon support exploiting standard DPD in the previous chapter, we now turn our attention back to the bulk Nafion. We simulate a typical experimental process of swelling Nafion by continually adding water until it reaches maximal size. We investigate the change in the morphology of both water clusters and PTFE backbone chains. We demonstrate that the hypothesis presented by Gebel [1] about rod-like shape of polymer chains at high water contents is not supported by our simulations.

There has been an ongoing debate about the structure and morphology of Nafion, and its dependence on water content. Several models have been proposed [50, 52] but none of them is conclusive. In 2000, Gebel has conducted experiment on Nafion at several water contents [1], ranging from 7.8% to 67%, which is a variation from a very dry stateup to the point at which the membrane is fully immersed in water.

Inspired by these experiments, we perform simulation to gain additional insight into the structure and morphology of these membranes. Firstly, we start with a very dry Nafion and, by adding water, gradually swell it. Secondly, we explore the reverse route, starting from dissolved Nafion and gradually removing water until there is almost none.

3.1 Simulation details

We consider Nafion as represented on Fig. 2.1, where the polymerisation is 15 monomers per chain, and each monomer contains five beads. Each A bead contains six CF_2 groups. We represent the water content λ as a ratio of the number of water molecules and the sulfonic acid groups: $\lambda = N(H_2O)/N(SO_3H^+)$. Table 3.1 shows a conversion from of λ to volume percentage used by Gebel. We explored water contents ranging from $\lambda = 3$ to 120.

As a simulation method, we used dissipative particle dynamics (DPD) at the coarse-graining degree of six water molecules per bead, which follows the parametrisation used by Wu *et al.* [14].

Table 3.1: Conversion of water content measured in number of water molecules per sulfonic acid group to volume percentage for a polymer with structure.

$N_{H_2O}/N_{SO_3H^+}$	Vol. frac.	$N_{H_2O}/N_{SO_3H^+}$	Vol. frac.
3	0.100	45	0.625
6	0.182	50	0.649
9	0.250	55	0.671
12	0.308	60	0.690
15	0.357	70	0.722
18	0.400	80	0.748
25	0.481	90	0.769
30	0.526	100	0.787
35	0.565	110	0.803
40	0.597	120	0.816

Table 3.2: Flory-Huggins χ-parameters defined between pairs of beads used in the simulation. Excess repulsions $\Delta a_{ij} = 3.27\chi_{ij}$ were added to the default value $a = 25$.

	δ (MPa$^{1/2}$)	χ (no units)			
		A	B	C	W
A	12.7	0			
B	13.6	1.23	0		
C	23.0	7.44	2.70	0	
W	47.8	3.36	1.53	1.48	0

The number density is $\rho = 3$, and the default interaction parameter $a = 25$. The unlike species interaction parameters, which were obtained via the Flory-Huggins χ-parameters by Wu et al., are summarised in Table 3.2.

In a simulation, we started with a simulation cell $L = 20 \times 20 \times 20$ in reduced DPD units (1 DPD unit corresponds to 0.814 nm), gradually increasing the number of water beads from the state of practically maximal draught, marked by $\lambda = 3$, towards maximum solvation at $\lambda = 120$. The total number of particles in the cell ranged from 24000 at $\lambda = 3$ up to 117600 at $\lambda = 120$.

For all the simulations we employed the DL_MESO package version 2.6. The time scale serving as a reduced unit was $\tau = 5.35$ ps, and the time step was set to $\Delta t = 0.05\tau$. Overall, each water content λ was simulated for 2.5 ns, which corresponded to 10k time steps. 40 different water contents were simulated. (see Fig. 3.1) The difference between consecutive water contents $\Delta\lambda$ was set such that the percentage difference was kept reasonably small. The total time of a swelling/drying simulation was 110 ns. We also tried a smaller simulation time per water content 1 ns, but this was not sufficiently long for equilibration.

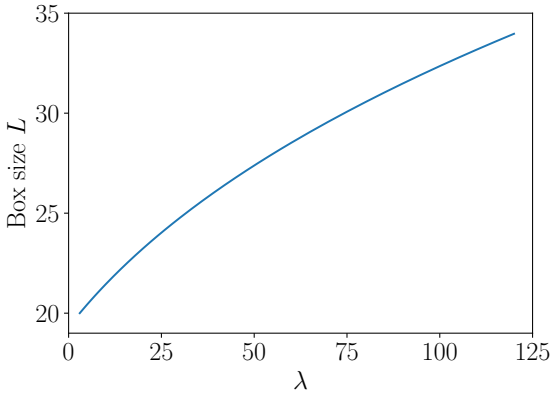

Figure 3.1: Evolution of the water content λ. Each value λ was simulated for 2.2 ns. Overall, 40 values of λ were simulated.

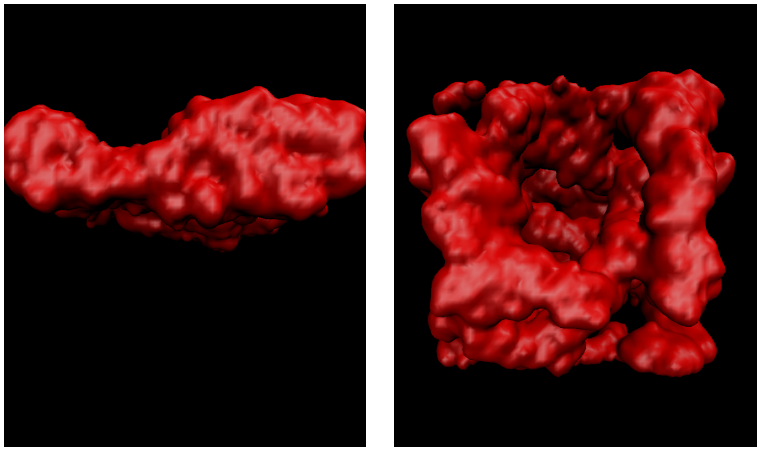

(a) Swelling, $\lambda = 120$

(b) Drying, $\lambda = 120$

Figure 3.2: Simulation cells depicting isosurfaces of PTFE backbone (A and B beads) for (a) swelling and (b) drying.

3.2 Chain behaviour

Visual observation of the simulation cells on Fig. 3.2 reveals a clear difference in the structure of the chains at maximal $\lambda = 120$. At the end of the swelling process, the chains shrink into a minimal volume, whereas starting the drying process with a randomly initialised configuration of bead positions leads to a maximal spread within the simulation cell.

To quantify these observations, we monitored the radius of gyration (RG) as well as the end-to-end distance (EE) of the Nafion polymer chains. RG is defined as:

$$R_{\mathrm{g}} = \frac{1}{N_{\mathrm{c}}} \sum_{i=1}^{N} (\mathbf{r}_i - \mathbf{r}_{\mathrm{com}})^2, \tag{3.1}$$

and EE as follows:

$$\langle R_{1,N} \rangle = \langle |\mathbf{r}_N - \mathbf{r}_1| \rangle, \tag{3.2}$$

where the average goes over the chains in the box as well as frames taken at various simulation times after the equilibration period.

The resulting evolutions of the EE and RG are shown on Fig. 3.3b and Fig. 3.3a respectively. According to these descriptors, the process of swelling and drying is reversible, as there is no difference between either route for a well-equilibrated system. The extremely dry state $\lambda = 3$

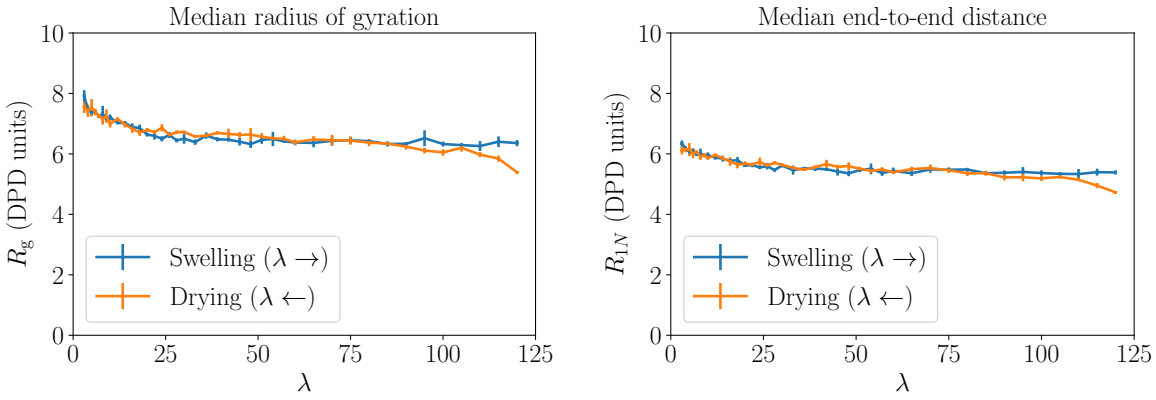

(a) (b)

Figure 3.3: (a) Radius of gyration and (b) end-to-end distance as a function of water content λ with errorbars. These descriptors yield similar trends, and same behaviour for swelling and drying apart from very high water contents $\lambda > 100$.

Figure 3.4: Visualisations of single backbone chains for (a) swelling and (b) drying reveal sphere-like clusters, as opposed to polymer rods posited by Gebel [1].

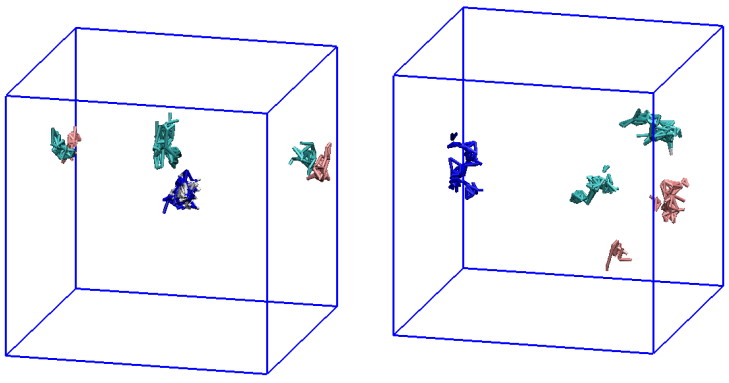

(a) Swelling, $\lambda = 120$ (b) Drying, $\lambda = 120$

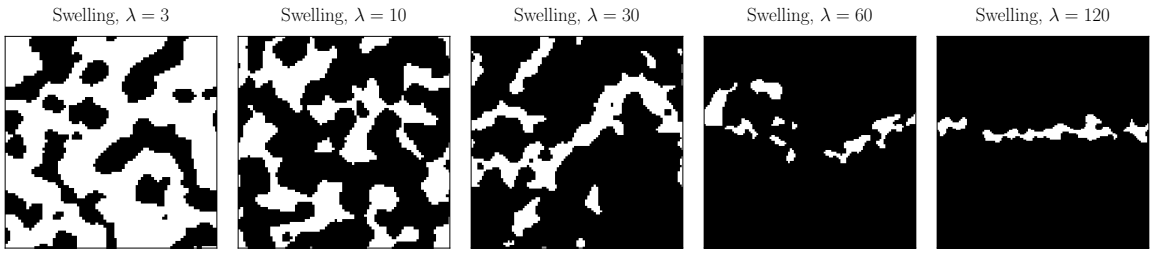

Figure 3.5: Visual evolution of water clustering as a function of water content in the process of swelling.

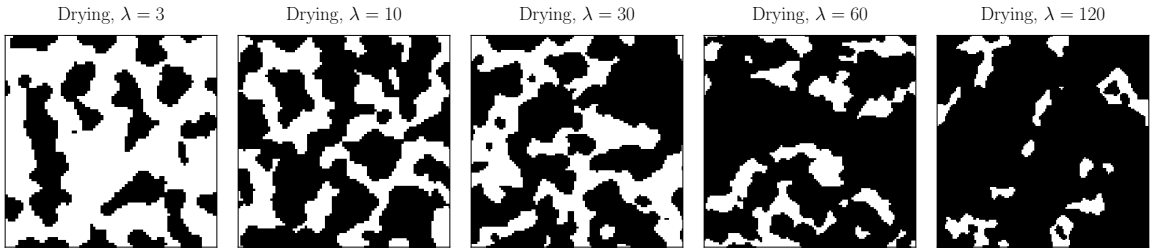

Figure 3.6: Visual evolution of water clustering as a function of water content in the process of drying.

manifests itself with a large size of the chains. Otherwise, there is no discontinuity or a local maximum that should point at a sudden change of structure.

As a final check on the chain behaviour we chose the principal component analysis (PCA).[1] This descriptor yields the principal axes in which a set of points in space (in our case monomers) is oriented, and eigenvalues μ_i representing their lengths. Hence, PCA should be more suitable than either radius of gyration or end-to-end distance to capture the asymmetric orientation of the chains. However, as Fig. 3.7 shows, there is no feature in the dependence of the largest eigenvalue on water content λ that would expose a structure inversion from a spherical shape towards oriented polymer rods, which as proposed by Gebel [1]. In fact, these curves are qualitatively the same as those representing RG and EE. Visualisations of single backbone chains in simulation cells shown on Fig 3.4 expose chains forming sphere-like globules and not elongated polymer rods anticipated by Gebel, and thus confirm the findings reached by the PCA analysis. Hence, we conclude that Nafion remains structurally the same throughout both swelling and drying process.

3.3 Water clustering and percolation

To gain insight into the structure of water, we monitored the percolation of water clusters and channels. After computing the density profile by smearing each bead on a grid using a Gaussian function, we selected the regions where water density $\rho_{\text{water}} > 0.1\rho = 0.3$.

The change in clustering with increasing and decreasing water content λ can be qualitatively observed in Fig. 3.5 and Fig. 3.6, respectively, which depict cuts through the simulation cell. There is a clear difference at hight water contents, where, in case of drying, the polymer chains

[1] Also known as singular value decomposition.

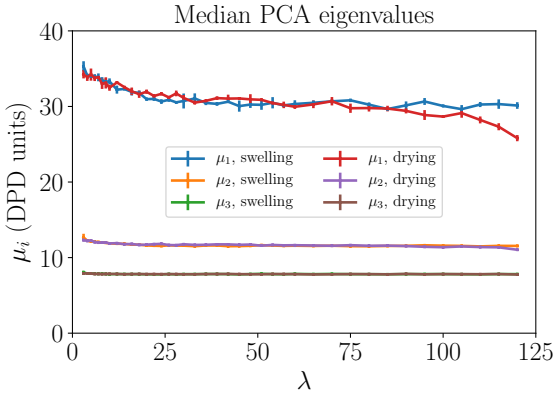

Figure 3.7: Eigenvalues μ_i from the principal component analysis (PCA) of the Nafion chains as a function of water uptake.

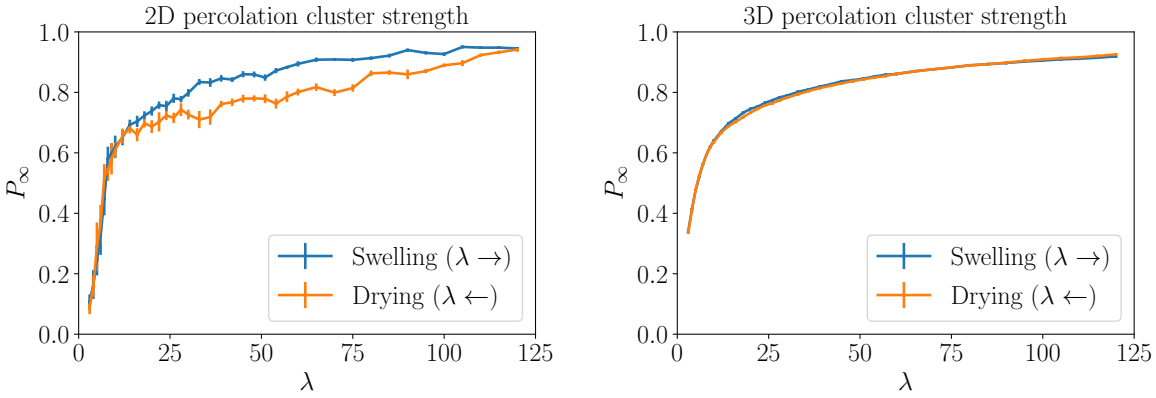

(a) (b)

Figure 3.8: (a) Percolation cluster strength in two dimensions with errorbars computed from the clustering images shown in Fig. 3.5 and 3.6. Despite a considerable level of noise, this descriptor also reveals a clear separation of the drying and swelling process at $\lambda > 20$. (b) The same quantity in three dimensions reveals no significant difference between swelling and drying.

are visibly more spread, whereas the swelling reduces them to a narrow strip.

To put these observations on solid quantitative footing, we computed the percolation cluster strength P_∞, which is defined as the ratio of the largest cluster to the size of the simulation cell, using the flood fill algorithm. This descriptor can be calculated in either two dimensions for a cut through a plane, or three for the whole simulation cell. The meaning of the quantity P_∞ is in that captures the spread of water through the system.

The resulting evolution of two-dimensional P_∞ with drying and swelling, shown on Fig. 3.8a, demonstrates a clear difference between the two simulation routes. During the swelling, water is on average more spread in the cell than during the drying process. On the other hand, 3D P_∞ on Fig. 3.8b reveals almost no difference between swelling and drying.

3.3.1 Simulation pressure

The DPD simulations run at NVT ensemble and the pressure cannot be relaxed to let sudden changes in the volume manifest themselves. On the other hand, monitoring the pressure of a

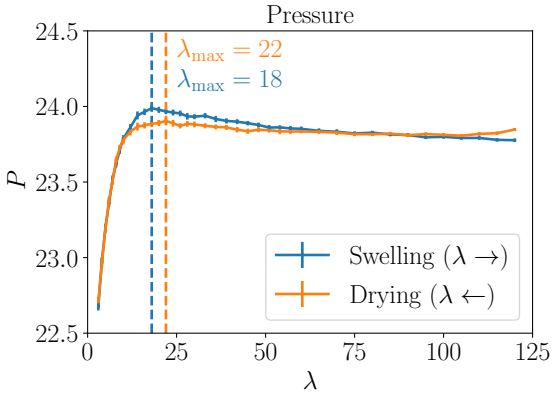

Figure 3.9: Pressure as a function of water uptake shows a maximum around $\lambda = 20$ for both swelling and drying.

system at constant volume (and hence density) provides a new insight into the behaviour.

The evolution of pressure on Fig. 3.9 with water content reveals a pronounced maximum at $\lambda = 18$ (percentage volume 0.4) for swelling and a flatter one at $\lambda = 22$ (0.45) for drying. The sharp increase in pressure at low values of λ before these maxima suggests that, in a constant pressure environment, the membrane would tend to expand and at the same time reduce its density.

3.4 Conclusion

We have demonstrated via simulation that the structure of bulk Nafion at high water contents is slightly different depending on the way it is prepared. At the same time, there is no sharp transition in the microscopic behaviour of PTFE chains, as determined by computing the end-to-end distance, the radius of gyration or performing the principal component analysis.

The structural inversion first suggested by Gebel [1] at water volume fraction 0.5 (equivalent to water content $\lambda = 27$), which results in a connected network of polymer rods, is not supported by simulation. Our results imply that gradual swelling produces a compact structure of chains packed next to one another with large water pool outside, as opposed to a porous polymeric structure with water spread everywhere in case of starting from the dissolved state.

Chapter 4

Revisiting the scaling in DPD

> In mathematics, you don't learn things.
> You just get used to them.
>
> *John von Neumann*

This chapter attempts to resolve long-standing ambiguities about the dependence of the DPD interaction parameter on temperature as well the resulting experimental observables on the coarse graining degree. We revisit the role of this parameter in DPD simulations and derive the scaling of the input variables such that experimentally observable outputs do not scale. We illustrate the versatility of this modification by computing surface tensions of three mixtures.

Coarse-grained molecular dynamics (MD) contains, in addition to the usual force field- or thermostat-related parameters associated with atomistic MD, another parameter: coarse-graining (CG) degree, which provides the freedom to trade off between simulation speed and spatial or temporal resolution. As CG degree is a theoretical construct without experimental substance, the physical properties of a simulated system must be the same, or at least as similar as possible, at different scales, i.e. over a range of CG degrees.

Materials simulations are usually performed using reduced units in order to avoid extremely small or large numbers and prevent the arithmetic underflow or overflow. Some CG simulation methods, such as dissipative particle dynamics (DPD) widely used for soft matter, work in units where the length scale is defined from the reduced density and the CG degree, both of which one is free to choose [7]. As a result, the conversion from real to reduced units while preserving the physical properties has been rather ambiguous, and the comparison of same physical settings simulated at different CG degrees nearly impossible. The purpose of this chapter is to address this challenge through a consistent scaling approach.

The standard version of DPD has been successfully applied to a wide range of soft matter systems in the past two decades [27]. Besides, a many-body dissipative particle dynamics (MDPD) has been proposed by adding a density-dependent term into the force field [35, 36, 37]. This version is thus capable of simulating non-ideal fluids and free surfaces, and hence covering a much wider range of systems of practical interest [39].

Unfortunately, no general protocol for deriving the MDPD interaction parameters for real materials has been proposed so far. In case of standard DPD, the sole parameter a is obtained by matching the compressibility to an equation of state (EOS) of a pure liquid, and cross-interaction parameters for mixtures are based on some mean-field approximation, such as Flory-Huggins theory. However, in case of MDPD, the choice has so far been ad hoc [41, 40, 40, 42].

Furthermore, there has been much discussion about how the DPD interaction parameter should scale with the coarse-graining (CG) degree. Groot and Rabone [83] originally suggested a linear dependence, but this was refuted independently by Maiti and McGrother [93] and Füchslin *et al.* [30]. Maiti and McGrother also proposed linear scaling for the χ-parameter with the aim of reproducing the experimental surface tensions. However, we have found inconsistencies in their reasoning. In case of MDPD, to our knowledge there have been no predictions of the surface tension for real mixtures and consequently no discussion of the scaling.

The aim of this chapter is to present a general protocol to determine the interaction parameters as a function of not only material properties, such as compressibility, but also the coarse-graining degree and temperature. To achieve this, we first need to discuss the choice and role of the reduced units. We revisit and restate the derivation presented by Füchslin *et al.*, and correct the temperature-dependence of the interaction parameter originally proposed by Groot and Warren (GW). More importantly, we explain the derivation and the reasoning behind the scaling of the Flory-Huggins χ-parameter, a key variable determining the mixing properties of soft matter. Consequently, demonstrate the improved predictive accuracy of these methods across a range of CG degrees.

4.1 Summary of reduced units and parameterisation in DPD

The DPD force field is summarised in Section 1.3 of the Introduction. We define the reduced units of length, mass and energy $r_\mathrm{c} = m_\mathrm{c} = k_\mathrm{B}T_\mathrm{c} = 1$, where T_c is a user-selected reference temperature, and, in the following, denote all variables in reduced units by a diacritical tilde, following the convention set by Füchslin *et al.* [30]. The conversion is, for example, $\tilde{r} = r/r_\mathrm{c}$, $\tilde{m} = 1 = m/m_\mathrm{c}$, since all the masses are assumed to be same or very similar, and $\widetilde{k_\mathrm{B}T} = k_\mathrm{B}T/k_\mathrm{B}T_\mathrm{c}$, where $k_\mathrm{B}T_\mathrm{c}$ is the energy scale based on the chosen temperature.

In case of a single-component DPD fluid, this force field is sufficiently simple that its EOS can be easily reverse-engineered, as GW did [7]:

$$\tilde{p} = \tilde{\rho}\widetilde{k_\mathrm{B}T} + \tilde{\alpha}\tilde{a}\tilde{\rho}^2, \tag{4.1}$$

where $\tilde{\rho}$ is number density, and $\tilde{\alpha}$ a fitting constant, which was shown to be approximately 0.1 for $\tilde{\rho} > 3$. To derive $\tilde{a}$, these authors matched the EOS to the isothermal compressibility κ. From definition,

$$\kappa^{-1} = \rho\left(\frac{\partial p}{\partial \rho}\right)_T, \tag{4.2}$$

and, in reduced units,

$$\tilde{\kappa}^{-1} = \tilde{\rho}\left(\frac{\partial \tilde{p}}{\partial \tilde{\rho}}\right)_{\tilde{T}} = \tilde{\rho}\widetilde{k_\mathrm{B}T} + 2\tilde{\alpha}\tilde{a}\tilde{\rho}^2. \tag{4.3}$$

Considering water with compressibility $\kappa \approx 4.5 \times 10^{-10}$ Pa^{-1}, which can be non-dimensionalised to $\kappa_{\mathrm{nd}}^{-1} = 1/(\kappa n k_{\mathrm{B}} T)$, where T is absolute temperature and n is molecular number density, and making the choice that one DPD particle (*bead*) contains one molecule, the interaction parameter $\tilde{a}$ derived by GW for room temperature, when $\kappa_{\mathrm{nd}}^{-1} \approx 16$ (below eq. (16) in their paper [7]), is:

$$\tilde{a} = \frac{\kappa_{\mathrm{nd}}^{-1} - 1}{2\tilde{\alpha}\tilde{\rho}} \widetilde{k_{\mathrm{B}}T} = 25\, \widetilde{k_{\mathrm{B}}T}. \tag{4.4}$$

Note that a has the dimension of force, i.e. $k_{\mathrm{B}}T_{\mathrm{c}}/r_{\mathrm{c}}$, but r_{c} in the denominator is set to 1.

To bridge the simulation method with real materials, Groot and Rabone defined the length scale (and interaction cutoff at the same time) r_{c} as follows:

$$r_{\mathrm{c}} = (\tilde{\rho} N_{\mathrm{m}} V_0)^{1/3}, \tag{4.5}$$

where V_0 is the volume of a single water molecule. These authors consequently derived that parameter $\tilde{a}$ should scale linearly with the number of molecules in a bead, i.e. CG degree N_{m}: $\tilde{a}(N_{\mathrm{m}}) = N_{\mathrm{m}}\tilde{a}(1)$. However, their reasoning was refuted by Füchslin *et al.*, who showed that, in real units, the scaling is a power law: $a(N_{\mathrm{m}}) = N_{\mathrm{m}}^{2/3} a(1)$. More importantly, in reduced units the interaction parameter does *not* scale: $\tilde{a}(N_{\mathrm{m}}) = 25$.

4.1.1 Temperature dependence

Here we show that the temperature scaling of GW needs to be reconsidered. We start by noting that in practice there are two equivalent ways to define the reduced units: either $k_{\mathrm{B}}T = k_{\mathrm{B}}T_{\mathrm{c}}$ and so $\widetilde{k_{\mathrm{B}}T}$ is always held at 1, in which case the EOS is reduced to

$$\tilde{p} = \tilde{\rho} + \tilde{\alpha}\tilde{a}\tilde{\rho}^2, \tag{4.6}$$

as was already pointed out by Maiti *et al.* [93]. A more practical approach is to decide a base temperature T_{c}, e.g. 300 K, and thus define the energy scale $k_{\mathrm{B}}T_{\mathrm{c}} = 1$. This enables varying the temperature in the simulation by setting $\widetilde{k_{\mathrm{B}}T}$ to, e.g. 2, and the EOS then becomes

$$\tilde{p} = \tilde{\rho}\widetilde{k_{\mathrm{B}}T} + \tilde{\alpha}\tilde{a}\tilde{\rho}^2. \tag{4.7}$$

We consider here the latter option, for which the EOS looks the same in real units: $p = \rho k_{\mathrm{B}}T + \alpha a \rho^2$. Hence, we can obtain an unambiguous value of the interaction parameter via the compressibility match:

$$\kappa^{-1} = \rho \left(\frac{\partial p}{\partial \rho} \right)_T = \rho k_{\mathrm{B}}T + 2\alpha a \rho^2, \tag{4.8}$$

from which it follows that

$$a = \frac{\kappa^{-1} - \rho k_{\mathrm{B}}T}{2\alpha\rho^2}. \tag{4.9}$$

So in real units a *decreases* linearly with temperature. Consider here a DPD fluid where one bead corresponds to one molecule, so $N_{\mathrm{m}} = 1$. Using dimensional analysis, the conversion to

reduced units is as follows:[1]

$$p = \tilde{p}\frac{k_\mathrm{B}T_\mathrm{c}}{r_\mathrm{c}^3}, \quad a = \tilde{a}\frac{k_\mathrm{B}T_\mathrm{c}}{r_\mathrm{c}}, \quad \alpha = \tilde{\alpha}\, r_\mathrm{c}^4, \quad \rho = \tilde{\rho}\frac{1}{r_\mathrm{c}^3}. \tag{4.10}$$

To non-dimensionalise the compressibility we cannot use the same approach as GW, who took the molecular density $n = 1/V_0$ instead of the DPD density ρ. These are only equal to each other in the special case $N_\mathrm{m} = 1$.

To better illustrate this point and also expose the strength of the dimensional analysis, we note that the inverse compressibility has the same dimensions as pressure:

$$\tilde{\kappa}^{-1} = \kappa^{-1}\frac{r_\mathrm{c}^3}{k_\mathrm{B}T_\mathrm{c}} = \kappa^{-1}\frac{\tilde{\rho}V_0}{k_\mathrm{B}T_\mathrm{c}}. \tag{4.11}$$

On the other hand, the compressibility due to GW is:

$$\kappa_\mathrm{nd}^{-1} = \kappa^{-1}\frac{1}{nk_\mathrm{B}T_\mathrm{c}} = \kappa^{-1}\frac{V_0}{k_\mathrm{B}T_\mathrm{c}}. \tag{4.12}$$

By rearranging these equations we see that these are not equal, but differ by the DPD density: $\tilde{\kappa}^{-1} = \tilde{\rho}\kappa_\mathrm{nd}^{-1}$.

Non-dimensionalising eq. (4.9) by inserting eq. (4.10), we obtain the following expression for the interaction parameter in reduced units:

$$\tilde{a} = \frac{\tilde{\kappa}^{-1} - \tilde{\rho}\widetilde{k_\mathrm{B}T}}{2\tilde{\alpha}\tilde{\rho}^2}, \tag{4.13}$$

and, inserting $\tilde{\kappa}^{-1} = \tilde{\rho}\kappa_\mathrm{nd}^{-1}$ for clarity:

$$\tilde{a} = \frac{\kappa_\mathrm{nd}^{-1} - \widetilde{k_\mathrm{B}T}}{2\tilde{\alpha}\tilde{\rho}}, \tag{4.14}$$

which, after setting $\widetilde{k_\mathrm{B}T} = 1$ and $\kappa_\mathrm{nd}^{-1} = 16$, turns into the form due to GW: $\tilde{a} = 15/(2\tilde{\alpha}\tilde{\rho}) = 75/\tilde{\rho}$. This proves that our derivation based on dimensional analysis is a generalised version of the approach first used by GW.

We now see clearly (Fig. 4.1) that the interaction parameter $\tilde{a}$ decreases linearly with temperature in reduced units as well, as opposed to the linear increase derived by GW, assuming constant compressibility. For a bead containing one water molecule at DPD density $\tilde{\rho} = 3$, the temperature dependence is: $\tilde{a} = (16 - \widetilde{k_\mathrm{B}T})/0.6$.

It must be noted that this temperature dependence is very weak and, for most practical purposes, can be neglected. For example, at 373 K, which is probably the highest temperature at which one would want to simulate liquid water, $\widetilde{k_\mathrm{B}T} \approx 1.25$, and $\tilde{a}$ changes to ≈ 24.6, which is only a 2% difference from $\tilde{a} = 25$ at 300 K. However, this variation becomes more relevant if one aims to explore materials at extreme temperatures.

In our analysis so far the compressibility was considered independent of temperature. This

[1] That the dimension of fitting parameter α is r_c^4 can be ascertained from eq. (9) in Ref. [37].

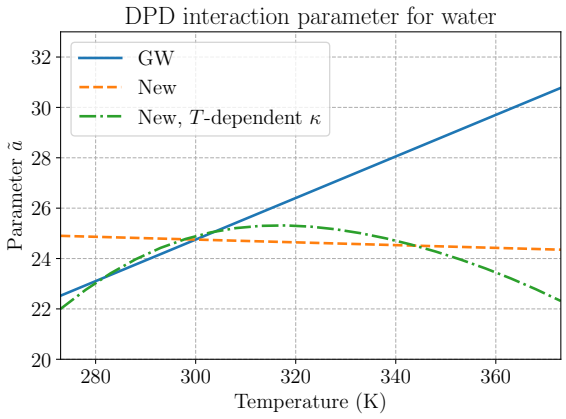

Figure 4.1: Temperature dependence of interaction parameter $\tilde{a}$ in reduced units in the range where water is liquid at ambient pressure, comparing the formula due to GW and our revisited derivation, and the effect of temperature dependence of compressibility.

might be an overly crude approximation, as, in case of water, the variation is about 10% between 0 and 50 °C [94]. However, the framework presented above enables easy inclusion of this variation by first choosing energy scale $k_\mathrm{B}T_\mathrm{c}$ and simulation temperature $\widetilde{k_\mathrm{B}T}$, finding the experimental value of κ at the given $k_\mathrm{B}T = \widetilde{k_\mathrm{B}T}\,k_\mathrm{B}T_\mathrm{c}$, and finally non-dimensionalising κ with respect to $k_\mathrm{B}T_\mathrm{c}$ to obtain $\tilde{\kappa}$. Fig. 4.1 shows the effect of temperature dependence of compressibility.

4.2 Scaling with coarse-graining degree

Having understood the temperature dependence of the DPD potential, we now turn to the scaling with respect to the coarse-graining degree N_m, which is defined as the number of molecules in one bead. As mentioned above, Füchslin *et al.* have proposed that the interaction parameter scales with $N_\mathrm{m}^{2/3}$ in real units and remains scale-invariant in reduced units [30]. We reproduce this derivation with simple arguments of dimensionality. Thus we will be able to intuitively track the scaling of separate variables, which would otherwise get complicated due to the fact that the length scale r_c depends on N_m.

As a first step, we convert the density from reduced to real units. Knowing that the density of unscaled, $N_\mathrm{m} = 1$ liquid is $\rho(1) = 1/V_0 = n$, it follows that

$$\rho(N_\mathrm{m}) = \frac{\tilde{\rho}(N_\mathrm{m})}{r_\mathrm{c}^3} = \frac{\tilde{\rho}(1)}{N_\mathrm{m} r_\mathrm{c}^3} = \frac{n}{N_\mathrm{m}}, \tag{4.15}$$

where r_c is a function of N_m as well. We also note that the reduced density is set regardless of the CG degree, so $\tilde{\rho}(N_\mathrm{m}) = \tilde{\rho}(1)$. Knowing the relation between real and reduced variables, we can now figure out the EOS of a coarse-grained liquid:

$$p = \frac{\rho}{N_\mathrm{m}} k_\mathrm{B}T + \alpha a \frac{\rho^2}{N_\mathrm{m}^2}. \tag{4.16}$$

For $N_\mathrm{m} = 1$, this simply reduces to the known form $p = \rho k_\mathrm{B}T + \alpha a \rho^2$. For a general N_m, we denote all the variables with a prime: $p' = \rho' k_\mathrm{B}T' + \alpha' a' \rho'^2$, where $\rho' = \rho/N_\mathrm{m}$. Now we need to decide which quantity is scale-invariant. Like Füchslin *et al.*, we choose pressure, which is an experimental observable, so $p = p'$. In principle, other variables can be thus chosen. Starting

from $r_c(N_m) = (\tilde{\rho} N_m V_0)^{1/3} \sim N_m^{1/3}$, we can derive how the quantities of interest change with the CG degree:

$$\rho'(N_m) \sim N_m^{-1}, \tag{4.17}$$

$$k_B T'(N_m) \sim N_m, \tag{4.18}$$

$$\alpha'(N_m) \sim N_m^{4/3}, \tag{4.19}$$

$$a'(N_m) = a N_m N_m^{-1/3} \sim N_m^{2/3}. \tag{4.20}$$

It might seem surprising that to keep the ideal gas term of the EOS scale-invariant, the energy $k_B T$ should depend on the CG degree. To keep the temperature scale-invariant, this implies that the Boltzmann constant k_B must scale linearly with N_m. This is correct, since the dimension of the Boltzmann constant is J/K, and energy was from the very beginning decided to scale linearly, whereas temperature was kept constant.

Importantly, and as already mentioned, the interaction parameter expressed in reduced units is scale-invariant:

$$\begin{aligned} \tilde{a}' &= a' \frac{r_c(N_m)}{k_B T(N_m)} \\ &= a N_m^{2/3} \frac{r_c(N_m)}{k_B T(N_m)} = \tilde{a} \frac{k_B T}{r_c} \frac{r_c(N_m)}{k_B T(N_m)} N_m^{2/3} = \tilde{a}. \end{aligned} \tag{4.21}$$

This is the main and somewhat understated point from the paper by Füchslin *et al.*: assuming we do not enforce any constraints from the outside apart from the invariance of the compressibility, *all* the quantities in reduced units remain scale-invariant with respect to the coarse-graining. This means that any DPD simulation with water serving as the solvent should be done at $\tilde{a} = 25$. What matters is how we map the results back to the real units after the simulation. This has an important positive side effect in that the interaction parameter does not become too high at high CG degrees, which could lead to freezing, a generally undesirable phenomenon in simulations of liquids [95].

Finally, we derive the scaling of time and the friction constant γ from dimensional analysis:

$$\tau = \sqrt{\frac{m(N_m) r_c^2(N_m)}{k_B T(N_m)}} \sim \left(\frac{N_m N_m^{2/3}}{N_m} \right)^{1/2} = N_m^{1/3}, \tag{4.22}$$

$$\gamma \sim \frac{m_0(N_m)}{\tau(N_m)} \sim \frac{N_m}{N_m^{1/3}} = N_m^{2/3}. \tag{4.23}$$

Füchslin *et al.* wrote that there is a gauge freedom in choosing the scaling of time, but in fact this exponent is determined by the decision to keep pressure scale-invariant.

However, a problem now arises. Füchslin *et al.* decided to constrain the three basic units, length, mass, and energy, in such a way that pressure, compressibility, or any other quantity with the same dimension will be constant across all the scales. But liquid compressibility is not the only property that should be kept constant. In general, any experimental observable should behave so. This is not a priori guaranteed by Füchslin's scaling scheme.

Consider surface tension and self-diffusivity, two important simulation outputs. The dimen-

sional analysis reveals their scale dependence:

$$\sigma \sim \frac{k_\mathrm{B}T_\mathrm{c}(N_\mathrm{m})}{r_\mathrm{c}^2(N_\mathrm{m})} \sim \frac{N_\mathrm{m}}{N_\mathrm{m}^{2/3}} = N_\mathrm{m}^{1/3}, \tag{4.24}$$

$$D \sim \frac{r_\mathrm{c}(N_\mathrm{m})^2}{\tau(N_\mathrm{m})} \sim \frac{N_\mathrm{m}^{2/3}}{N_\mathrm{m}^{1/3}} = N_\mathrm{m}^{1/3}. \tag{4.25}$$

Clearly, these experimental observables vary with CG degree, which is undesirable, as CG degree is a simulation parameter without physical nature.

The way to rectify this problem is add an appropriate scaling of the reduced units $\tilde{D}, \tilde{\sigma}$ such that these will become scale-invariant after conversion to real units. To achieve this, we need to understand how these observables depend on the underlying simulation inputs, such as the interaction parameter $\tilde{a}$, the Flory-Huggins χ-parameter, or the friction $\tilde{\gamma}$. To simplify our analysis as much as possible, we will restrict ourselves to either pure liquids or binary mixtures.

4.2.1 Surface tension

We first turn to the surface tension, which was extensively discussed by Maiti *et al.* [93]. Starting from the Hildebrand solubilities δ_i of species i, a simple model for the χ-parameter is

$$\chi_{ij} = \frac{V}{k_\mathrm{B}T}(\delta_i - \delta_j)^2, \tag{4.26}$$

where V is the bead volume, Maiti derived a linear dependence of the χ-parameter on N_m from the fact that the bead volume varies linearly with the solubilities [93].

There are two problems with this line of reasoning, a technical and a theoretical one. Technically, these authors kept the energy scale $\widetilde{k_\mathrm{B}T}$ invariant. If we corrected this, we would find out that χ is invariant, which would lead, together with invariant $\tilde{a}$, to invariant surface tension $\tilde{\sigma}$. However, this would imply the scale dependence of σ, which is undesirable.

The theoretical objection is that mixing is a delicate interplay of various effects on the microscale and it is not a priori clear how these should vary on the number of molecules bundled into a bead. This bundling – the coarse-graining – is in itself an artificial process without any physical substance, the sole aim of which is speeding up the simulation.

In order to derive a plausible scaling of $\tilde{\sigma}$ we follow a different route, which will not require diving into the complex microscopic origin of mixing. We start from the dependence of surface tension on the χ-parameter derived by GW in the context of the DPD (eq. (36) in their paper, with $\tilde{\rho}$ being density and assuming $k_\mathrm{B}T = 1, r_\mathrm{c} = 1$):

$$\tilde{\sigma} = \begin{cases} 0.75\tilde{\rho}\chi^{0.26}\left(1 - \frac{2.36}{\chi}\right)^{3/2} & \chi > 2.36 \\ 0, & \chi \leq 2.36. \end{cases} \tag{4.27}$$

To render $\tilde{\sigma}$ scale-invariant, we need to determine the scaling of the χ-parameter such that

Table 4.1: Solubilities δ, χ-parameters and surface tensions σ_{expt} of water-liquid interface, taken from Maiti *et al.* [93].

Component	$\delta(\text{MPa}^{1/2})$	χ	σ_{expt} (mN/m)
Water	47.9		
Benzene	18.6	6.132	35.0
CCl_4	17.8	6.474	45.0
Octane	15.6	7.555	51.7

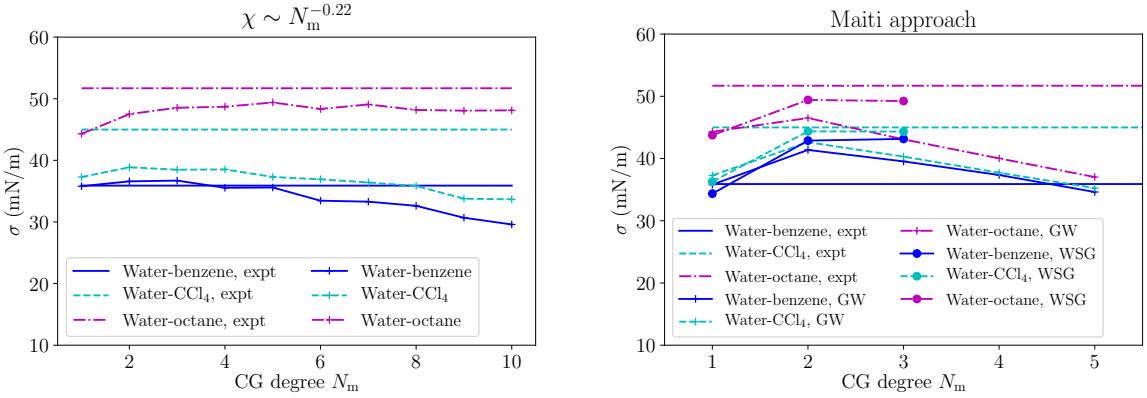

(a) (b)

Figure 4.2: Variation of surface tension for three mixtures with coarse-graining degree: (a) our derivation using the fine-tuned scaling of χ-parameter, and (b) methodology by Maiti [93], working up to $N_m = 5$, for both GW and Wijmans, Smit and Groot (WSG) $\Delta a - \chi$ relation.

$\tilde{\sigma} \sim N_m^{-1/3}$. In other words, we are looking for the exponent β such that

$$\begin{aligned} \sigma &= \tilde{\sigma}\frac{k_B T_c(N_m)}{r_c(N_m)^2} \\ &= 0.75\tilde{\rho}(\chi N_m^{\beta})^{0.26}\left(1-\frac{2.36}{\chi N_m^{\beta}}\right)^{3/2}\frac{k_B T_c}{r_c^2}\frac{N_m}{N_m^{2/3}} \sim \text{constant}. \end{aligned} \tag{4.28}$$

Due to the rather complex power law of eq. (4.27), we resort to numerical minimisation after defining the relevant range of CG degrees. Although it might be desirable to try to deliver a perfect analytical solution, given the overall qualitative nature of the DPD, a reasonably accurate approximation is sufficient for practical simulations.

We consider the mixtures explored by Maiti, that is water-benzene, water-CCl_4, and water-octane. Their χ-parameters are computed from the Hildebrand solubilities, and the data are summarised in Table 4.1. Defining the range of CG degrees $N_m \in \{1, 2, ..., 10\}$ and the root mean-square error

$$\text{RMSE} = \sqrt{\frac{1}{N_{N_m} - 1}\sum_{N_m}(\sigma_1 - \sigma_{N_m})^2}, \tag{4.29}$$

we can minimise the RMSE across these mixtures. Hence, we arrive at the scaling of the χ-parameter $\chi \sim N_m^{-0.22}$.

To test this scaling, we performed simulations in the LAMMPS software package [96]. We

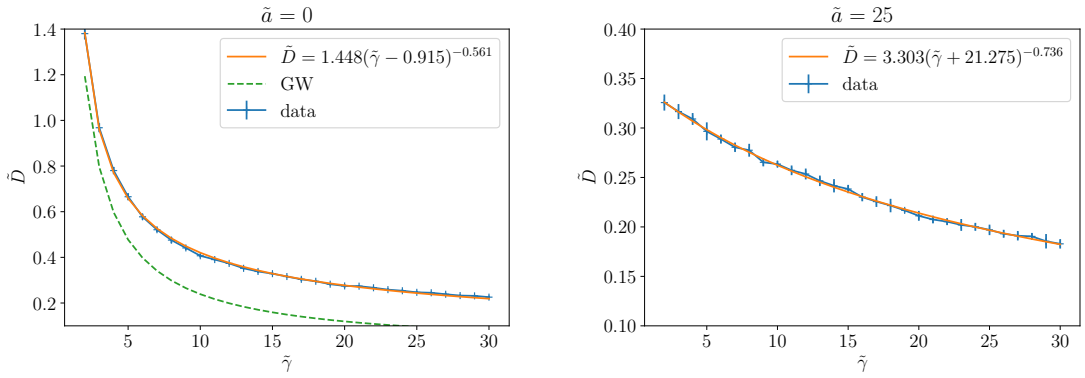

(a) (b)

Figure 4.3: Self-diffusivity dependence with error bars for (a) $\tilde{a} = 0$, i.e. no conservative interaction, and (b) $\tilde{a} = 25$ with power law fits (equations shown in inset).

set a $20 \times 10 \times 10$ orthorhombic cell at density $\tilde{\rho} = 3$. The time step was set to 0.05. Taking water as the default liquid, the volume of a bead containing one molecule was $V_0 = 30$ Å, and the like bead repulsion $\tilde{a}_{ii} = 25$. We equilibrated the system for 20000 steps and collected data for another 50000 steps. The surface tension was calculated from the pressure tensor components:

$$\tilde{\sigma} = \frac{\tilde{L}_x}{2}\left(\langle \tilde{p}_{xx} \rangle - \frac{\langle \tilde{p}_{yy} \rangle + \langle \tilde{p}_{zz} \rangle}{2}\right). \tag{4.30}$$

In parallel, we have reproduced the measurements by Maiti *et al.* These workers tested two various relations for Δa vs χ: a linear one derived by GW:

$$\Delta a = \chi / 0.286, \tag{4.31}$$

which we used for our simulations as well, and a quadratic one derived by Wijmans, Smit and Groot (WSG) [33]:

$$\frac{\chi}{\Delta a} = 0.3 - \frac{0.3 - 0.2}{115 - 15}(\Delta a - 15). \tag{4.32}$$

Both of these approaches, if scaled linearly with N_m, lead to extremely large excess repulsions Δa and allow CG degrees only up to $N_\mathrm{m} = 5$ and 3, respectively.

Fig 4.2 shows the results of analytical predictions and simulations using the scaling arguments presented above, and the approach by Maiti *et al.* Our method gives satisfactory results for water-benzene and water-octane mixtures for CG degrees up to $N_\mathrm{m} = 10$ and possibly even above. The water-CCl_4 mixture starts from an incorrect position at $N_\mathrm{m} = 1$, which might be due to the inability of the overly simple eq. (4.26) to describe real behaviour. Overall, our derived scaling of $\chi \sim N_\mathrm{m}^{-0.22}$ is able to capture the mixing properties over a wide range of CG degrees and improve the predictive accuracy of mixing in DPD.

4.2.2 Self-diffusivity

The friction parameter $\tilde{\gamma}$ from the dissipative and random force (eq. (1.9)) is another microscale parameter that influences the self-diffusivity D, which can be measured experimentally. Overall,

bead diffusion depends not only on γ, but also on the particle repulsion a. There have been attempts to analytically derive how γ should vary with the CG degree [97]. Nonetheless, we can easily derive the scaling that renders the self-diffusivity constant across different CG degrees.

To understand the behaviour of a pure DPD liquid, we exploit the fact that the low number of simulation parameters enables fast exploration of a large portion of the parameter space. Defining the self-diffusivity from the MSD:

$$\tilde{D} = \lim_{\tilde{t}\to\infty} \frac{\tilde{r}(\tilde{t})^2}{6\tilde{t}}, \quad D = \tilde{D}\frac{r_\mathrm{c}^2}{\tau}, \tag{4.33}$$

we have measured the dependence of $\tilde{D}$ for a wide range of $\tilde{\gamma}$ values between 2 and 30, and $\tilde{a}$ values between 0 and 55. Using $10 \times 10 \times 10$ orthorhombic cell with 3000 beads, we have equilibrated for 40k steps and measured the MSDs for 1000 steps 10 times in succession to eliminate noise. We took a smaller time step 0.03 to maintain the temperature at $k_\mathrm{B}T = 1$, as it tends to diverge with increased friction.

Firstly, we consider the case where $\tilde{a} = 0$, i.e. beads interact only via the dissipative and random force. In this case, using mean-field approximation by setting $g(r) = 1$ GW derived analytically $D = 45/(2\pi\gamma\rho r_\mathrm{c}^3)$ or, in reduced units, $\tilde{D} = 45/(2\pi\tilde{\gamma}\tilde{\rho})$ [7]. From simulations we obtained systematically higher values, as shown on Fig. 4.3 (left). For all the interaction parameters $\tilde{a}$, it is possible to fit the self-diffusivity with the power law of the form:

$$\tilde{D}(\tilde{\gamma}) = c_1(\tilde{\gamma} - c_2)^{c_3}, \tag{4.34}$$

where $c_i, i \in \{1, 2, 3\}$ are fitting parameters. We also tried to fit the self-diffusivities for both a and γ at once via

$$\tilde{D}(\tilde{\gamma}, \tilde{a}) = c_1(\tilde{\gamma} - c_2\tilde{a})^{c_3}, \tag{4.35}$$

but this failed to achieve a desired accuracy, especially at low frictions. This is not an important obstacle, since most simulations are done with water as the default bead type with the repulsion $\tilde{a} = 25$. Hence, to derive the scaling of $\tilde{\gamma}$ with the CG degree, it is sufficient to focus only on this value.

As before with the surface tension, our aim is to obtain the exponent β such that:

$$D = \tilde{D}\frac{r_\mathrm{c}(N_\mathrm{m})^2}{\tau(N_\mathrm{m})} \tag{4.36}$$

$$= 3.303(\tilde{\gamma}N_\mathrm{m}^\beta + 21.275)^{-0.736}\frac{r_\mathrm{c}^2}{\tau}\frac{N_\mathrm{m}^{2/3}}{N_\mathrm{m}^{1/3}} \sim \text{constant}. \tag{4.37}$$

Starting from $\tilde{\gamma}(1) = 4.5$ at $N_\mathrm{m} = 1$ used by GW, we have minimised the RMSE defined as in eq. (4.29) for $N_\mathrm{m} \in \{1, ..., 10\}$, and obtained $\beta = 1.13$. To verify this, we have again simulated pure liquids at $\tilde{a} = 25$ with $\tilde{\gamma} = \tilde{\gamma}(1)N_\mathrm{m}^{1.13}$. The results on Fig. 4.4 show a reasonably, if not perfectly flat curve, demonstrating the achieved scale invariance of water self-diffusivity in DPD.

Compared with the experimental self-diffusivity of water 2.3×10^{-9} m^2/s at 300 K, the values from DPD simulations are about 20 times larger. This is expected due to the extremely soft nature of DPD potential. To precisely target the experimental value, we would need to take

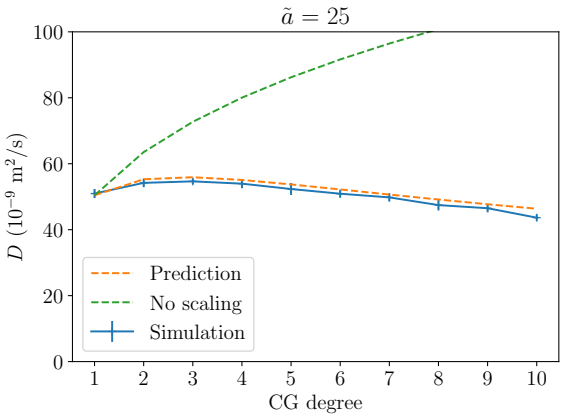

Figure 4.4: Self-diffusivity of DPD water (in SI units) as a function of the CG degree, performed at $\tilde{a} = 25$ and $\tilde{\gamma} = 4.5$ and plotted with or without the offsetting scaling of $\tilde{\gamma}$ with CG degree. Simulation results show agreement with the scaling $\tilde{\gamma} \sim N_{\mathrm{m}}^{1.13}$ predicted from eq. (4.37).

$\tilde{\gamma}$ of about 1500. Such a large value would severely impact the simulation efficiency in that the time step would have to be orders of magnitude smaller, and the speed of equilibration, which is one of the principal advantages of the DPD, would be lost. Nonetheless, having a method to generate scale-invariant, if shifted self-diffusivities can improve the insight into the dynamics of soft matter.

4.3 Relaxing the definition of r_{c}

Finally, we address an intriguing theoretical question, whether the definition of r_{c} can be relaxed by introducing general coefficients $\xi_{1,2}$, not necessarily equal to 1, such that

$$r_{\mathrm{c}} = (\tilde{\rho}^{\xi_1} N_{\mathrm{m}}^{\xi_2} V_0)^{1/3}. \tag{4.38}$$

Here, we prove that it cannot. Once the two elements from the set of three, containing the reduced density, CG degree, and r_{c} are decided, the third is automatically fixed, otherwise the mass would not be conserved. To this end, we devise a diagram scheme in 1D that should make our reasoning easy to follow.

4.3.1 Visualising the scaling and reduced units in one dimension

Assume a pure liquid in 1D, where all molecules are ordered on a line and obviously non-overlapping. The molecular number density in 1D is $n = 1/L_0$, where L_0 is a length occupied by one molecule. The definition of r_{c} changes slightly:

$$r_{\mathrm{c}} = \tilde{\rho} N_{\mathrm{m}} L_0. \tag{4.39}$$

We can illustrate a liquid by a following diagram depicting several molecules in a row. On x-axis is the distance (box size), on y-axis is the physical mass density ρ_{m}. So the mass of one molecule is $m_0 = \rho_{\mathrm{m}} L_0$. Hence, in our scheme, surface area has the meaning of the mass and so must be conserved.

Assume we choose a CG degree $N_{\mathrm{m}} = 2$ and reduced density $\tilde{\rho} = 1$. Then, the length scale $r_{\mathrm{c}} = 2L_0$, and from six molecules we get three beads:

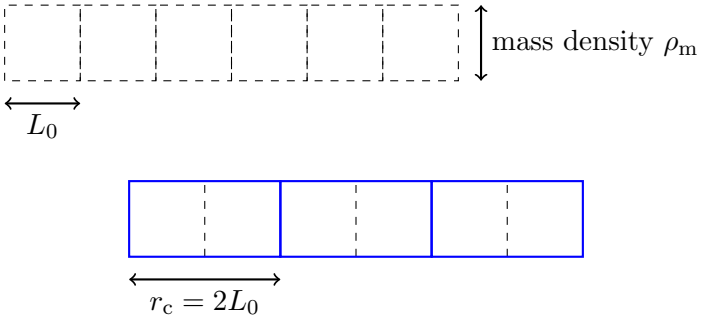

To illustrate the meaning of reduced density, choose a different parametrisation with $\tilde{\rho} = 3$ and $N_{\mathrm{m}} = 1$. This would mean that $r_{\mathrm{c}} = 3L_0$. In real units (denoted in red colour), non-coarse-grained liquid is the same as coarse-grained:

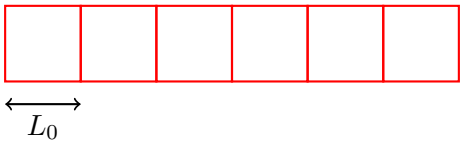

but in reduced units (denoted in blue colour), the partitioning changes:

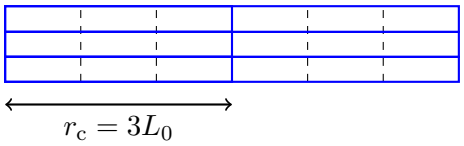

The blue rectangles correspond to the coarse-grained particles, and stacking of three on top of each other implies the chosen reduced number density $\tilde{\rho} = 3$. Note also that the area of one rectangle corresponds to the mass of one bead, which, in this case, is $m = N_{\mathrm{m}} m_0 = m_0$.

What if we chose $\tilde{\rho} = 3$ and $N_{\mathrm{m}} = 2$? Then, length scale would become $r_{\mathrm{c}} = \tilde{\rho} N_{\mathrm{m}} L_0 = 6L_0$:

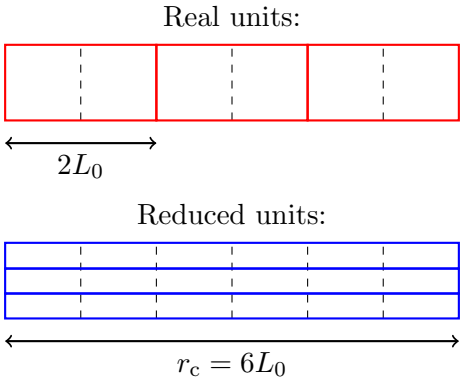

Note that the mass of one bead $m = N_{\mathrm{m}} m_0 = 2m_0$ gets smeared across a larger space, which is defined by the length scale $r_{\mathrm{c}} = 6L_0$. It then follows that to cover exactly six molecules, the reduced density must be equal to $\tilde{\rho} = 3$, which means stacking three particles (rectangles) on top of each other.

Choosing $\xi_1 \neq 1$

Imagine now that we define the bead size $r_c = \tilde{\rho}^{\xi_1} N_m L_0$. This means that we decouple the definition of r_c from N_m and $\tilde{\rho}$. We now illustrate how this approach fails.

Consider again the case $\tilde{\rho} = 2$, $N_m = 3$, and choose $\xi_1 = 2$. Hence, $r_c = \tilde{\rho}^{\xi_1} N_m L_0 = 12 L_0$. The mass of one bead should be $m = 3m_0$. We get the following scheme:

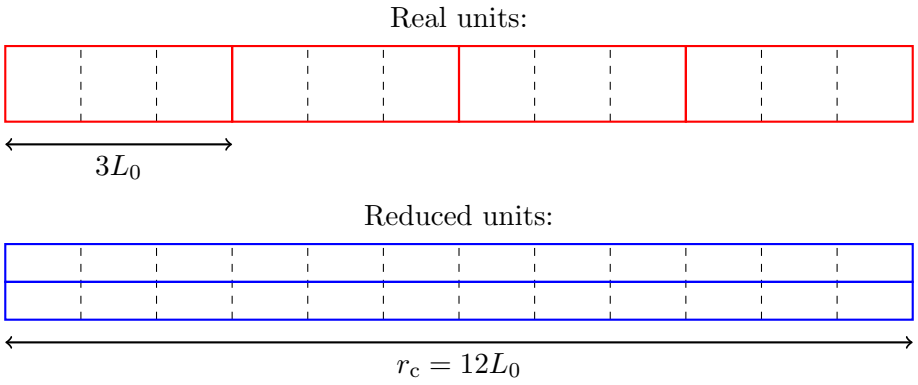

Computing the mass of one bead from the surface area yields:

$$m = \frac{1}{2}\rho_m \times 12 L_0 = 6m_0. \tag{4.40}$$

However, by choosing $N_m = 3$ we already fixed the mass at $m = 3m_0$, which is a contradiction!

Choosing $\xi_2 \neq 1$

Relaxing ξ_2 leads to a similar problem. Consider $\tilde{\rho} = 3$, $N_m = 2$ and $\xi_2 = 2$. Then, $r_c = \tilde{\rho} N_m^{\xi_2} L_0 = 12 L_0$. Drawing the same scheme as before:

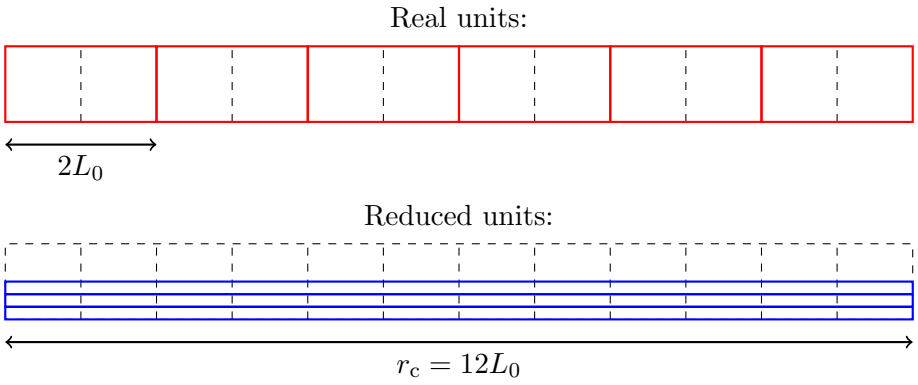

The height of one bead in reduced units is chosen such that the area corresponds to the mass in the bead $m = N_m m_0 = 3m_0$. In such case, however, there appears an empty space not covered by the beads, meaning that some mass cannot get squeezed into the beads. Again, this is a contradiction.

Trying $\xi_1 = 0$ or $\xi_2 = 0$

What if we redefined r_c such that it would not contain either $\tilde{\rho}$ or N_m? Would it allow to change the coefficient without violating the mass conservation?

Consider, for example, $r_c = N_m^{\xi_2} L_0$. Choosing $N_m = 3$ and $\xi_2 = 2$, we get $r_c = 9L_0$. To fill all the space, this would automatically decide the density $\tilde{\rho} = 3$, as demonstrated by the following scheme:

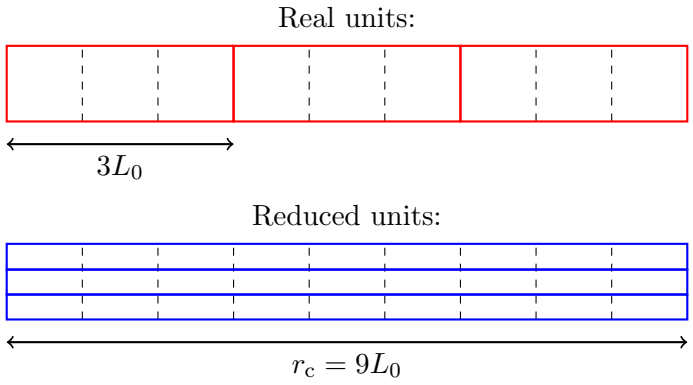

More generally, deciding N_m and ξ_2 would fix $\tilde{\rho} = N_m^{\xi_2 - 1}$. Similarly, choosing $r_c = \tilde{\rho}^{\xi_1} L_0$ would automatically fix $N_m = \tilde{\rho}^{\xi_1 - 1}$.

4.3.2 Simultaneous variation of ξ_1, ξ_2

There is a way to relax the definition of r_c and maintain mass conservation at the same time.

Starting from $r_c = \tilde{\rho}^{\xi_1} N_m^{\xi_2} L_0$, we now derive the relation between ξ_1 and ξ_2 given the necessary constraints.

The mass of one bead in real units is $m = N_m m_0$, and $m_0 = \rho_m L_0$. The law of mass conservation could be stated as follows: the mass of $\tilde{\rho}$ beads occupying one blue block, is $\tilde{\rho_m}$ (blue picture), and this is equal to $r_c \rho_m$ (red picture). Hence:

$$m = \frac{r_c \rho_m}{\tilde{\rho}} = \frac{\tilde{\rho}^{\xi_1} N_m^{\xi_2} L_0 \rho_m}{\tilde{\rho}} = \tilde{\rho}^{\xi_1 - 1} N_m^{\xi_2} m_0 = \tilde{\rho}^{\xi_1 - 1} N_m^{\xi_2 - 1} m. \tag{4.41}$$

from which it follows:

$$\tilde{\rho}^{\xi_1 - 1} = N_m^{1 - \xi_2}. \tag{4.42}$$

Using this gauge, we can choose ξ_1 independently from $\tilde{\rho}$ and N_m. This would yield ξ_2:

$$\xi_2 = 1 - (\xi_1 - 1) \frac{\ln \tilde{\rho}}{\ln N_m}. \tag{4.43}$$

Now the relationship between real and reduced bead density changes to:

$$\rho = \frac{\tilde{\rho}^{\xi_1} N_m^{\xi_2 - 1}}{r_c}, \quad \text{consistent with} \quad \rho = \frac{1}{N_m L_0} = \frac{n}{N_m}. \tag{4.44}$$

Having rectified the problem with mass conservation, we still need to devise the transfor-

mation of the equation of state, starting with the ideal gas term:

$$p = \rho k_\mathrm{B} T \quad \rightarrow \quad \tilde{p} = \tilde{\rho}\widetilde{k_\mathrm{B}T}. \tag{4.45}$$

We consider the case $N_\mathrm{m} = 1$ for simplicity. Knowing that $\tilde{p} = pr_\mathrm{c}/k_\mathrm{B}T_\mathrm{c}$ and $\widetilde{k_\mathrm{B}T} = k_\mathrm{B}T/k_\mathrm{B}T_\mathrm{c}$, we start from the real form $p = \rho k_\mathrm{B} T$:

$$p = \rho k_\mathrm{B} T, \tag{4.46}$$

$$p = \frac{\tilde{\rho}^{\xi_1}}{r_\mathrm{c}} k_\mathrm{B} T, \tag{4.47}$$

$$pr_\mathrm{c} = \tilde{\rho}\tilde{\rho}^{\xi_1 - 1} k_\mathrm{B} T, \tag{4.48}$$

$$p\frac{r_\mathrm{c}}{k_\mathrm{B}T_\mathrm{c}} = \tilde{\rho}\frac{k_\mathrm{B}T}{k_\mathrm{B}T_\mathrm{c}}\tilde{\rho}^{\xi_1 - 1}, \tag{4.49}$$

$$\tilde{p} = \tilde{\rho}\widetilde{k_\mathrm{B}T}\,\tilde{\rho}^{\xi_1 - 1}. \tag{4.50}$$

The remaining term $\tilde{\rho}^{\xi_1 - 1}$ cannot be absorbed into any definition of a reduced unit. Hence, It is impossible to transform $p = \rho k_\mathrm{B} T$ into reduced units with definition of r_c other than $\tilde{\rho} N_\mathrm{m} L_0$. We conclude that relaxing the definition of r_c is a dead end.

4.4 Conclusions

In the first part of this chapter, following the derivations by Füchslin *et al.* [30] we restated the scaling of the simulation parameters in the dissipative particle dynamics with respect to coarse-graining degree arguing by dimensional analysis only. The outcome of this procedure was the rectification of the temperature dependence of the conservative interaction parameter, which dates back to the original work of Groot and Warren [7]. Consequently, we showed that some simulation parameters, such as the friction constant γ and the Flory-Huggins χ-parameter, need to be pre-scaled in reduced units prior to the simulation in order to make the experimental observables, such as self-diffusivity or surface tension, scale-invariant. Our findings bring in the consistency and enable to compare simulations across a range of coarse-graining degrees.

Chapter 5

Bottom-up DPD parametrisation

> We wanted the best, but it ended up as always.
>
> *Viktor Chernomyrdin*

This chapter presents a protocol to generate the DPD interaction parameter a from bottom–up. Our recipe is built on an idea that the radial distribution function (RDF) of a coarse–grained but atomistically resolved liquid should be the same as the one from a mesoscale simulation. To coarse–grain atomistic simulations we use the k–means clustering algorithm, and to compare the RDFs we explore two approaches. We test our reasoning on a few liquids and demonstrate that the resulting interaction parameter gives meaningful and scale-invariant values.

5.1 Introduction

Coarse-graining in simulation reduces the computational expense while retaining vital features of the system. In some sense, even atomic nuclei, the smallest units in most sophisticated computer models, are only coarse–grained quarks. In more practical terms, in ab initio simulations core electrons are coarse–grained into a pseudopotential and only valence electrons are treated as such. In classical molecular dynamics (MD), all electrons are coarse–grained into a Lennard-Jones potential, which contains only the long-range attractive term due to van der Waals interactions, and the short-range repulsive term due to the Pauli exclusion principle. The resulting speed-up from to this effective removal of quantum effects is several orders of magnitude.

Coarse-graining of atoms into bigger particles has been an important research topic in the past few decades, motivated by the fact that even atomistically resolved simulations of large molecules, e.g. proteins, are prohibitive [98]. The theoretical origin of coarse–graining dates back to Zwanzig [99] and Mori [100]. Common approaches include potential of mean force and direct or iterative Boltzmann inversion. The resulting potentials can be static or dynamic, i.e. derived on-the-fly.

In this chapter we are concerned with dissipative particle dynamics (DPD), a mesoscale method with a static potential controlled by only one interaction parameter. This very simple and efficient method has been successfully applied to a wide range of soft-matter systems such as polymer melts, block copolymers, amphiphiles or ionomers [27].

There have been several attempts to derive DPD simulation parameters from bottom–up. Espanol showed that the dissipative and random forces in DPD arise by integrating out the degrees of freedom [101]. The MD simulations of LJ liquids by Lei *et al.*, in which groups of atoms were constrained, revealed how the potentials of mean force and radial distribution functions arise [102]. Izvekov derived a scheme to coarse–grain dissipative and random terms [97].

We aim to devise a parametrisation method from bottom–up, using atomistically resolved simulations, as opposed to top-down macroscopic route using compressibility, which has been originally presented by Groot and Warren, the authors of the method, and still remains in use [7]. The key idea behind our approach is to match scale-invariant quantities for atomistic and coarse–grained simulations. The first example is pressure, leading to the possible comparison of the equations of state. This suggests that the virial expansion should be the same in case of atomistic and DPD liquid. However, this method is valid only in the dilute regime and thus is unsuitable at reduced number densities $\rho > 1$, when the series $\sum_i B_i \rho^i$ has problems with convergence. Unfortunately, DPD operates at $\rho = 3$ and higher. Another scale-invariant quantity is the radial distribution function (RDF), which is essentially an experimental observable.[1]

Here, we explore the role of RDF as a means for inferring the DPD interaction parameter from atomistic simulations. Apart from this aim, we explore the general structure of RDFs of pure DPD liquids, which are controlled by only two input parameters: density ρ and interaction parameter a. We demonstrate that these RDFs can be fitted by simple functions combined from a sine, a Gaussian, and a sigmoid.

We note that the key algorithm that we employ for clustering molecules into beads, k–means, has also been used in a very similar context by Hadley and McCabe [103]. We found this coincidence only after defining the main contours of this project.

The organisation is as follows. In Section 5.2 we first present the MD simulations of a few simple liquids and the algorithm to cluster them into coarse–grained particles. Then, in Section 5.3 we discuss the general structure of RDFs of a pure DPD liquid. Finally, Section 5.4 introduces two methods to match the RDFs arising from clustered MD and DPD simulations, which we call first–peak and maximum–overlap.

5.1.1 Protocol to generate DPD interaction parameters

Our approach consists of the following steps:

1. Run an MD simulation of a pure liquid.

2. Compute the centres of mass of (several frames of) the equilibrated liquid.

3. Apply the k–means algorithm to cluster the molecules into coarse grained particles, a step similar to Izvekov [97] and Hadley *et al.* [103].

[1] Its Fourier transform is the structure factor, which arises from X-ray diffraction.

4. Compute the RDFs for a range of CG degrees.

5. By matching the coarse–grained RDFs from MD simulations with RDFs of pure DPD liquids, infer the DPD interaction parameter.

5.1.2 Brief overview of DPD

Dissipative particle dynamics (DPD) is thoroughly presented in the introduction of this thesis. Here we summarise only its vital features. DPD a coarse–grained method suitable for simulation of soft matter. Compared with standard coarse–grained dynamics, the interparticle potential in DPD is set from the beginning and controlled by only one interaction parameter. The potential is quadratic (using reduced units $r_\mathrm{c} = k_\mathrm{B}T_\mathrm{c} = m_\mathrm{c} = 1$):

$$V(r) = \begin{cases} \frac{a}{2}(1-r)^2, & r < 1, \\ 0, & r \geq 1, \end{cases} \tag{5.1}$$

yielding linear force. The temperature is maintained by the Langevin thermostat providing a dissipative and a random term.

The method is used with reduced units $r_\mathrm{c} = m_\mathrm{c} = k_\mathrm{B}T_\mathrm{c} = 1$.The energy scale is set from the simulation temperature T_c, and the length scale r_c from the average molecular volume V_0, the coarse–graining degree N_m and the chosen reduced density ρ, which is essentially a free parameter:

$$r_\mathrm{c} = (\rho N_\mathrm{m} V_0)^{1/3}. \tag{5.2}$$

The simplicity of this force field yields a parabolic equation of state for densities $\rho > 3$:

$$p = \rho + \alpha a \rho^2, \tag{5.3}$$

where $\alpha = 0.101$. The interaction parameter a can be derived by matching the liquid compressibility κ (in reduced units):

$$a = \frac{\kappa^{-1} - \rho}{2\alpha\rho^2}. \tag{5.4}$$

The cross interactions between different kinds of particles can be obtained via the Flory-Huggins χ-parameter: $\Delta a_{ij} = 3.27\chi_{ij}$, where i, j are different particle species.

To simulate the DPD liquid throughout this chapter we used the DL_MESO package version 2.6.

5.2 Coarse-graining molecules from atomistic simulations

Our aim is to approximate an atomistically resolved homogeneous liquid composed of molecules by DPD beads such that an average bead contains N_m molecules. On these we will consequently calculate the RDF, which we will later match with model RDFs arising from pure DPD liquids. Assuming that these RDFs are fundamentally similar, this match will enable us to derive the DPD interaction parameter.

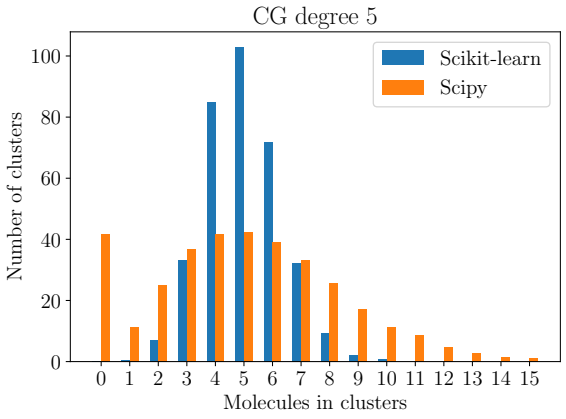

Figure 5.1: An example of the distribution of the number of molecules in clusters after running two different implementations of the k–means algorithm for the MD simulation of SPC water with 1728 molecules. An ideal distribution would contain only one peak at $N_\mathrm{m} = 5$.

To partition the molecules into groups we employ k–means clustering algorithm. The core idea is to distribute $N_\mathrm{c} = N/N_\mathrm{m}$ cluster centres and let them evolve in order to find the close molecules by moving towards the centre of mass of the nearest molecules until convergence. The closeness is defined by their distance from the cluster centre, which is the definition of the Voronoi cell. We then interpret the resulting cluster centres as coarse–grained beads. In contrast to the work by Hadley and McCabe [103], we perform this only once and do not proceed iteratively until convergence marked by agreement of the centre of cluster volume and centre of mass. We will demonstrate that even one step yields satisfactory results. Furthermore, in our approach the CG degree is a parameter that can be chosen.[2]

We define the *bead* as the centre of mass (CoM) belonging to a concrete cluster. Even though there are other options that could capture the "essence" of a bead, such as the centre of volume occupied by the molecules, the (CoM) is a simple and reliable choice. Moreover, it naturally arises as a result of the k–means algorithm.

K-means algorithm is not perfect, and it is practically impossible to obtain a homogeneous coarse–grained liquid where each cluster would have exactly N_m molecules. There will always be a distribution around N_m. For example, at $N_\mathrm{m} = 5$ there will be usually 0 to 10 molecules per cluster. The standard deviation depends on the cluster initialisation, which varies with implementation. Taking into account the simplicity and efficiency on the algorithm, as well as aiming to average over many frames, we can still consider k–means well suited for this task.[3] We also note that standard implementations of this algorithm do not consider periodic boundary conditions, a basic concept in computational physics. However, this deficiency can be considered as a finite-sized effect, the role of which diminishes with increasing the system size.

We explored two implementations contained in Scipy and Scikit-learn libraries. The Scikit-learn version produced a significantly lower spread of molecules per cluster and no clusters with zero molecules. The example of a distribution is visualised on Fig. 5.1. Despite slightly increased computational expense we consider it far more reliable than the Scipy implementation.

We tested our reasoning on the following seven liquids:

[2]We had also tried to partition the box by randomly locating the cluster centres and assigning the molecules to their Voronoi cells. This approach resulted in unphysical RDFs with non-zero values at at $r = 0$, which demonstrated the obvious fact: the coarse–grained beads are not be randomly distributed.

[3]The common problems with performance of k–means are well summarised in this blog post: http://varianceexplained.org/r/kmeans-free-lunch/

1. water in various parametrisations: SPC, TIP3P-EW and TIP4P/2005,
2. methanol,
3. ethanol,
4. acetone.

For simulation we used LAMMPS (version from 11 August 2017). We equilibrated the system in NpT for 500k steps, evolved in NpT for another 500k steps, and collected the data in NVT during 20k steps. The time step was set to 1 fs, so overall each simulation took about 1 ns. In case of water, the oxygen-hydrogen bonds and the angle were fixed by the SHAKE algorithm. To account for finite-size effects, we investigated three sets of boxes: 512, 1000, and 1728 molecules.

The interaction parameters, which include partial charges, bonds, angles and non-bonded LJ terms for water models can be found on the LAMMPS website[4] or on this website[5]. For methanol, ethanol, and acetone, we used AMBER force field parameters [104].

The resulting coarse–grained RDFs based on clustered CoMs are shown on Figs 5.2. They all possess the same features marked by a pronounced correlation hole[6] close to $r = 0$, a smooth rise towards the first peak, and a fast convergence towards 1 beyond $r = 1.5$ nm. Furthermore, beyond $N_\mathrm{m} > 2$ the RDFs show a smooth variation with N_m, marked by a linear shift in the position and the height of the first peak.

In the following, we will match the key features of these coarse–grained RDFs from MD simulations to idealised RDFs of a pure DPD liquid, with the aim to infer the appropriate interaction parameter for a real liquid at a given CG degree.

5.3 Exploring properties of RDFs of a pure DPD liquid

Having demonstrated the systematic variation of the RDFs arising from coarse–graining of MD simulations we now explore the properties of RDFs of pure DPD liquids. We show that these vary smoothly with varying the simulation parameters, which will enable us to make the connection between these systems. In this section we investigate two ways of describing an RDF: a first–peak method and a maximum–overlap method.

The static properties of a pure DPD liquid are controlled by only one two parameters: number density ρ and the only force field parameter a representing the interaction strength. In case of considering the dynamics, another parameter is the friction constant γ.

It is an interesting feature of this method that the density ρ in DPD is, from the point of view of the interpretation of results, a free parameter. Hence, it is in practise set as low as possible for the sake of computational efficiency. At $\rho > 3$ the DPD liquid is in the regime of the quadratic EOS, so $\rho = 3$ is the most suitable value. A few times $\rho = 5$ was used as well, e.g. in [11].

[4] http://lammps.sandia.gov/doc/Section_howto.html
[5] http://www.orsi.sems.qmul.ac.uk/downloads.html
[6] We borrow here the term *exchange-correlation hole* from the electronic structure theory, which describes the motion of electrons.

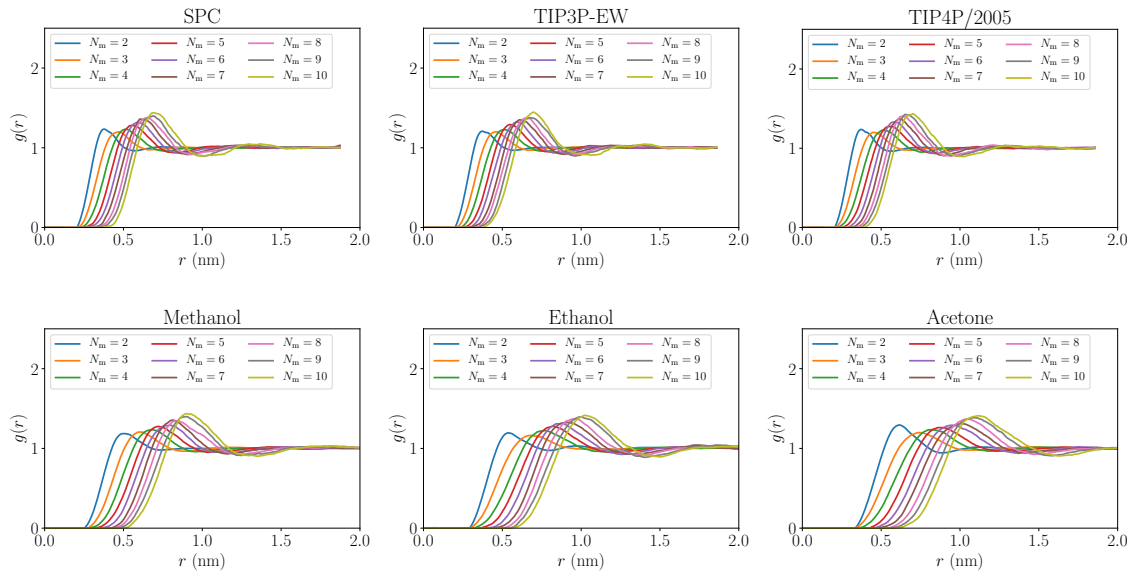

Figure 5.2: RDFs of the explored solvents for various CG degrees, showing smooth variation in first peak size for $N_m > 2$. Each simulation contained 1728 molecules.

The parameter a is typically equal to 25, the value derived from water compressibility. Beyond $a = 200$ the diffusivity drops sharply, which is a signature of freezing [95]. Having limited the range of available values, it now feasible to fully explore the parameter space.

We generated the RDFs of pure DPD liquids at densities ρ between 1 to 8 and interaction parameters from 5 to 200. The box size was set to $10 \times 10 \times 10$, so the number of beads ranged between 1000 and 8000. The friction was $\gamma = 4.5$, time step 0.05 and number of steps 100k. Figs 5.3, which show the results for $\rho = 3$ and 5, demonstrate the smooth variation of RDFs. At $\rho = 3$, the strongest signature is the rise of the first and at the same time largest peak. At $\rho = 5$, a smaller peak is formed before the largest for parameters $a > 100$, suggesting a small change in liquid ordering.

Fig. 5.3 enable us to venture that RDFs arising from a pure DPD liquid could be reduced to a few features. We first explore the height of the first and largest peak, which clearly correlates with the interaction strength a. Consequently, using a few simple functions we will try to fit the RDF as a whole.

5.3.1 Dependence of the first RDF peak on parameter a

Extracting the positions and heights of the the first peaks (FP) as a function of the interaction parameter a, we can observe that these collapse on one curve for densities $\rho = 1 - 7$. Figs. 5.4 show that the first peak positions are essentially constant for all densities and in the range $0.8 - 0.9$. More importantly, the peak heights h collapse on the power law or a line, depending on the liquid density:

$$h(a) = \begin{cases} c_1(a + c_2)^{c_3}, & \rho < 4, \\ c_1 a + c_2, & \rho \geq 4. \end{cases} \tag{5.5}$$

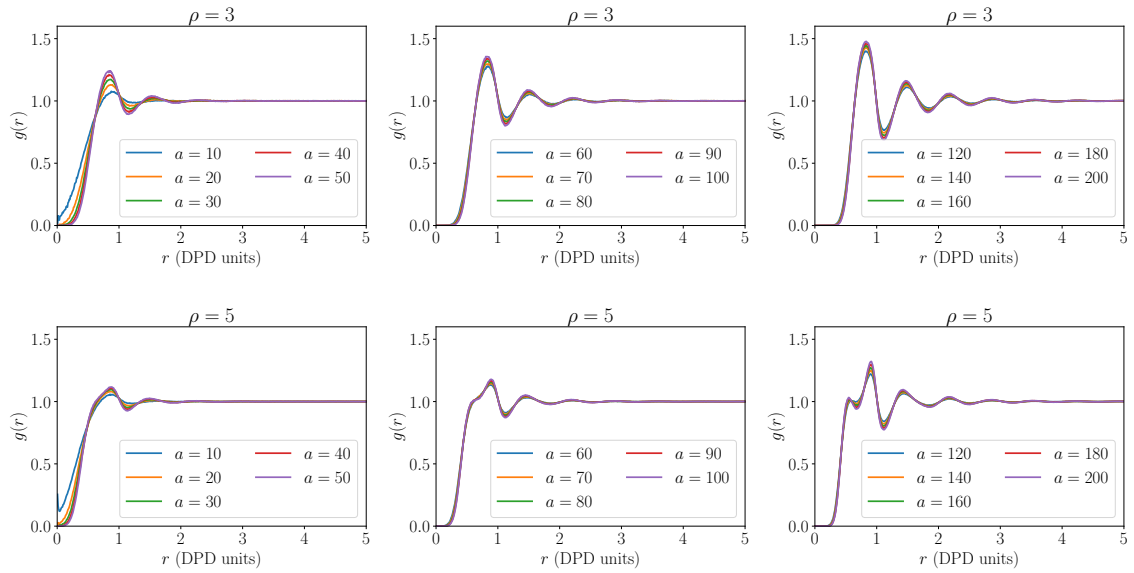

Figure 5.3: Smooth variation of the RDFs of pure DPD liquid at densities $\rho = 3$ and 5.

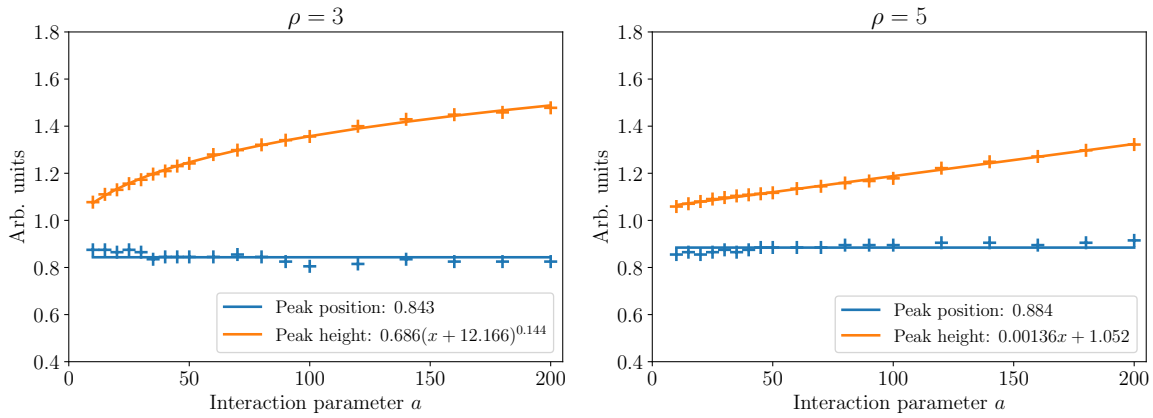

Figure 5.4: Positions and heights of first RDF peaks (FP) as a function of interaction parameter a. FP positions show little variation with a and can be treated as only density-dependent. FP heights vary linearly or as a power law with a, depending on density.

where c_i are the fitting parameters. At $\rho = 3$ the resulting dependence is.

$$h(a) = 0.928(a + 12.166)^{0.144}. \tag{5.6}$$

We will later use this form to match the RDFs arising from coarse–grained MD simulations.

5.3.2 Maximum-overlap method: fitting the whole RDF

Having revealed the relative similarity and smooth variation of the RDFs representing DPD liquid for a wide range of parameters, we can attempt to explicitly design a fitting function. A passing visual observation suggests three basis functions that should be able to capture the essential features of the RDFs above, as schematically shown on Fig. 5.5:

1. a sine for the oscillatory behaviour,

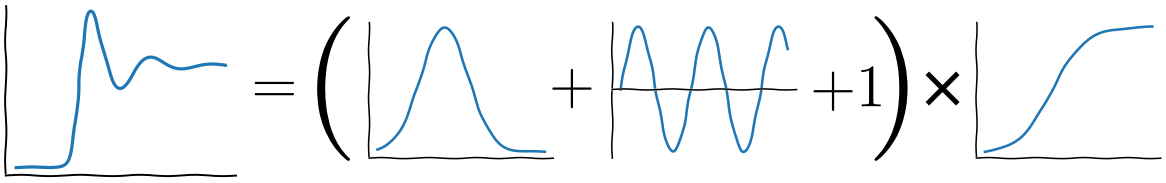

Figure 5.5: Using a combination of a sine, a Gaussian and a hyperbolic tan one in principle should be able to compose any RDF.

	N_{param}	$g(r)$
1.	5	$[d_1 e^{-\lvert x-d_2\rvert} \sin(d_3(x-d_2)) + 1][\tanh(d_4(x-d_5)) + 1]/2$
2.	6	$[d_1 e^{-\lvert x-d_2\rvert} \sin(d_3(x-d_4)) + 1][\tanh(d_5(x-d_6)) + 1]/2$
3.	5	$[d_1 e^{-(x-d_2)^2} \sin(d_3(x-d_2)) + 1][\tanh(d_4(x-d_5)) + 1]/2$
4.	6	$[d_1 e^{-(x-d_2)^2} \sin(d_3(x-d_4)) + 1][\tanh(d_5(x-d_6)) + 1]/2$
5.	6	$[d_1 e^{d_2(x-d_3)^2} \sin(d_4(x-d_3)) + 1][\tanh(d_5(x-d_6)) + 1]/2$
6.	7	$[d_1 e^{d_2(x-d_3)^2} \sin(d_4(x-d_5)) + 1][\tanh(d_6(x-d_7)) + 1]/2$

Table 5.1: Tried fitting functions for the RDFs.

2. a Gaussian or an exponential for the large first peak,

3. a hyperbolic tan, or a sigmoid, for the correlation hole close to $r = 0$.

From now on we will only focus on the most widely used DPD density $\rho = 3$, which could lead to the greatest applicability. We fit the RDFs using the combination of these three basis functions. Each of these bases requires about two parameters, overall leading to up to 10 fitting parameters. Some of these have clear interpretation in how they capture the essential features of an RDF, such as the height of the first peak, the period of the sine, or the position of the peak of the Gaussian. Others are more open to removal in the attempt to simplify the models, such as the steepness and the shift of the hyperbolic tan, the position of the sine, or the steepness of the Gaussian.

We tried several plausible combinations, presented in Table 5.1, of increasing complexity measured by the number of the parameters, We tried to reduce the parameters where possible, e.g. by controlling the Gaussian/exponential peak and a sine peak by only one parameter. For each of the explored functions we measured the correlation, defined as

$$C(x, y) = \frac{\sum_i (x_i - \bar{x})(y_i - \bar{y})}{\sum_i (x_i - \bar{x})^2 \sum_i (y_i - \bar{y})^2}, \tag{5.7}$$

where x_i, y_i are the vectors of the simulated and fitted RDFs, respectively. Only correlations above 0.99 led to a visibly satisfactory overlap of the predicted and training curves. The 7-parameter fit no. 5 turned out as the most reliable as well as sufficient. This is no surprise, as generally more parameters lead to a better fit.

Having found the set of parameters $\{d_i\}$ for on a set of RDFs arising from pure DPD liquid, we now determine their dependence of each d_i on the interaction parameter a. Expecting smooth

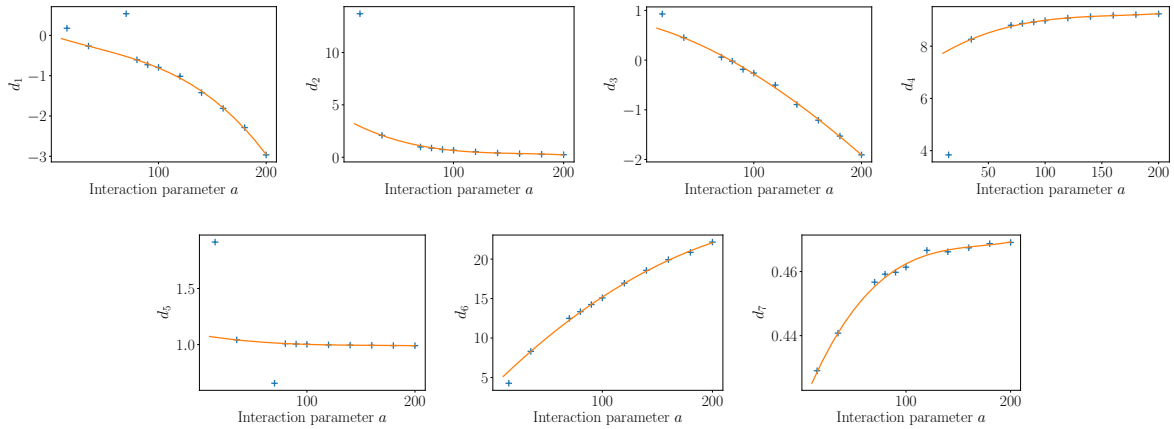

Figure 5.6: Dependence of fitting parameters d_i on the interaction parameter a.

variation, we assume that these can be captured by a polynomial of a certain order. It turns out that 3rd order polynomial (with four parameters each) provides a satisfactory fit:

$$d_i(a) = c_{3,i}a^3 + c_{2,i}a^2 + c_{1,i}a + c_{0,i}, \quad i \in \{1, ..., 7\}, \tag{5.8}$$

The variation of d_i with a is shown on Fig. 5.6.

Thus predicted RDFs really lie on the curve with sufficient accuracy, as shown on Figs. 5.7. The only deviations occur at both extremely low and high interactions. At $a = 10$ the correlation hole at $r \leq 1$ is not well pronounced, and at $a = 180$ or 200 the height of the first peak is slightly overshot. Further investigation showed that the latter imperfection can be smoothed with a 4th order polynomial fit of d_i's. Since in practise such high interactions are unlikely, we decided to stick with the 3rd order polynomial.

Finally, we briefly discuss if the number of fitting parameters $N_\mathrm{p} = 28$ is not too high. Considering the amount of data that went into the fitting (20 RDFs, 500 point per RDF, overall around 1000 points), N_p is reasonably low. There might be small room for improvement, since d_5 is almost constant and could be set to 1, which would reduce N_p to 24. Similarly, it might be possible to fit the other d_i's with a lower-order polynomial, but it is questionable if the time spent on this tuning would be worth the effort.

An advanced challenge would be to exploit one of numerous machine learning approaches to devise an implicit fit of any RDF. This line of research might lead to a genuinely useful solution, not only in the context of the parameter generation for the DPD. However, this would be far from trivial, especially without the intuition provided by the basis functions, which would be more difficult to incorporate, and is beyond the scope of this work.

5.4 Deriving DPD interaction parameters by matching RDFs

Having coarse–grained the MD simulations by clustering molecules using k–means algorithm and understood the trends in the RDFs generated by the DPD, we now in a position to predict the DPD interaction parameters bottom–up for a few pure liquids.

Starting from the assumption that RDFs should be independent of the simulation method,

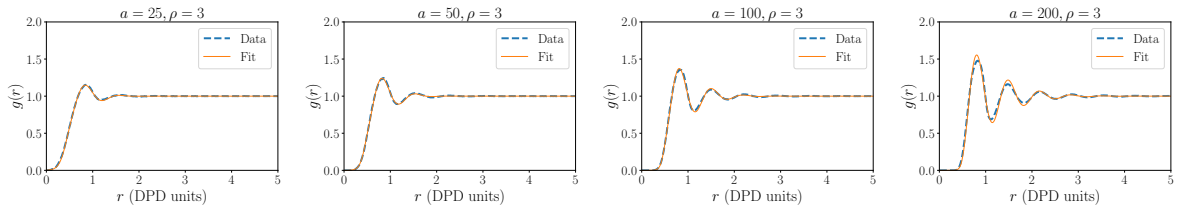

Figure 5.7: A few examples of predicted RDFs as a function of a using 28 parameters using sine, exponential and hyperbolic tangent. The agreement is excellent for $a < 180$

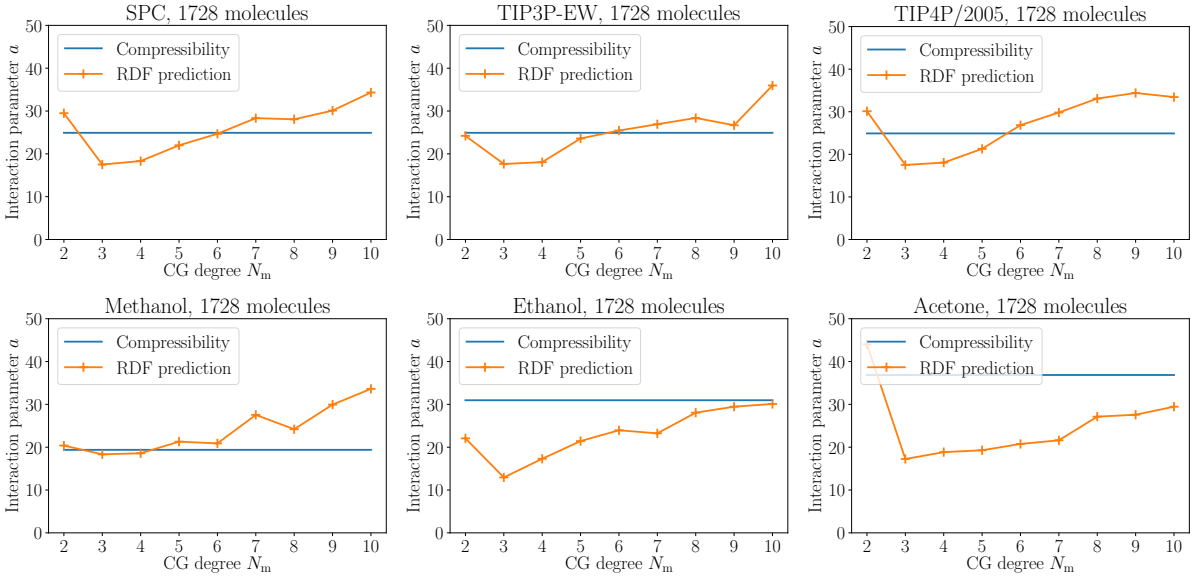

Figure 5.8: Predicted interaction parameters for several solvents via first–peak (FP) method CG degrees N_m for 1728 molecules.

we present two approaches to generate the interaction parameter for the DPD: the simple first–peak method, and the more sophisticated maximum–overlap method. The advantages of both methods are conceptual simplicity, the easiness in visualising the process, and no need to iterate.

Before presenting the results, we need to clarify an important technical point. In reduced units, the DPD interaction parameter for a specific liquid remains constant across all the scales, as was first shown by Füchslin [30].[7] For example, water in DPD has $a = 25$ regardless of the CG degree. In real units, $a \sim N_m^{2/3}$. Since the MD simulations are done in real units, we need to divide the derived interaction parameter by this scaling factor.

5.4.1 First–peak method

Figs. 5.8 show the interaction parameters predicted by reversing eq. (5.6).and compare them with the compressibility route proposed by Groot and Warren [7].

Visual inspection shows that nearly all derived values are within a factor of two from the compressibility line. Furthermore, excluding the pathological behaviour CG degree $N_m = 2$, all the FP-derived parameters reveal an unexpected steady increase with N_m. For the water models, the FP and compressibility curve cross each other and hence agree well at intermediate

[7] We prove this in Chapter 4.

CG degrees $N_\mathrm{m} = 5-8$. Apart from water, methanol seems to agree well up to $N_\mathrm{m} = 8$, whereas ethanol converges towards the compressibility only at $N_\mathrm{m} \geq 8$. Acetone deviates most strongly.

In conclusion, the increase of FP–derived interaction parameters with CG degree is unsatisfactory. This deficiency provides motivation for the exploration of a more sophisticated method.

5.4.2 Maximum–overlap method

We apply the tools built in chapter 5.3.2 to generate the interaction parameters for the real liquids. We consider only the DPD liquids with density $\rho = 3$. At this density, the whole RDF is controlled by only one parameter, and the problem is reduced to finding the interaction parameter for which the overlap with the given RDF of the coarse–grained MD simulation is minimised.

We define the cost function as a continuous version of the square error:

$$J(a) = \int_0^{\mathrm{cut}} (g_\mathrm{MD}(r, N_\mathrm{m}) - g_\mathrm{fit}(r, a))^2 dr, \tag{5.9}$$

where $g_\mathrm{MD}(r, N_\mathrm{m})$ is the clustered MD RDF and $g_\mathrm{fit}(r, a)$ the idealised RDF of a pure DPD liquid. The cutoff is effectively about 20 Å, at which point both RDFs are about equal to 1. We used the Nelder-Mead optimisation algorithm from the Scipy library to minimize J for each CG degree.

Figs 5.9 show the resulting interaction parameters. Not considering $N_\mathrm{m} = 2$, which deviate strongly in all the explored cases, we observe excellent good agreement for all water models. Methanol is satisfactory, while ethanol and acetone tend to deviate by a factor of up to 2. It is especially encouraging that the correct scaling is reproduced, which is marked by the fact that the derived interaction parameters are, for all cases and up to small deviations, broadly invariant to the CG degree, especially compared with the FP method. However, we can observe a small tendency of acetone to decrease a with the CG degree. Without further investigation, it is difficult to conclude if this is a genuine trend or a finite size effect (at $N_\mathrm{m} = 10$ and with 1728 molecules, there were only 173 clusters to compute the RDF).

Furthermore, the deviation of ethanol and acetone from the compressibility route does not necessarily mean that these parameters are less suitable. One interpretation of this feature might be that derivation based on compressibility fails sufficiently capture the essence of certain molecules. That compressibility might be overly restrictive in DPD parametrisation has also recently been discussed by Anderson *et al.* [105].

5.5 Temperature dependence of interaction parameters

Having developed two methods, first–peak and maximum–overlap, to extract interaction parameters from bottom up via comparison of atomistic and coarse–grained RDFs, we now apply these to derive how the coarse–grained interaction parameters depend on temperature.

In Chapter 4 we showed that the DPD parameter a derived from compressibility varies with

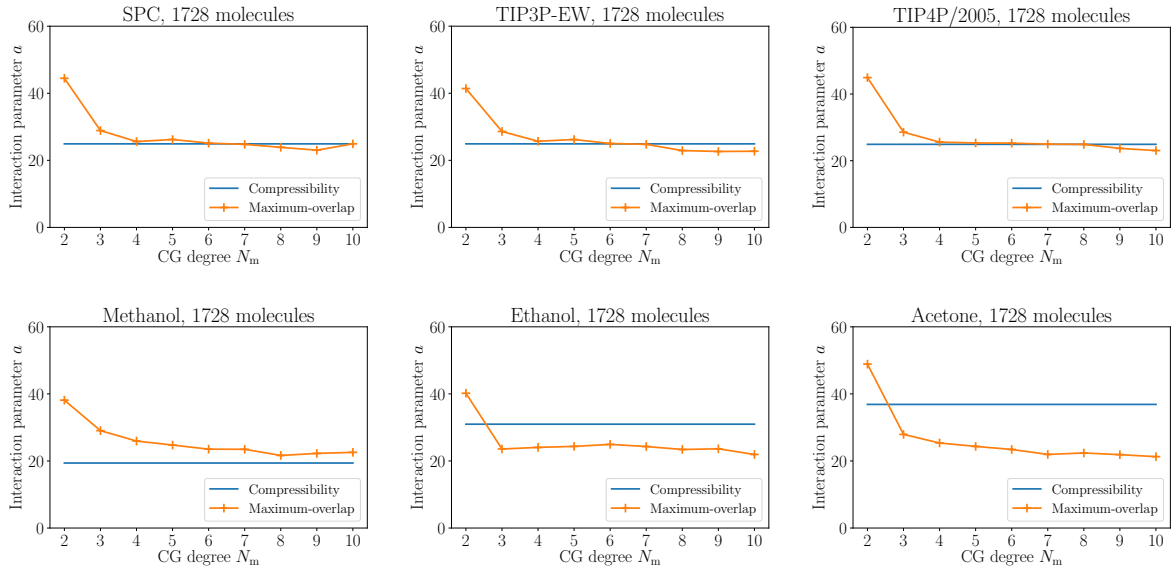

Figure 5.9: Predicted interaction parameters for several solvents via maximum–overlap (MO) method. The resulting parameters agree more closely with the compressibility derivation and preserve the scaling.

temperature k_BT (expressed in reduced units) as follows:

$$a = \frac{\kappa^{-1} - k_BT}{2\alpha\rho}. \tag{5.10}$$

Setting the energy scale k_BT_c to, e.g., 300 K, $k_BT = 1.2$ at 360 K. For water with $a(300\text{ K}) = 25$, the new interaction parameter would be $a(360\text{ K}) = 24.66$. The decrease in the value of a with temperature is in contrast to the original work on DPD [7] claiming that $a(T) = ak_BT$, i.e. $a(360\text{ K}) = 30$. In this section, we demonstrate that the bottom–up parametrisation protocol reproduces the top-down derivation from Chapter 4 based on scaling arguments only and the assumption of temperature–independent compressibility.

We consider two water models, SPCE and TIP4P-2005 at three CG degrees, $N_m = 3, 5$ and 8. As in previous MD simulations, we set up a simulation cell $10 \times 10 \times 10$ of 1000 molecules in LAMMPS. Using time step to 1 fs, we equilibrate in NpT for 500k steps and in NVT for another 500k steps, collecting data over subsequent 20k steps. For analysis we repeat the procedure outlined in previous sections, i.e. computing the centre of mass of molecules, coarse–graining them via k–means clustering, computing the RDFs at various CG degrees and extracting the interaction parameter. We explored temperatures ranging from 280 K to 360 K.

Fig. 5.10 shows the resulting variation of a with temperature using both FP and MO methods of parameter extraction. While the FP method yields a rather noisy behaviour for SPCE water model and large, systematic variation with CG degree, the temperature variation follows the expected trend of slight decrease. The MO method yields a solid agreement with both expected temperature dependence and compressibility, with precision increasing in line with CG degree. Hence, our bottom–up parametrisation method is suitable not only at room temperature, but remains robust with respect to a wider range of simulation inputs.

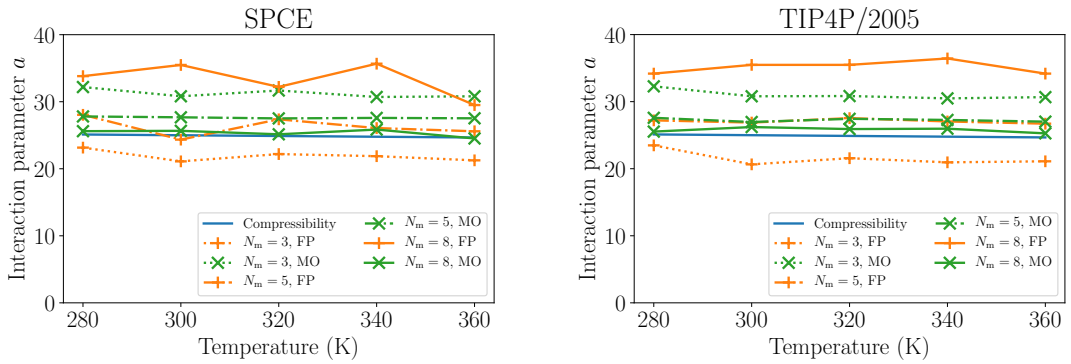

Figure 5.10: Dependence of the interaction parameter a on temperature for two water models, SPCE (left) and TIP4P-2005 (right), at a range of CG degrees N_m and using two methods of parameter extraction from coarse–grained RDF, FP and MO.

5.6 Conclusions

The original aim of the work summarised in this chapter was to develop a method to generate the DPD interaction parameters from bottom–up. This approach should, in theory, capture the microscopic essence of a liquid. We started by the notion that RDFs as essentially experimental observables[8] should be invariant with respect to a simulation method.

However, mesoscale simulations occur at different coarse–graining degrees, and hence, as a first step, it is vital to devise a method to compare RDFs across different scales. To this end, we employed the k–means algorithm to group atomistically resolved molecules into clusters. Thus generated clusters yielded RDFs that could be compared with RDFs arising from mesoscale simulation methods such as, but not exclusively, DPD.

We presented two tools to extract DPD interaction parameters by comparing RDFs. The first, *first–peak method* (FP), was based on matching the first or largest RDF peak of a clustered MD liquid with an idealised DPD liquid. The second, *maximum–overlap method* (MO), was based on fitting the RDF of a pure DPD liquid with a few simple basis functions predicting the whole RDF as a function of the interaction parameter only, and consequently finding a which maximised the overlap with clustered RDFs arising from atomistic simulations.

The interaction parameters generated by the FP method are rather imperfect in that they do not follow the basic condition on the scaling of the interaction parameter, and also show considerable noise. The MO method is significantly more reliable, providing excellent scaling and also matching the results of water perfectly at CG degrees $N_m > 2$.

We also briefly explored the idea of generalising this bottom–up parametrisation method to liquid mixtures, as these are at the heart of the interest of coarse–grained or mesoscale simulations. A reasonable aim would be the derivation of the Flory-Huggins χ-parameter, a key driver of the phase behaviour. Unfortunately, (de)mixing is by its very nature concerned with inhomogeneity and anisotropy in liquids, and these in principle cannot be captured by RDF that is isotropic in its nature. Hence, our method remains valid for pure mixtures only, which are, in the context of mesoscale simulations, of limited interest.

[8] Strictly speaking, it is the Fourier transforms of RDFs which are experimentally observable.

Another drawback is non-negligible computational expense. Compared with the straightforward compressibility route introduced by Groot and Warren [7], our method requires prior atomistic simulations, which take the order of hours on computers with about ten cores. In light of the limited scope of application caused by the inability to generalise to mixtures and more complex systems, this extra expense is hard to justify.

Notwithstanding these concerns about usefulness, this work is a playful exercise in fitting functions and trying to extract as much information from RDFs as possible. Since RDFs are important experimental observables, this exploration might later reveal avenues for further research into classification and possibly inference of material properties from experimental data.

Chapter 6

Exploration of many-body DPD

> Education is an admirable thing, but ... nothing that is worth knowing can be taught.
>
> *Oscar Wilde*

In this chapter we present a thorough exploration of the phase diagram of many-body dissipative particle dynamics (MDPD) force field. Having identified the liquid phase, we then devise a bottom-up parametrisation method based on compressibility and surface tension, and generate interaction parameters of water at a range of coarse-graining degrees. Finally, we derive the relationship between the χ-parameter and surface tension, and verify on three simple mixtures that our parametrisation gives meaningful surface tension predictions for a wide range of coarse-graining degrees.

6.1 Introduction

In designing a new force field it is vital to understand its phase diagram before applying it to real systems. It is generally prohibitively expensive to derive the equation of state (EOS), from which all the experimental observables would follow, from a molecular dynamics force field, due to many parameters that can be varied. However, the EOS can be inferred for some mesoscale potentials, which possess few parameters. This is the case for dissipative particle dynamics (DPD), for which the EOS can be easily reverse-engineered, as first Groot and Warren [7] showed for standard DPD, and consequently Warren [37] for many-body DPD (MDPD):

$$p = \rho + \alpha A \rho^2 + 2\alpha B r_{\mathrm{d}}^4 (\rho^3 - c\rho^2 + d), \tag{6.1}$$

where $\alpha = 0.1$, $c = 4.16$, and $d = 18$ are fitting constants.

The standard DPD, which is presented in the introductory chapter, has an important draw-

back in that its purely repulsive force field:

$$F(r) = \begin{cases} A(1-r), & r < 1, \\ 0, & r \geq 1 \end{cases} \tag{6.2}$$

with r being distance between two particles and parameter $A > 0$, cannot support liquid-vapour coexistence. In order to overcome this deficiency and retain the simplicity and other advantages of the extremely soft potential, there have been several attempts to generalise DPD and increase its scope of applicability. A simple extension called many-body DPD (MDPD) adds a density-dependent repulsive term [35, 36, 37]

$$F_{\text{rep}}(r) = \begin{cases} B(\bar{\rho}_i + \bar{\rho}_j)(1 - r/r_{\text{d}}), & r < r_{\text{d}}, \\ 0, & r \geq r_{\text{d}}, \end{cases} \tag{6.3}$$

where B, which is greater than zero, is the repulsion parameter, $r_{\text{d}} < 1$ a new, many-body lengthscale, and $\bar{\rho}_i$ a local density for ith particle, which we define later. For some specific set of parameters, this force field can simulate a water slab with correct surface tension [41].

Since its introduction, MDPD has been linked to Flory-Huggins theory [38, 42] and tested on several simplified models of pure liquids [42, 106] or polymers [43, 10]. However, the scope of its applications is still limited, when compared with standard DPD, and so far this method has not been applied to more complex systems of industrial relevance with the aim of behaviour prediction or material design.

The first restriction on the applicability of MDPD is the lack of a systematic protocol for generating the interaction parameters that would reproduce the properties of real liquids. For example, Ghoufi *et al.* [41] simulated pure water at a coarse-graining (CG) degree of three molecules per bead, and showed that their set of parameters leads to the correct density and surface tension. However, these authors did not explain how they generated these parameters, or how these should be modified if one wanted to simulate water at a different CG degree. As these authors admitted in a different publication [42], there is not "rigorous route" to calculate realistic MDPD interaction parameters.

Secondly, while the behaviour of standard DPD, which is controlled by only one interaction parameter, A, is relatively well understood, MDPD has three: A, B and r_{d}. The two additional parameters significantly increase the complexity of the phase diagram and the risk of unexpected and unphysical behaviour if not chosen well.

The aim of this chapter is to resolve these two problems. To this end, we explore a large portion of the phase diagram of an MDPD fluid by systematically varying the values of repulsion B, attraction A and many-body cutoff r_{d}. By measuring the density and the self-diffusion coefficient, we reveal the region of the liquid-vapour coexistence as well as the gas phase, where the particles homogeneously fill the whole simulation cell, and a solid phase with a well-defined lattice and negligible particle diffusion, but lacking a proper stress-strain relation. Having determined the phase boundaries, we then discuss how these findings can be applied to define a top-down parametrisation protocol. Finally, we demonstrate how this protocol can yield the interaction parameters for water at varying CG degrees.

We note that there is an extension generalising both DPD and MDPD called smoothed DPD (SDPD). This method corrects for the problems with transport and an inability to simulate non-isothermal settings based on discretising Navier-Stokes equations [107, 108]. However, the simplicity and versatility of MDPD makes the effort of parametrising it a worthwhile pursuit before considering a more general SDPD.

This chapter is organised as follows. In Section 6.2 we present the simulation details and tools used for determining the phase behaviour, namely the density profile, self-diffusivity, surface tension and coordination number, and determine the lattice type of the solid phase. In Section 6.3 we develop a top-down parametrisation protocol for the liquid phase and derive interaction parameters for water. Consequently, in Section 6.4 we investigate the relation between the Flory-Huggins χ-parameter and the surface tension, and predict interfacial surface tensions of a few simple binary mixtures using the formalism built in Section 6.3.

6.2 Measurement of properties

6.2.1 Simulation details

Following Ghoufi *et al.* [41], we set a simulation cell size of $22 \times 5 \times 5$ (in reduced units), with one dimension significantly larger than the others. This asymmetry forces the liquid to form a rectangular slab instead of a spherical droplet, which facilitates calculation of the surface tension. The simulation step Δt is set to 0.01, which is significantly lower than the one used in standard DPD simulations (0.05). The MDPD force field is not strictly linear and so one should expect the need to lower the simulation step in order to keep the temperature within manageable limits. On several occasions, especially at lower values of r_d, the temperature in our simulations diverged by more than 10%, which is considered undesirable [37]. While this problem can be generally ameliorated by further lowering the timestep, this creates a penalty in the form of decreased simulation speed and undermines the main advantage of DPD and MDPD as a mesoscale method. For this reason, we did not use timesteps below 0.01 and did not explore many-body cutoffs below $r_\mathrm{d} = 0.55$.

In each simulation we used 1000 particles, equilibrated for 500k steps and measured during the following 5k steps, a long enough interval to capture mass transport since a bead with average speed would be displaced by 50 length units. The dissipation parameter γ was set to 4.5, a value commonly used in the literature. We note that varying γ would change the diffusive behaviour, but it would not influence the position of phase boundaries or equilibrium behaviour in general. To perform the simulations we used the DL_MESO software package version 2.6 [84].

We have explored a wide range of values A and B. We also note that A should always be negative in order to create van der Waals loop [37] and the liquid-vapour interface, whereas values of B should always be positive to keep the core of the force field repulsive. We chose the range $[-100, 0]$ for A and $[0, 100]$ for B and henceforth refer to them as attraction and repulsion, respectively. In Section 6.3, we will show that a real liquid can fall into this range for a wide number of CG degrees.

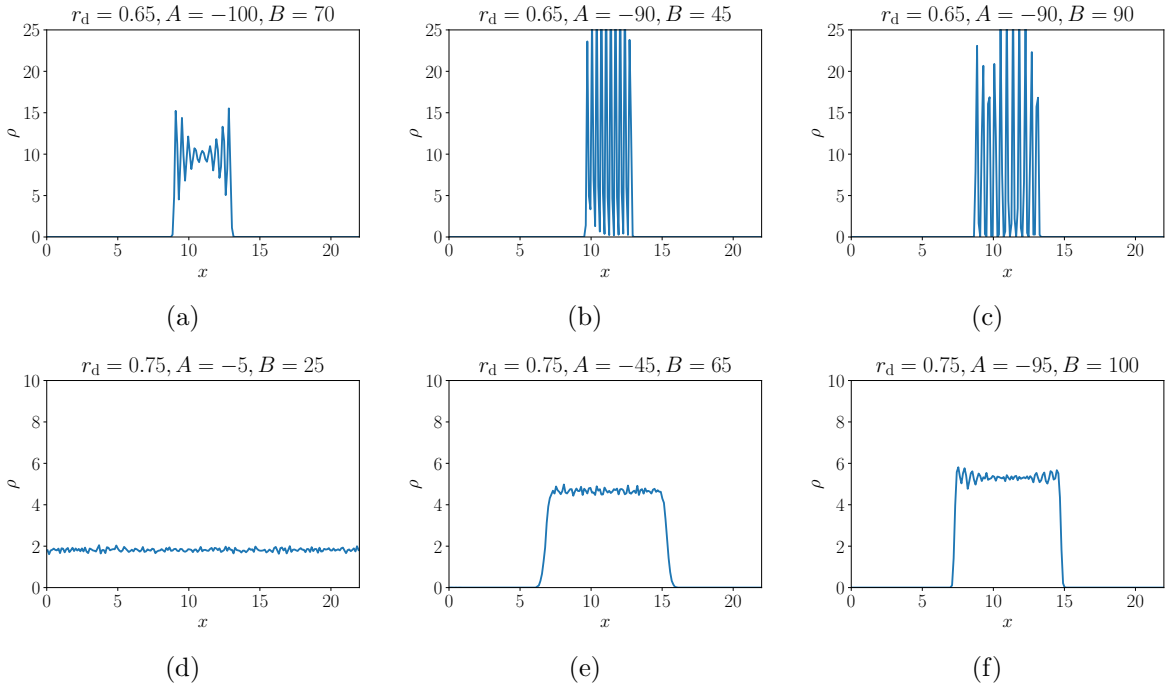

Figure 6.1: Representative density profiles of MDPD depicting solid phases with clear lattice at $r_d = 0.65$ ((a), (b), (c)), and gas, liquid and solid phase at $r_d = 0.75$ ((d), (e), (f) respectively). From the similarity of (e) and (f) it is clear that the solid phase cannot by reliably identified only by its density profile.

6.2.2 Density

Our first tool in describing the properties of MDPD fluid is density, which arises naturally as a function of the repulsion, attraction and the many-body cutoff r_d and not due to the constraints of the simulation cell as in case of standard DPD. Fig. 6.1 shows typical density profiles in a cell of size $22 \times 5 \times 5$ for $r_d = 0.75$ and 0.65. For low values of both $|A|$ and B, we observed homogeneously dispersed particles signalling the gas phase. For intermediate values between 0 and 100 there is a liquid phase with well-defined interface. Finally, the periodic variation of zero and very high density at $r_d = 0.65$ indicates a lattice of a solid phase.

To quantify these observations we fitted the density profiles with a symmetrised hyperbolic tangent:

$$\rho_{A,B}(x) = c_1[\tanh(c_2|x - c_3| + c_4) + 1]/2 + c_5. \tag{6.4}$$

where c_1 is the excess density of the liquid phase, c_5 is the density of the gas phase, c_3 and c_4 are the centre and the half-width of the liquid droplet respectively, and c_2 is the steepness of the interface. The resulting liquid density is then $\rho = c_1 + c_5$.

Fig. 6.2 shows heat maps of the computed densities $\rho = c_1 + c_5$, with each subfigure representing a specific many-body cutoff. At $r_d = 0.85$, the gas phase (dark colour) occupies almost one half of the phase diagram, indicating that at higher values of r_d there would be no space for the liquid phase within a reasonable range of repulsions and attractions. On the other hand, at low values of r_d, such as 0.55, the gas phase is limited to very low values of $|A|$, and most of the region is occupied by the solid phase, as will be confirmed by self-diffusivity measurements in Section 6.2.3.

r_d	d_1	d_2	d_3
0.65	5.01±0.03	2.11±0.05	−0.870±0.01
0.75	3.01±0.03	1.21±0.03	−0.856±0.01
0.85	1.50±0.05	0.60±0.02	−0.756±0.01

Table 6.1: Fitting coefficients for liquid and solid densites (eq. (6.5)) as a function of A, B, and r_d.

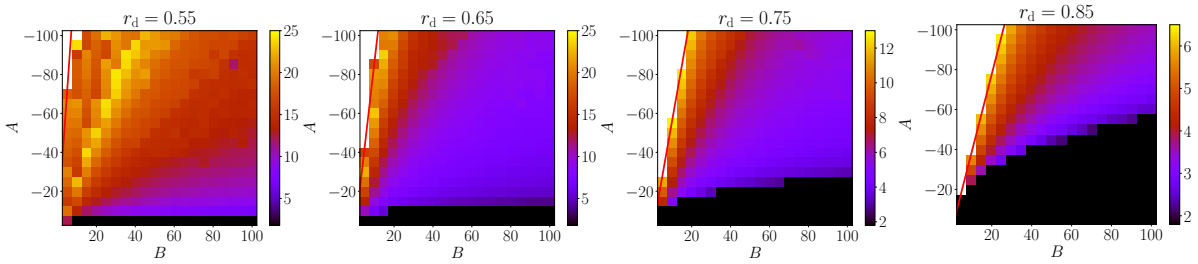

Figure 6.2: Density heat maps for $r_\mathrm{d} \in \{0.55, 0.65, 0.75, 0.85\}$. Dark regions at low values of $|A|$ show the gas phase, and yellow regions of high density show at the top left corner reveal the no-go region with attractive force at zero interparticle distance.

We now determine how the liquid or solid density vary with the force field parameters. For simplicity, we perform this fitting separately for each value of r_d. In principle it is possible to obtain such dependence by analytically finding the roots of the EOS at zero pressure. However, our attempt to solve Warren's EOS (eq. (6.1)) analytically resulted in an expression that was too long and intractable for further use. Our aim is instead to produce a density function which is more empirical but at the same time more practical for subsequent applications. This can be achieved using only a few fitting parameters and simple polynomial, power law or exponential functions.

Visually observing the cuts through the phase diagram and exploring several candidate functions we arrived at a simple three-parameter fit suitable for all considered many-body cutoffs:

$$\rho(A, B) = d_1 + d_2(-A)B^{d_3} \tag{6.5}$$

with fitting coefficients $d_i, i \in \{1, 2, 3\}$. Their values and associated errors are shown in Table 6.1. We did not fit the lowest explored value of the cutoff $r_\mathrm{d} = 0.55$ due to its very small liquid phase, but in principle this can be done as well as for any other cutoff. A more detailed analysis, including the model selection, is provided in the appendix.

6.2.3 Self-diffusivity

To reliably identify the boundary between solid and liquid phase for $r_\mathrm{d} \in \{0.65, 0, 75, 0.85\}$, we investigate the dynamic properties of MDPD. The self-diffusivity of an unknown material is an important signature differentiating between liquid, solid and gas phases. We expect this quantity to be negligible in solids, while in pure liquids or gases it should follow the Einstein regime marked by the linear dependence of the mean-square displacement on time.

We measured the self-diffusion coefficient for every configuration via the mean-square dis-

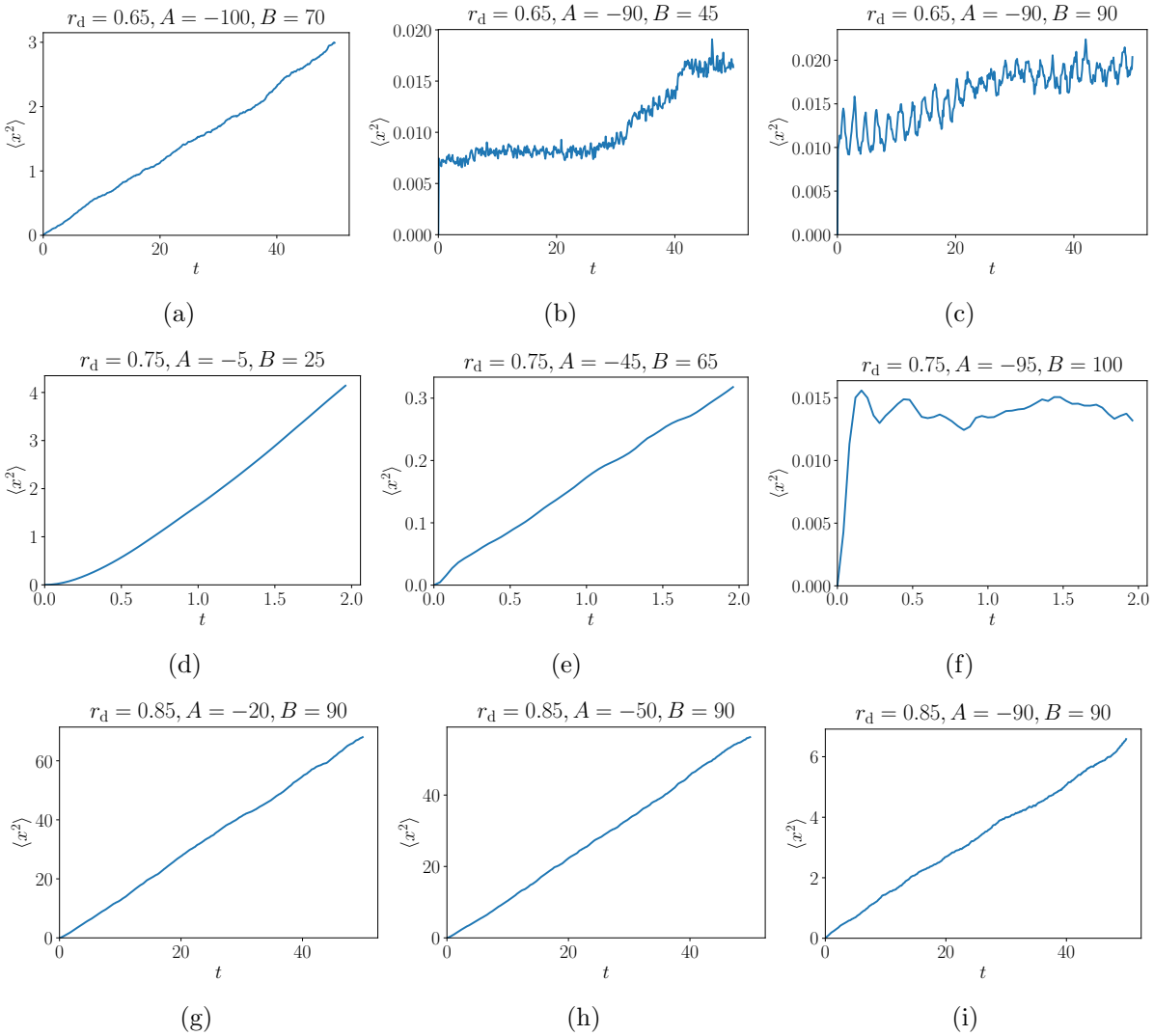

Figure 6.3: Mean-square displacements for the representative configurations observed in the many-body DPD, depicting typical behaviour of gas ((d), (g), (h)), liquid ((a), (e), (i)) and solid phase ((b), (c), (f)).

placement (MSD):

$$D = \lim_{t \to \infty} \frac{\langle |\mathbf{r}(t) - \mathbf{r}(0)|^2 \rangle}{6t} \tag{6.6}$$

where the average $\langle . \rangle$ is over all the particles.

Typical MSDs are shown on Figs 6.3. The scale on the y-axis demonstrates a clear difference between solids, liquids and gases. The solid phase poses a limit to the beads in how far they can diffuse. The liquid phase allows only the linear regime, whereas the gas phase contains a polynomial transient response and then gradually becomes linear.

Plotting all the self-diffusivities in a heat map (Figs 6.4) enables us to distinguish the different phases. Dark blue regions corroborate the existence of the solid phase, whereas the yellow regions show the gas phase. The region in between is liquid.

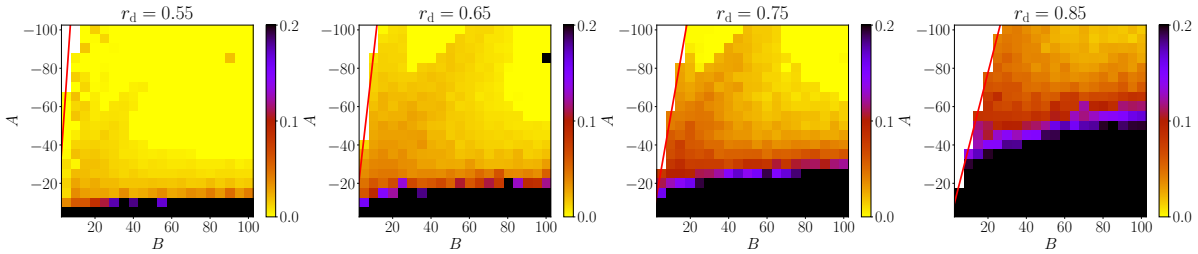

Figure 6.4: Self-diffusivity heat maps for $r_d \in \{0.55, 0.65, 0.75, 0.85\}$. Yellow regions at the top reveal the solid phase; dark regions regions at the bottom show the gas phase.

6.2.4 Lattice of the solid phase

Having located the whereabouts of the solid phase in the phase diagram via the self-diffusion coefficient, we now determine its lattice. There are in fact two lattice types, implying two different phases. Starting with $r_d = 0.75$, we observe the first type occurring at large values of both repulsion and attraction, around $(A, B) = (-100, 100)$. The density of this configuration is $\rho \approx 5$. Another phase, which is formed at high repulsions $A < -80$ and intermediate attractions $B = 30$–50, is more closely packed, with a typical density of $\rho \approx 8$ at $r_d = 0.75$.

To identify these phases, we plotted the radial distribution functions (RDF) and compared them with a set of RDFs of several Bravais lattices smeared by temperature fluctuations. The first phase was identified with the body-centred cubic (bcc) lattice (Fig. 6.7), and the second one with the hexagonal (hex) lattice with an interlayer distance lower than the in-plane lattice constant.

As another verification, we computed the coordination numbers (CN) for all the solid configurations (A, B, r_d), which we chose by their self-diffusivity. CN is defined as the number of nearest neighbours of a particle, which can be computed by integrating the RDF $g(r)$:

$$z(r) = \rho \int_0^r g(r')\, 4\pi r'^2\, dr'. \tag{6.7}$$

In a lattice, neighbouring particles reside in so-called coordination shells, which give rise to local maxima in the RDF. Separating the adjoining coordination shells can be realised by identifying the plateaus in the CN as a function of the distance, i.e. the minima in the first derivative of $z(r)$. Fig. 6.5 unambiguously shows that all the solid configurations (A, B, r_d) indeed fall into two groups: the bcc phase with a plateau value of $z \approx 14$, which includes first two coordination shells, and the hex phase with a first plateau $z = 2$, which captures out-of-plane vertically aligned atoms, followed by $z \approx 20$, which comprises two hexagons above and below and one in the plane of any particle.

From Fig. 6.5 it is also clear that the solid phase occupies a major part of the phase diagram at $r_d = 0.55$, rendering the usefulness of this value of this many-body cutoff rather limited for simulations of liquids. On the opposite end, at $r_d = 0.85$, the solid phase is non-existent within the explored range of repulsions and attractions. From these observations it follows that most practical for simulation of multiphase systems, as well as richest in terms of the number of phenomena to capture, are simulations at $r_d = 0.75$, which has already been widely employed in the literature, as well as 0.65.

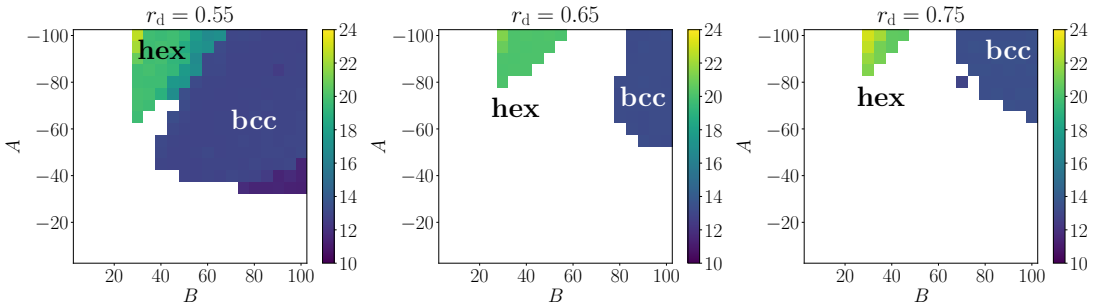

Figure 6.5: Heat map of coordination numbers for each many-body cutoff r_d containing a solid phase, with the lattice denoting a specific phase type.

We further investigated the stability of both phases, performing simulations in multiple orthorhombic simulation cells of varying degree of asymmetry, between $16 \times 4 \times 4$ up to the cubic shape, $16 \times 16 \times 16$, and for a range of densities. For the bcc phase, we took the configurations $(A, B, r_d) = (-100, 100, 0.75)$, at which the equilibrium density was $\rho_{bcc} \approx 5.5$. When setting the initial density to around 5.5, the randomly initialised particles indeed formed a bcc lattice for every cell box shape, implying a stable minimum.

To reproduce the hex phase, we chose the configuration $(-100, 40, 0.75)$ leading to the equilibrium density $\rho_{hex} = 8.5$. Starting again from randomly initialised positions, the hex phase formed only when the initial density was set below ρ_{hex}, and only in the more asymmetric cells. This suggests that the hex phase is stabilised by the negative pressure.

Further investigation by measuring excess chemical potential via the Widom particle insertion method [3] revealed that the bcc phase is significantly more stable than the hex phase at both $(A, B, r_d) = (-100, 100, 0.75)$ and $(-100, 40, 0.75)$. We can hence safely conclude that the hex phase is metastable and cannot be considered as a true bulk phase of the MDPD force field.

Finally, to estimate the stress-strain relation of the solid phase, we put an already solid cuboid into a larger simulation cell. After a short simulation period, its shape became spherical. Hence, the true stress-strain relationship of the solid phase cannot be captured by MDPD.[1]

6.2.5 Liquid phase and surface tension

We now return to the examination of the liquid phase by excluding solid and gas regions. We computed the surface tension for each configuration as follows:

$$\sigma = \frac{L_x}{2}\left(\langle p_{xx}\rangle - \frac{\langle p_{yy}\rangle + \langle p_{zz}\rangle}{2}\right), \tag{6.8}$$

where $p_{\beta\beta}$ are the diagonal components of the pressure tensor. As in case of density, we obtain the functional dependence of the surface tension by fitting over the measured points for each many-body cutoff r_d. Visual observation of the cuts through the phase diagram at constant A or B and trial of several functions revealed that different many-body cutoffs r_d are best fit by different functions with varying number of parameters. Table 6.2 summarises these functions and

[1] We thank an unknown reviewer for inspiring this analysis.

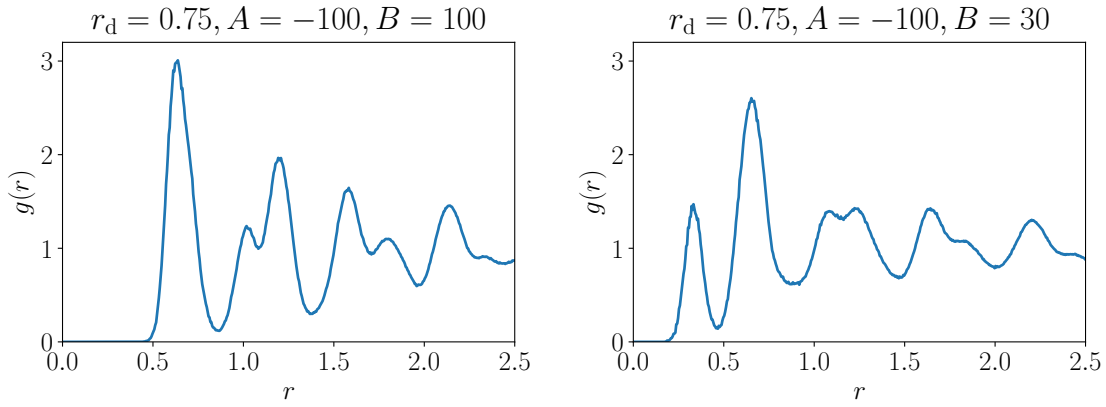

(a) (b)

Figure 6.6: Radial distribution functions of (a) bcc and (b) hex phase for $r_d = 0.75$. The lattices of the simulation were identified by comparing these with RDFs arising from ideal temperature-smeared lattices.

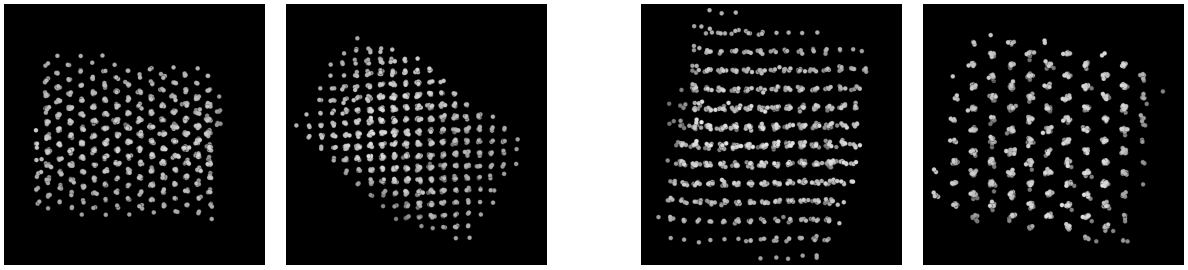

(a) (b)

Figure 6.7: Lattice visualisations from various high-symmetry directions of (a) bcc and (b) hex phases for $r_d = 0.75$.

their coefficients. We explain the reasoning for the model selection more fully in the appendix.

6.3 The connection to real liquids

Having described the phase diagram of an MDPD fluid and determined the dependence of density and surface tension on the force field parameters A, B, and r_d, we now discuss how these findings can be used in parametrising real liquids. In the standard DPD, the simulation of a pure fluid is controlled by one parameter $A > 0$, and hence only one physical quantity is needed to bridge the simulation with the experiment. Groot and Warren chose compressibility [7], but

r_d	Function	Coefficients
0.65	$(f_1A^2 + f_2A + f_3)(B - f_4 + f_5A)^{f_6}$	$(0.0592, -4.77, -66.8, -1.62, 0.146, -0.665)$
0.75	$(f_1A^2 + f_2A)(B + f_3A)^{f_4}$	$(0.0807, 0.526, 0.0659, -0.849)$
0.85	$(f_1A^2 + f_2A)(B - f_3)^{f_4}$	$(0.0218, 0.591, 7.52, -0.803)$

Table 6.2: Fitting functions and their coefficients for the surface tension dependence on A and B.

in principle many other experimental properties could be used.

In developing the parametrisation for MDPD, we first assume that r_d is fixed. There remain two free parameters, repulsion and attraction, and so two physical quantities are needed. Having obtained functional relations for density and surface tension over a wide range of configurations (A, B, r_d), we now understand how the behaviour of the liquid, gas or solid varies with the interparticle potential. Furthermore, compressibility is readily available as a function of density and (A, B, r_d) from the EOS due to Jamali *et al.* [38] (eq. (1.25)):

$$\kappa^{-1} = \rho\frac{\partial p}{\partial \rho} = \rho + 2\alpha A\rho^2 + 2\alpha B r_\mathrm{d}^4(3\rho^3 - 2c'\rho^2 + d'\rho) - \frac{\alpha B r_\mathrm{d}^4}{|A|^{1/2}}2\rho^2, \tag{6.9}$$

where $k_\mathrm{B}T$ was set to 1 and c', d' are fitting constants.

Starting from the interaction parameters in reduced units, we can verify that the relations for density, surface tension, and compressibility yield meaningful liquid properties. As an example, let us take $(A, B, r_\mathrm{d}) = (-40,\ 25,\ 0.75)$, which were first used by Warren to demonstrate the capabilities of MDPD by forming a pendant drop [37], and later by Ghoufi and Malfeyt to prove that MDPD is capable of simulating liquid water [41]. Using the values from Table 6.1 we obtain the density 6.09, which is almost equal to the simulation value 6.08 (also obtained by Arienti [109]). Employing the appropriate equation and coefficients from Table 6.2, the surface tension is 7.01 in reduced units.

To convert these numbers into experimental values, we need to define the reduced units. Following Groot and Rabone's definition of the units in standard DPD simulations [83], these depend on the simulated liquid and are based on the average volume per molecule V_0, the number of molecules in a bead (a CG degree) N_m, and the target density ρ:

$$r_\mathrm{c} = (\rho N_\mathrm{m} V_0)^{1/3}. \tag{6.10}$$

Having determined ρ from $(A,\ B,\ r_\mathrm{d})$ and taking $N_\mathrm{m} = 3$, the length scale r_c is 0.818 nm. The experimental observables are summarised in Table 6.3. The density in SI units is trivially 997 $\mathrm{kg/m^{-3}}$, as this is the value on which the parametrisation was based in the form of the volume per molecule V_0.

To convert the compressibility and surface tension to SI values, we first need understand how these quantities scale with the CG degree. Following Füchslin [30] and the work in Chapter 4, we note:

$$k_\mathrm{B}T \sim N_\mathrm{m}, \tag{6.11}$$

$$r_\mathrm{c} \sim N_\mathrm{m}^{1/3}, \tag{6.12}$$

$$\kappa^{-1,\mathrm{real}} = \kappa^{-1} k_\mathrm{B}T_\mathrm{c}/r_\mathrm{c}^3 \sim 1, \tag{6.13}$$

$$\sigma^\mathrm{real} = \sigma k_\mathrm{B}T_\mathrm{c}/r_\mathrm{c}^2 \sim N_\mathrm{m}^{1/3}. \tag{6.14}$$

The resulting bulk modulus, which is the inverse of the compressibility, is about three times the experimental value (2.15×10^9 Pa) and the surface tension is about twice as high as the real value for water (71.5 mN/m). Compared with more precise, atomistically resolved water models such as SPC, which yield about 50 mN/m [110], this is not an unreasonable agreement, so we

$N_\mathrm{m} = 3$	Reduced units	Real units
Length scale r_c	1	0.818 nm
Density	6.09	997 kg/m^3
Surface tension	7.01	130 mN/m
Bulk modulus	294	6.67×10^9 Pa

Table 6.3: Predicted physical properties of a typical MDPD liquid with configuration $(A,\, B,\, r_\mathrm{d}) = (-40,\, 25,\, 0.75)$. These can be compared with experimental values 2.15×10^9 Pa and 71.5 mN/m for bulk modulus and surface tension, respectively.

can say that these interaction parameters yield meaningful, if not accurate quantities of interest. However, we now show that there is space for fine-tuning, which would achieve considerably improved precision.

6.3.1 Parameterisation for real liquids

Usually, in simulating new materials, one desires to go the opposite way, that is start from experimental data and obtain the interaction parameters in reduced units to prepare the material for simulation. Here, we show how this can be achieved. From this point we denote the quantities in reduced units by a diacritical tilde.

For any liquid defined by compressibility, surface tension and volume per molecule, and choosing CG degree N_m and temperature defining the energy scale $k_\mathrm{B}T_\mathrm{c}$, we have four highly non-linear equations with four unknowns: $r_\mathrm{c}, \tilde{A}, \tilde{B}$, and $\tilde{\rho}$. Considering, e.g., $\tilde{r}_\mathrm{d} = 0.75$, the fitting coefficients from Tables 6.1 and 6.2 yield:

$$r_\mathrm{c} = (\tilde{\rho} N_\mathrm{m} V_0)^{1/3}, \tag{6.15}$$

$$\tilde{\rho}(\tilde{A}, \tilde{B}) = 3.01 + 1.21(-\tilde{A})\tilde{B}^{-0.856}, \tag{6.16}$$

$$\tilde{\sigma}(\tilde{A}, \tilde{B}) = \sigma \frac{r_\mathrm{c}^2}{k_\mathrm{B}T_\mathrm{c}} = (0.0807\tilde{A}^2 + 0.526\tilde{A})(\tilde{B} + 0.0659\tilde{A})^{-0.849}, \tag{6.17}$$

$$\tilde{\kappa}^{-1} = \kappa^{-1}\frac{k_\mathrm{B}T_\mathrm{c}}{r_\mathrm{c}^3} = \tilde{\rho}\frac{\partial \tilde{p}}{\partial \tilde{\rho}} = \tilde{\rho} + 2\tilde{\alpha}\tilde{A}\tilde{\rho}^2 + 2\tilde{\alpha}\tilde{B}\tilde{r}_\mathrm{d}^4(3\tilde{\rho}^3 - 2c'\tilde{\rho}^2 + d'\rho) - \frac{\tilde{\alpha}\tilde{B}\tilde{r}_\mathrm{d}^4}{|\tilde{A}|^{1/2}}2\tilde{\rho}^2. \tag{6.18}$$

These equations can be solved numerically, either by a root-finding algorithm[2] or by a brute-force search through the parameter space.

In a mesoscale simulation, one does not demand extreme accuracy, so rounding the interaction parameters to nearest integer can often suffice. Hence, working with resolution $\Delta\tilde{A} = 0.1$, $\Delta\tilde{B} = 0.1$, a brute-force search through the parameter space with range $[-100, 0]$ and $[0, 100]$ for $\tilde{A}$ and $\tilde{B}$, respectively, requires relatively few evaluations of eqs. (6.18) and an objective error term. On an average modern computer, this process takes at most a few seconds.

We defined the error function as follows:

$$\mathrm{Err} = w\left|1 - \frac{\sigma}{\sigma_\mathrm{L}}\right| + \left|1 - \frac{\kappa^{-1}}{\kappa_\mathrm{L}^{-1}}\right|, \tag{6.19}$$

[2] One can now employ, e.g., the `find_root` function from the Scipy library

Table 6.4: Derived interaction parameters for water at various CG degrees and $\tilde{r}_\mathrm{d} = 0.65$.

N_m	$\tilde{\rho}$	$\tilde{A}$	$\tilde{B}$	σ (mN/m)	κ^{-1} (10^9 Pa)
1	22.10	−14.8	2.0	71.1	3.52
2	21.52	−14.3	2.0	71.1	3.37
3	20.61	−14.1	2.1	71.8	3.33
4	21.06	−13.9	2.0	71.8	3.24
5	20.28	−13.8	2.1	71.3	3.23
6	20.83	−13.7	2.0	72.2	3.18
7	20.71	−13.6	2.0	70.8	3.15
8	19.46	−13.6	2.2	71.5	3.20
9	20.60	−13.5	2.0	71.4	3.12
10	19.36	−13.5	2.2	71.4	3.17

where σ_L and κ_L^{-1} are experimental surface tension and compressibility, respectively. We chose the weight factor $w = 5$, putting more emphasis on reproducing surface tension more accurately than compressibility, which in itself is too restrictive, as has been recently highlighted in the context of standard DPD [105].

We have determined the interaction parameters $\tilde{A}, \tilde{B}$ for water, which we later apply to water-solvent mixtures. We need to bear in mind that water is an outlier in that its surface tension is about three times higher and the volume per molecule several times lower than in case of other common solvents. We have explored a range of many-body cutoffs $\tilde{r}_\mathrm{d}$: 0.65, 0.75 and 0.85 and CG degrees N_m from 1 to 10.

Firstly, we focus on water. The resulting values of $\tilde{A}, \tilde{B}$ for $\tilde{r}_\mathrm{d} = 0.65$, which are shown in Table 6.4, are relatively small and marked by excessive inverse compressibilities. More importantly, the reduced density, which is a key parameter for simulation efficiency, is extremely high for any CG degree up to 10, as can be compared by the typical density $\tilde{\rho} = 3$ used in standard DPD. We conclude that this many-body cutoff is useless for water simulations and decide not to proceed.

The parameter search for $\tilde{r}_\mathrm{d} = 0.75$ yields more suitable results, with accurate surface tensions as well as compressibilities for all CG degrees, as shown in Table 6.5. The density $\tilde{\rho}$ is still rather high at $N_\mathrm{m} = 1$ and 2, but other CG degrees are viable. $\tilde{r}_\mathrm{d} = 0.85$ in Table 6.6 produces reasonable parameter values and highly suitable reduced densities, almost on the level of standard DPD, but slightly low inverse compressibilities. Hence, both of these values of $\tilde{r}_\mathrm{d}$ are suitable for simulations including water. This analysis also suggests that an intermediate value of $\tilde{r}_\mathrm{d}$, such as 0.80, would provide both reasonable densities as well as accurate compressibilities.

To demonstrate the robustness of this parametrisation method, Table 6.7 shows derived interaction parameters for ethanol and benzene, respectively, as examples of chemically different solvents. These two liquids have several times lower surface tension (22.3 mN/m for ethanol and 28 mN/m for benzene) and compressibility than water, which leads to lower and thus more

N_m	$\tilde{\rho}$	$\tilde{A}$	$\tilde{B}$	σ (mN/m)	κ^{-1} (10^9 Pa)
1	9.99	−18.5	3.9	71.6	2.23
2	8.63	−18.1	4.9	71.5	2.16
3	7.76	−18.2	6.0	71.5	2.19
4	7.23	−18.2	6.9	71.3	2.22
5	6.94	−18.0	7.4	71.4	2.20
6	6.70	−17.9	7.9	71.6	2.20
7	6.55	−17.7	8.2	71.5	2.18
8	6.39	−17.6	8.6	71.4	2.18
9	6.23	−17.6	9.1	71.5	2.20
10	6.12	−17.5	9.4	71.5	2.20

Table 6.5: Derived interaction parameters for water at various CG degrees and $\tilde{r}_\mathrm{d} = 0.75$.

N_m	$\tilde{\rho}$	$\tilde{A}$	$\tilde{B}$	σ (mN/m)	κ^{-1} (10^9 Pa)
1	5.71	−39.8	10.0	71.3	1.20
2	5.43	−39.9	11.0	71.6	1.16
3	5.24	−39.6	11.6	71.5	1.10
4	5.07	−40.0	12.5	71.4	1.09
5	4.95	−40.0	13.1	71.4	1.06
6	4.88	−39.6	13.3	71.5	1.01
7	4.80	−39.4	13.6	71.4	0.98
8	4.68	−40.0	14.6	71.6	0.99
9	4.60	−40.0	15.1	71.3	0.96
10	4.54	−40.0	15.5	71.5	0.94

Table 6.6: Derived interaction parameters for water at various CG degrees and $\tilde{r}_\mathrm{d} = 0.85$.

efficient simulation densities.

Having discussed the properties of pure liquids, we now turn our attention to mixtures.

6.4 Mixing in MDPD

Having provided a general liquid parametrisation protocol for MDPD and derived the interaction parameters and densities of coarse-grained water, we now turn to the mixing properties of liquids. In simulating binary mixtures, we keep the parameter $\tilde{B}$ constant across liquid species, as required by the no-go theorem derived by Warren [111]. Thus, only varying $\Delta\tilde{A}$ controls the phase separation.

In the context of standard DPD, mixing was related to the Flory-Huggins theory [7]. In order to bridge the experiments to mesoscale simulation, the Flory-Huggins χ-parameter, which

Table 6.7: Derived interaction parameters for ethanol at $\tilde{r}_d = 0.75$ for a range of CG degrees.

Ethanol					
N_m	ρ	A	B	σ^{real} (mN/m)	$\kappa^{-1,real}$ (10^9 Pa)
1	6.63	−20.9	9.7	22.3	0.84
2	5.86	−20.3	12.4	22.3	0.84
3	5.49	−19.9	14.2	22.3	0.85
4	5.31	−19.5	15.2	22.3	0.84
5	5.16	−19.2	16.1	22.3	0.84

Table 6.8: Derived interaction parameters for benzene at $\tilde{r}_d = 0.75$ for a range of CG degrees.

Benzene					
N_m	ρ	A	B	σ^{real} (mN/m)	$\kappa^{-1,real}$ (10^9 Pa)
1	6.17	−33.3	19.6	28.0	1.05
2	5.48	−32.3	25.2	28.0	1.05
3	5.18	−31.4	28.3	28.0	1.05
4	5.00	−30.8	30.7	28.0	1.05
5	4.87	−30.3	32.6	28.0	1.05

can be computed a priori for a given mixture from Hildebrand solubilities δ via eq. (4.26) or through a more sophisticated Monte Carlo sampling [34], was related to the excess repulsion $\Delta\tilde{A}$.

Denoting $\chi = \nu\Delta\tilde{A}$, $\nu = 0.286$ in standard DPD at $\tilde{\rho} = 3$ and 0.689 at $\tilde{\rho} = 5$ [7]. In the context of MDPD, Jamali *et al.* derived three values of ν at three different densities, considering positive values of $\tilde{A}$ only and hence describing a purely repulsive liquid (eqs. (19)–(21) in their paper) [38]. Since density in MDPD is not decided a priori but arises by choosing the liquid and the specific CG degree, we need to understand the general dependence of ν on density. These three points obtained by Jamali *et al.* can be fitted by a line:

$$\nu(\tilde{\rho}) = -0.259 + 0.196\tilde{\rho}. \tag{6.20}$$

Here, we derive how ν depends not only on density but also many-body cutoff $\tilde{r}_d$ for negative values of $\tilde{A}$. Following the protocol presented by GW (Section V and Fig. 7), we set up a simulation cell $20 \times 8 \times 8$, varied excess repulsion $\Delta\tilde{A}$ between 0 and 15 and measured the χ-parameter from the phase-separated density profiles via:

$$\chi = \frac{\ln[(1-\tilde{\rho}_A)/\tilde{\rho}_A]}{1-2\tilde{\rho}_A}, \tag{6.21}$$

where $\tilde{\rho}_A$ is the density of component A (for illustration, see Fig. 6 in GW). Consequently, we fitted this dependence of χ on $\Delta\tilde{A}$ by a line. Fig. 6.9 shows that that the region of linear dependence is limited for the values of χ between about 2 and 6 and depending on the density,

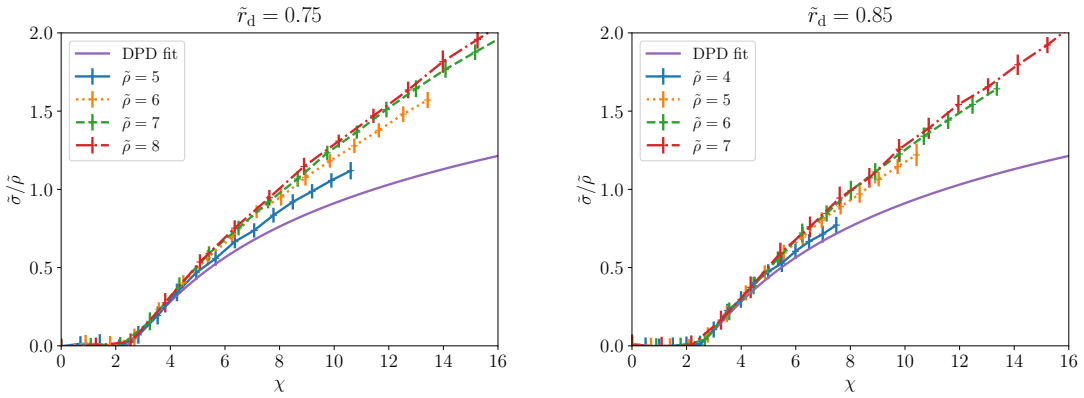

(a) (b)

Figure 6.8: Dependence of density-scaled surface tension $\tilde{\sigma}/\tilde{\rho}$ on the χ-parameter for (a) $\tilde{r}_d = 0.75$ and (b) $\tilde{r}_d = 0.85$ with error bars.

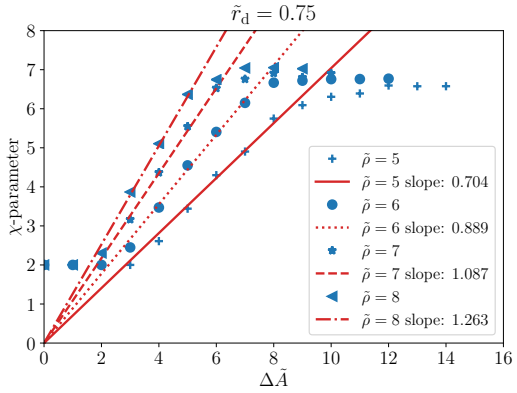

Figure 6.9: Dependence of the Flory-Huggins χ-parameter on excess repulsion $\Delta\tilde{A}$ for a range of densities. Compare this with Fig. 6 from GW [7] and especially Fig. 10 from Jamali *et al.* [38].

which should be carefully taken into consideration in simulating binary mixtures.

Exploring four different densities, we obtained a linear dependence of ν on density similar to Jamali *et al.*:

$$\nu = -(0.233 \pm 0.019) + (0.188 \pm 0.003)\tilde{\rho}, \tag{6.22}$$

for $\tilde{r}_d = 0.75$, and

$$\nu = -(0.285 \pm 0.019) + (0.196 \pm 0.003)\tilde{\rho}, \tag{6.23}$$

for $\tilde{r}_d = 0.85$. The influence of $\tilde{r}_d$ on ν is small and for practical purposes can be neglected.

6.4.1 Surface tension

Having determined the dependence of the χ-parameter on excess repulsion $\Delta\tilde{A}$, we now turn our attention to surface tension, a key quantitative descriptor of behaviour of a binary mixture.

Firstly, we verify how surface tension varies on χ-parameter. We note that Jamali *et al.* have also computed this dependence (Fig. 12b in [38]) but did not provide a functional form. We decided to revisit their results due to a different choice of interaction parameters $\tilde{A} > 0$ by these authors. We used the pressure tensor components for surface tension calculation via eq. (4.30).

Fig. 6.8a and 6.8b show the surface tension vs χ-parameter for $\tilde{r}_d = 0.75$ and 0.85, respec-

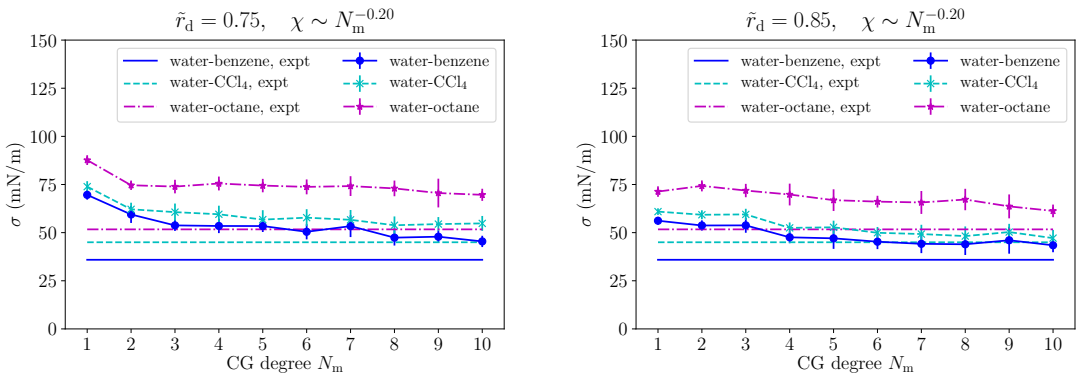

(a) (b)

Figure 6.10: Surface tension predicted from a MDPD simulation and compared with experiment for three solvent mixtures for (a) $\tilde{r}_d = 0.75$ and (b) $\tilde{r}_d = 0.85$. The scaling of the χ-parameter with CG degree aims to keep real surface tensions scale-invariant.

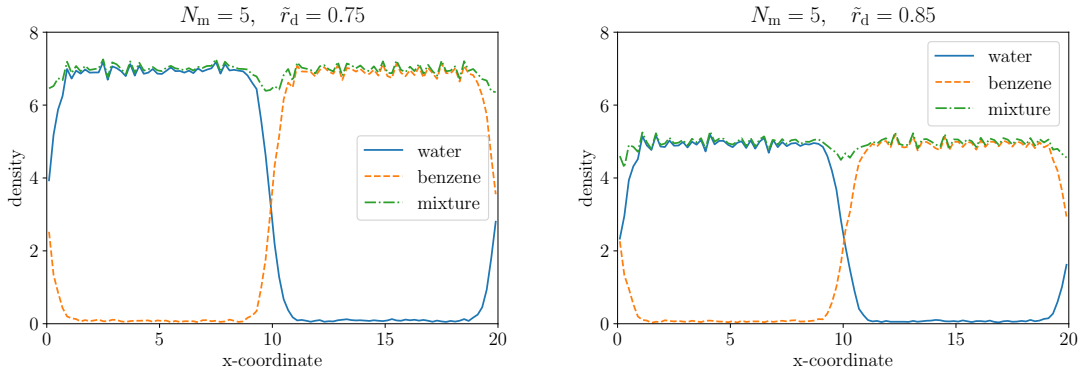

(a) (b)

Figure 6.11: Density profiles of equilibrated many-body DPD mixture of water and benzene at CG degree $N_m = 5$ for many-body cutoffs (a) $\tilde{r}_d = 0.75$ and (b) $\tilde{r}_d = 0.85$.

tively. We do not observe the collapse of the ratio $\tilde{\sigma}/\tilde{\rho}$ onto one curve, as GW claimed, beyond $\chi > 5$, as there still remains a small density dependence. Furthermore, our absolute values of the surface tension are lower by about a factor of three from the values obtained by Jamali *et al.* (Fig.12b), but in agreement with Fig. 1b from Yong [43].

GW suggested a fitting form $\tilde{\sigma} = \mu_i \chi^{\mu_2}(1 - \mu_3/\chi)^{3/2}$. In order to find a universal scaling where all the surface tension curves collapse onto one, we relaxed this form via coefficient ξ:

$$\tilde{\sigma}/\tilde{\rho}^{\xi} = \mu_i \chi^{\mu_2}(1 - \mu_3/\chi)^{3/2}. \tag{6.24}$$

Searching for ξ that minimises the standard deviation on μ_i, which is a signature of universal scaling, we found that the best fit is provided by $\xi = 1.38$ for $\tilde{r}_d = 0.75$ and 1.24 for $\tilde{r}_d = 0.85$.

As in the case of standard DPD, in order to enable reliable simulations of real mixtures at various scales, we need to derive the scaling of the χ-parameter with CG degree in order to keep surface tension in real units scale-invariant. Fitting for μ_i in eq. (6.24) and computing surface tension for the three mixtures considered by Maiti *et al.* [93], namely: water-benzene, water-

CCl_4 and water-octane, at CG degrees 1-10, we found that $\chi \sim N_m^{-0.2}$ yields the smallest RMSE with respect to experimental values in Table 4.1, an exponent similar to -0.22 for standard DPD.

To verify the predictive ability of MDPD, we computed via simulation surface tensions of the three mixtures for a range of CG degrees and the two viable many-body cutoffs, 0.75 and 0.85. We remark that the χ-parameters computed by eq. (4.26) of these mixtures are all on the top end of the range of validity in Fig. 6.9 at low CG degrees. We setting the simulation cell $20 \times 10 \times 10$ and timestep $\Delta\tilde{t} = 0.02$, we simulated in DL_MESO version 2.6 for 150k steps, using first 50k for equilibration and collecting 10k pressure tensor components for averaging. The interaction parameters $\tilde{B}_{ij}$ were the same for all pairs of species due to the Warren's no-go theorem, and $\tilde{A}_{ij}$ were different only for unlike species:

$$\tilde{A}_{ij} = \tilde{A} + \nu(\tilde{\rho})\chi_{ij}, \tag{6.25}$$

$$\tilde{B}_{ij} = \tilde{B}, \tag{6.26}$$

where $\tilde{A}, \tilde{B}$ were taken from Tables 6.5 or 6.6 for appropriate CG degree.

For $\tilde{r}_d = 0.75$, the results on Fig. 6.10a show a satisfactory albeit not perfect agreement apart from $N_m = 1$ and 2. At these low CG degrees, the densities are very high and already out of the range of validity of the density fit, resulting in incorrect liquid behaviour. Increasing many-body cutoff to $\tilde{r}_d = 0.85$, Fig. 6.10b shows good agreement of up to 10% in case of water-CCl_4. Considering that due to lower density $\tilde{\rho}$ the simulations took about a third of the time required by the configurations employing $\tilde{r}_d = 0.75$, this setting is suitable for water-solvent simulations. Illustrative density profiles of water and benzene at $N_m = 5$ are provided on Fig. 6.11.

Finally, we note that treating water and other solvents with the same set of default interaction parameters (A_{ii}, B_{ii}) is sufficient if the simulation cell is filled with liquid phase only, as is the case of our current simulations. However, to simulate liquid-vapour coexistence it would be ideal if the two solvents had their own set of default parameters derived from their respective compressibilities and surface tensions. At present, this is a challenge for MDPD due to the no-go theorem[111] preventing different values of B_{ij}.

6.5 Conclusion

In this chapter we have demonstrated the richness of many-body dissipative particle dynamics and established its suitability for simulating a wide range of mesoscale systems. By systematic variation of the force field parameters we uncovered the regions of liquid, gas and solid phase. We identified one stable solid phase with the bcc lattice, and one metastable phase with hexagonal lattice.

For the liquid phase, we fitted the density and surface tension as a function of the force field parameters and demonstrated how these functional relations can serve to generate the interaction parameters for real liquids.

By relaxing the definition of the length scale r_c, we generated reasonable interaction parameters from bottom-up for water and significantly improved the precision of predicting the surface tension of three mixtures. In principle, this parametrisation protocol can be applied to any other liquid.

This parametrisation now enables to rigorously apply many-body dissipative particle dynamics to solid/liquid or liquid/gas interfaces of soft matter systems, or porous structures in general, and expect more accurate predictions vis à vis experimental data. To point at one possible application, which is both industrially important as well as relevant in the context of this thesis, we mention the porous structure of the catalyst layer of fuel cells, which is the main bottleneck in the performance and commercial deployment of the fuel cells in transport, and, as a result, has been the source of extensive research effort in the past few decades [69].

Appendix: Fitting

Here, we describe in more detail the fitting procedure for the densities and surface tensions as functions of interaction parameters A, B discussed in the main paper. For all the fits, we used the function `curve_fit` from the Scipy library [3].

Density profiles

By visually inspecting the cuts of the density surface $\rho(A, B)$ it is possible to guess several trial functions. At constant B, the density varies linearly in the liquid and solid regime for $A < -20$, whereas at constant A, the variation follows the power law: $(B - \beta_1)^{\beta_2}$. Example cuts are shown in Fig. 6.12.

We applied two versions of the fitting function, composed as the linear combination of the line and the power law, one containing three and the other four parameters. To gauge their relative performance, we randomly split the data into training and validation sets with 80/20 ratio, respectively. We carried out 500 such splits and estimated the average root-mean-square error (RMSE) in the validation set. For further certainty, we also computed the median RMSE to verify that the distribution of the RMSEs is normal. This turned out to be the the case, which was marked by the similar values of median and average RMSE.

The results shown in Table 6.9 reliably conclude that the four-parameter fit performs better for all of the many-body cutoffs r_d. However, considering the similarity of the RMSEs and the fact that later, in Section IV of the paper, we would use this fit for deriving the interaction parameters A, B via minimisation, we decided to proceed with the three-parameter fit. The parameters for each of the explored values of r_d are summarised in Table 6.1.

	$\rho(A, B)$	N_param	Avg RMSE (r_d)		
			0.65	0.75	0.85
1.	$c_1 + c_2(-A)(B - c_3)^{c_4}$	4	0.20	0.16	0.13
2.	$c_1 + c_2(-A)B^{c_3}$	3	0.21	0.18	0.16

Table 6.9: Attempted fitting functions for density $\rho(A, B)$ and their respective average RMSEs vs r_d's.

[3] https://docs.scipy.org/doc/scipy/reference/generated/scipy.optimize.curve_fit.html

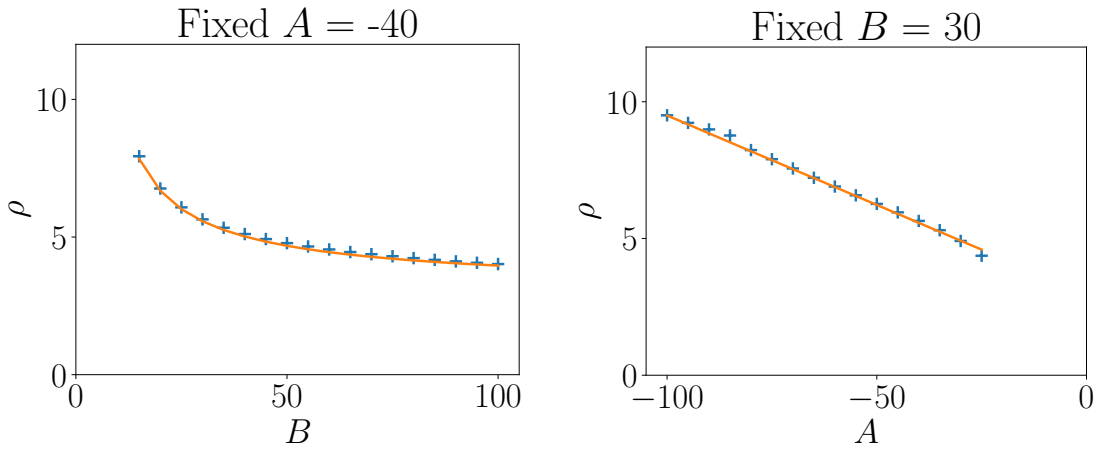

Figure 6.12: Example density surface cuts at $r_d = 0.75$ (in reduced units), suggesting linear and power law variation with A and B, respectively.

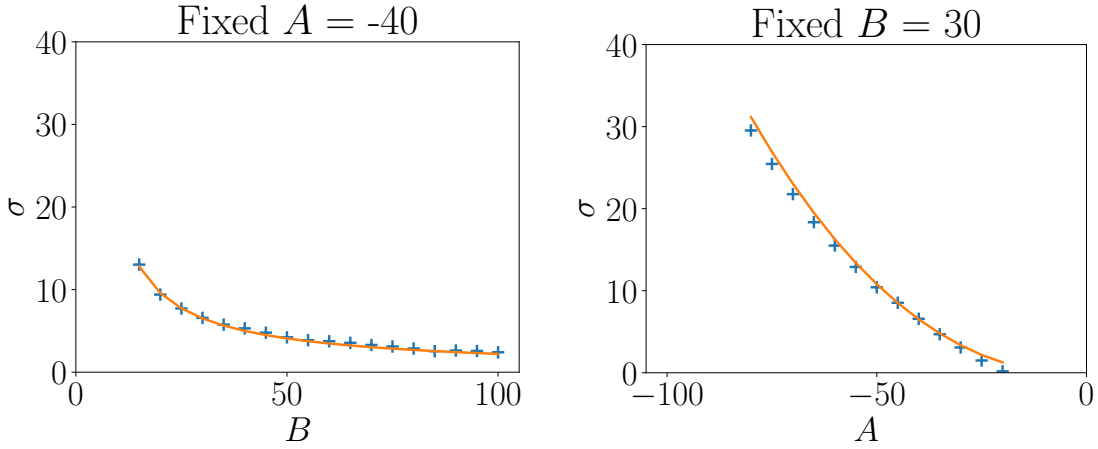

Figure 6.13: Examples of surface tension surface cuts for $r_d = 0.75$ (in reduced units).

Surface tension profiles

Visual inspection of the surface tension as a function of A, B (Fig. 6.13) suggest more candidates for fitting functions. The cuts at constant B seemed to indicate a quadratic dependence on A, whereas the cuts at constant A gave a power law, as in case of density.

We tried 10 linear combinations of these two functions. In each case, we followed the protocol outlined in the section I.: splitting the data 500 times into training and validation sets with 80/20 ratio, and for each split fitting on the training set and computing the RMSE on the points from the validation set.

The average and median RMSEs showed a non-negligible difference. In such case, we considered median to be a more appropriate measure of the quality of a fitting function. The trial fitting functions and their respective median RMSEs are summarised in Table 6.10. Each r_d is best represented by a different function. Deciding between functions with very similar values of median RMSEs, which happened at $r_d = 0.85$, we chose the one with the lower number of parameters. The resulting function choices for each value of r_d are summarised in Table 6.2.

	$\sigma(A,B)$	N_{param}	Median RMSE (r_{d})		
			0.65	0.75	0.85
1.	$(c_1A^2+c_2A+c_3)(B-c_4)^{c_5}$	5	3.64	1.80	0.34
2.	$(c_1A^2+c_2A+c_3)(B-c_4+c_5A)^{c_6}$	6	**2.09**	NA	0.34
3.	$(c_1A^2+c_2A+c_3)(B-c_4)^{c_5+c_6A}$	6	3.76	1.66	0.33
4.	$(c_1A^2+c_2A)(B-c_3)^{c_4}$	4	3.65	1.76	**0.34**
5.	$(c_1A^2+c_2)(B-c_3)^{c_4}$	4	3.65	1.67	0.39
6.	$(c_1A^3+c_2A^2+c_3A+c_4)(B-c_5)^{c_6}$	6	3.39	1.90	0.34
7.	$(c_1A^3+c_2A^2+c_3A)(B-c_4)^{c_5}$	5	3.49	1.86	0.34
8.	$(c_1A^2+c_2A)B^{c_3}$	3	3.91	1.74	0.51
9.	$(c_1A^2+c_2A+c_3)B^{c_4}$	4	3.88	1.78	0.51
10.	$(c_1A^2+c_2A)(B+c_3A)^{c_4}$	4	2.33	**1.47**	0.43

Table 6.10: Attempted fitting functions for surface tension $\sigma(A,B)$ and their respective median RMSEs vs r_{d}. The numbers in bold point at the best-fitting functions given the number of parameters.

Chapter 7

Thin Nafion films via many-body DPD

> Kancelária nesmie slúžiť ako zhromaždisko pre voľnú debatu nepracovného charakteru, popíjania kávy bez pracovnej náplne, či inej pracovnej nečinnosti.
>
> *Minutes from a business meeting*

Having developed the parametrisation for many-body dissipative particle dynamics in the previous chapter, we apply it here for the first time to industrial soft matter systems. We simulate an unconfined thin Nafion film on carbon support, a typical setting found in the catalyst layer of fuel cells. The results reveal several insights, including the hairy caterpillar structure of the PTFE backbone chains on the surface, periodic clustering of water, and the transition from hydrophilic to hydrophobic behaviour with increasing film thickness.

In the catalyst layer (CL) of fuel cells, thin ionomer films of thickness of the order of several nanometres cover the porous structure created by the carbon support with attached catalytic PGM nanoparticles. This environment is delicate structure in which protons tunnel through the water channels in the ionomer, the electrons arrive through the carbon support, and oxygen passes from the air and through the ionomer film to form water via the oxygen reduction reaction on the surface of the nanoparticles.

The CL is a key performance bottleneck in fuel cell operation. However, due to its complicated structure spreading several length scales, it is very difficult to obtain experimental data and analyse the effects of various independent variables. Therefore simulations can play a vital role.

Building on the DPD simulations of thin but confined ionomer (Nafion) films with no wapour phase [20, 85] presented in Chapter 2, we exploit many-body dissipative particle dynamics (MDPD) with the parametrisation scheme developed in Chapter 6 to simulate a more realistic

experimental setting of the CL. We hope to gain insight into the equilibrium structure of an unconfined thin ionomer film deposited on carbon support and distribution of water at a range of distances from the carbon support.

7.1 Simulation details

As in case of standard DPD simulations in Chapter 2, we start by defining water as the default material and the coarse-graining (CG) degree $N_\mathrm{m} = 6$, which was first used by Wu *et al.* for bulk Nafion simulations [14]. Each MDPD bead thus contains a volume roughly equivalent to six water molecules. Setting the many-body cutoff $r_\mathrm{d} = 0.75$, a suitable value according to findings summarised in Chapter 6, the MDPD interaction parameters (A, B) can now be computed by matching compressibility and surface tension with experimental values for pure water. This procedure yields $A = -17.9$, $B = 7.9$ and the reduced number density of MDPD beads $\rho = 6.70$.

The temperature in the simulation is set to ambient conditions, $T = 300$ K, and defines the energy scale $k_\mathrm{B}T$ as one of the reduced units apart from the mass scale $m_\mathrm{c} = N_\mathrm{m} \times 18$ AMU,[1] which is the mass of one bead containing six water molecules, and the length scale r_c:

$$r_\mathrm{c} = (\rho N_\mathrm{m} V_0)^{1/3} = 1.064 \text{ nm}, \tag{7.1}$$

where $V_0 = 30$ Å^3 is the average volume per water molecule. From these units also follows the time scale is $\tau = \sqrt{m_\mathrm{c} r_\mathrm{c}^2 / k_\mathrm{B}T} = 2.58$ ps.

Unlike bead interactions δA_{ij} are obtained from the Flory-Huggins χ-parameters as follows:

$$\Delta A_{ij} = 1.027\, \chi_{ij}, \tag{7.2}$$

where the values of χ_{ij} are taken from Wu *et al.*, where available, as well as from the Hildebrand solubilities for the cross-interactions involving carbon (Table 7.1). Following Warren's no-go theorem [111], the values of ΔB_{ij} are kept constant for all pairs (i, j).

As before in Chapters 2 and 3, we consider Nafion chains with polymerisation of 15 monomers per chain, with each monomer composed of five beads (Fig. 2.1). Each A bead contains six CF_2 groups, a structure corresponding to an equivalent weight (EW)[2] of about 1200. This is close to Nafion 117 with 1100 g/mol EW, which is considered an industrial standard.

The vapour phase is approximated by empty space. This is reasonable, since, at 100% relative humidity at 20 °C, the density of water in air is about 20 g/m^3. This corresponds to 25 water molecules in the volume of a typical simulation cell of side $L \approx 30$ nm, or about four W beads. This is in practice a negligible number. Throughout the simulation of thin films, several water beads escaped into the empty space, so the VMD screenshots depicted a visible vapour phase, but the density profiles revealed no significant mass contribution of this phase.

[1] Atomic mass unit, 1.66×10^{-27} kg.

[2] Equivalent weight is defined as the mass of dry PTFE backbone per mole of sulfonic acid groups.

	δ (MPa$^{1/2}$)	χ (no units)			
		A	B	C	W
A	12.7	0			
B	13.6	1.23	0		
C	23.0	7.44	2.70	0	
W	47.8	3.36	1.53	1.48	0
E	25.0	1.10	0.94	0.03	3.77

Table 7.1: Flory-Huggins χ-parameters defined between pairs of beads of a given type (A, B, C, W, or E) used in the simulation, also used in Chapter 2.

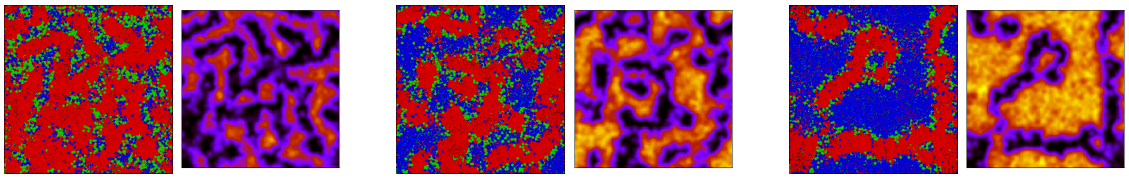

(a) $\lambda = 9$ (b) $\lambda = 16$ (c) $\lambda = 24$

Figure 7.1: VMD screenshots of the simulation cell and water density profiles for bulk Nafion simulated via many-body DPD at various water contents λ. Coloring follows convention set in Chapter 2: blue is water, red backbone and green sulfonic acid groups.

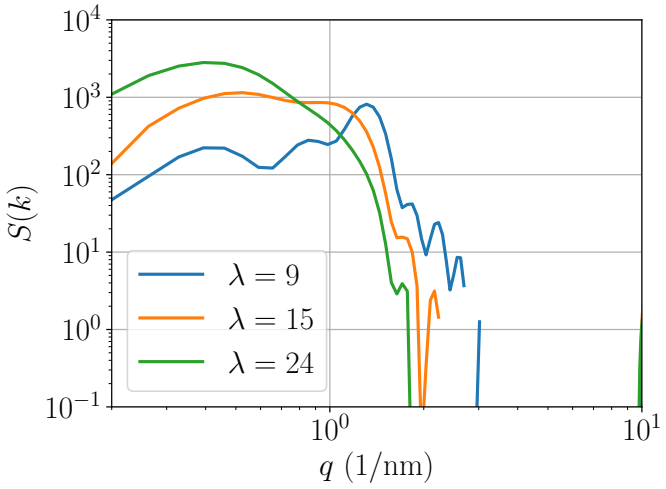

Figure 7.2: Structure factors of bulk Nafion as a function of water content λ. The peaks representing cluster spacing move towards lower wavelengths q with increasing λ, in agreement with experiment.

Table 7.2: Scattering maxima $q_{\max}$ as a function of water content, both in terms of λ and volume fraction (wt) and the resulting water cluster spacing d. Comparison with experimental trends in Fig. 3 in Elliott *et al.* [112].

λ	Vol. frac.	$q_{\max}$ (nm^{-1})	d (nm)
9	0.250	1.312	2.39
15	0.357	0.525	5.99
24	0.471	0.394	7.98

7.2 Verification: Bulk Nafion

Before embarking on simulations of unconfined thin Nafion film using MDPD, we verify that this method is able to reproduce the key properties of bulk Nafion that are well-documented in the literature [17, 14]. We explored three water contents λ defined as the number of water molecules per sulfonic acid group of the ionomer: 9, 15 (approximately equal to 100% relative humidity) and 24. Setting the cell $30 \times 30 \times 30$, we simulate for 200k steps with timestep $\Delta t = 0.01\tau$, so the total simulation time is $T = 2000\tau$. This should be sufficient for equilibration based on findings by Yamamoto [17], who explored in Fig. 6 in their paper times up to $T = 10000\tau$. From the last frame we compute the radial distribution functions (RDF) $g(r)$ of W beads and two-dimensional density profiles across the plane cuts. From these RDFs, structure factors of water, which are a key experimental observable, are subsequently calculated as follows:

$$S(k) = 1 + \rho \int_0^\infty (g(r) - 1) \frac{\sin(kr)}{kr} 4\pi r^2 \, dr. \tag{7.3}$$

Fig. 7.2 shows these structure factors. The position of the main peak demonstrating the distance between the clusters shifts to the left with increasing water content, in line with experiment. Computing the peak maxima $q_{\max}$ yields the average distance between water clusters d via the Bragg's law: $2d = n\lambda$. Setting $n = 1$ and using $\lambda = 2\pi/q_{\max}$ leads to $d = \pi/q_{\max}$. Comparison of the scattering maxima in Table 7.2 with experiments performed by Elliott *et al.*[112] (Fig. 3 in their paper, also Fig. 3 in James *et al.* [113]) is satisfactory, if qualitatively not exact. Hence, we conclude that MDPD can be relied upon as a mesoscale simulation method for complex polymer systems.

7.3 Thin film profiles

Having verified that MDPD is able to qualitatively capture the structure of bulk Nafion, we now proceed with simulations of thin Nafion film on carbon support. We vary water content λ from 3, essentially a dry state, up to 24, which corresponds to significant solvation. Fixing the thickness of the carbon support to 5 nm, we investigate ionomer films put on carbon surface of the following thicknesses: 2, 3, 5, 10, 15 and 20 nm. As before, we set the simulation cell $30 \times 30 \times 30$ in reduced units, with side equal to about 32 nm, and simulate for 100k steps using time step $\Delta t = 0.02\tau$, corresponding to physical time of $T = 2000\tau = 5.7$ ns.

Fig. 7.3 shows one-dimensional density profiles of water and backbone across the x-coordinate for 5, 10 and 15 nm, along which is the interface with the vapour phase. At low values of λ, there is a tendency to form periodic structures of excess and lack of water with wavelength of

about 5–6 nm, persisting up to $\lambda = 9$–12.

Films of thickness of 5 nm or thinner behave very differently, as shown on Fig. 7.4. There is clearly not enough space to accommodate the water inside the film, so nearly all water is displaced to the outside surface of the film. As a result, the PTFE backbone shrinks and adheres to the carbon surface. Hence, very thin ionomers can be considered hydrophilic in that water sticks to their outside surface.

On the other hand, 10, 15 and 20 nm films are hydrophobic at low values of λ, but eventually, passing through $\lambda = 15$ for 10 nm and $\lambda = 9$ for 15 nm, hydrophilicity sets on and at higher contents $\lambda > 18$ a large pool of water appears on the outer surface of the film as well.

To further probe the structure of the thin Nafion film, we analyse water density on the slices parallel to the film for thicknesses 5, 10 and 15 nm. We compute density profiles by smearing W beads and one half of C beads on a grid with a Gaussian function. We focus our analysis on the water contents that most resemble the operational conditions of a fuel cell: $\lambda = 9$ to 15.

Fig. 7.5 shows water densities at various distances from the substrate. For 3-5 nm above substrate surface, clustering is established and there is no evidence of a continuous pool of water that would indicate a lamellar phase, which has been suggested several times by the NIST group [56, 57]. All the explored film thicknesses have a depletion zone with very little water close to the substrate at a distance lower than 2 nm. Water uptake $\lambda = 15$, which corresponds to relative humidity 100% [113] and which is shown on Fig. 7.6, reveals the same depletion zone close to the substrate, but also considerably larger clusters and strong percolation across all of the simulation cell for distances greater than 3 nm from the carbon support.

7.4 Larger-scale simulations

Finally, to explore systems more comparable to available experimental data, we run a larger-scale simulation in a cell of size $60 \times 60 \times 60$, i.e. 66 nm in real units. Such a scale enables a clear depiction of water clusters and comparison with available atomic force microscopy (AFM) data obtained by James *et al.* [113]. Fig. 5 (vi) in their paper shows a 1000 nm screenshot of the surface of bulk Nafion at 33% relative humidity. The simulation details are the same as before with timestep $\Delta t = 0.02\tau$ and 100k simulation steps. The cell containing 5 nm film was minimised by running at temperature $0.01 k_{\mathrm{B}} T_{\mathrm{c}}$ prior to simulation.

Focusing again on water uptakes $\lambda = 9$ and 15 as most relevant for operational conditions, the thin film outer surfaces bordering the vapour phase are visualised on Fig. 7.7. The variation in the size of blue water regions on these screenshots unambiguously illustrates a gradual shift from hydrophilic behaviour at low film thicknesses, where water is pushed to the outer surface of the ionomer (Fig. 7.7a), up to hydrophobic behaviour at higher film widths (Fig. 7.7c). Furthermore, increasing water content λ also tends to push water to the outside ionomer surface and thus make it hydrophilic.

The practical consequences of these findings for fuel cell operation lie in the aim to keep the outer thin film surface hydrophobic. Water should not accumulate here and block the incoming oxygen from air arriving at the nanoparticle surface right under the ionomer. Our simulations suggest that hydrophobic film surface can be achieved by simply increasing the film width above

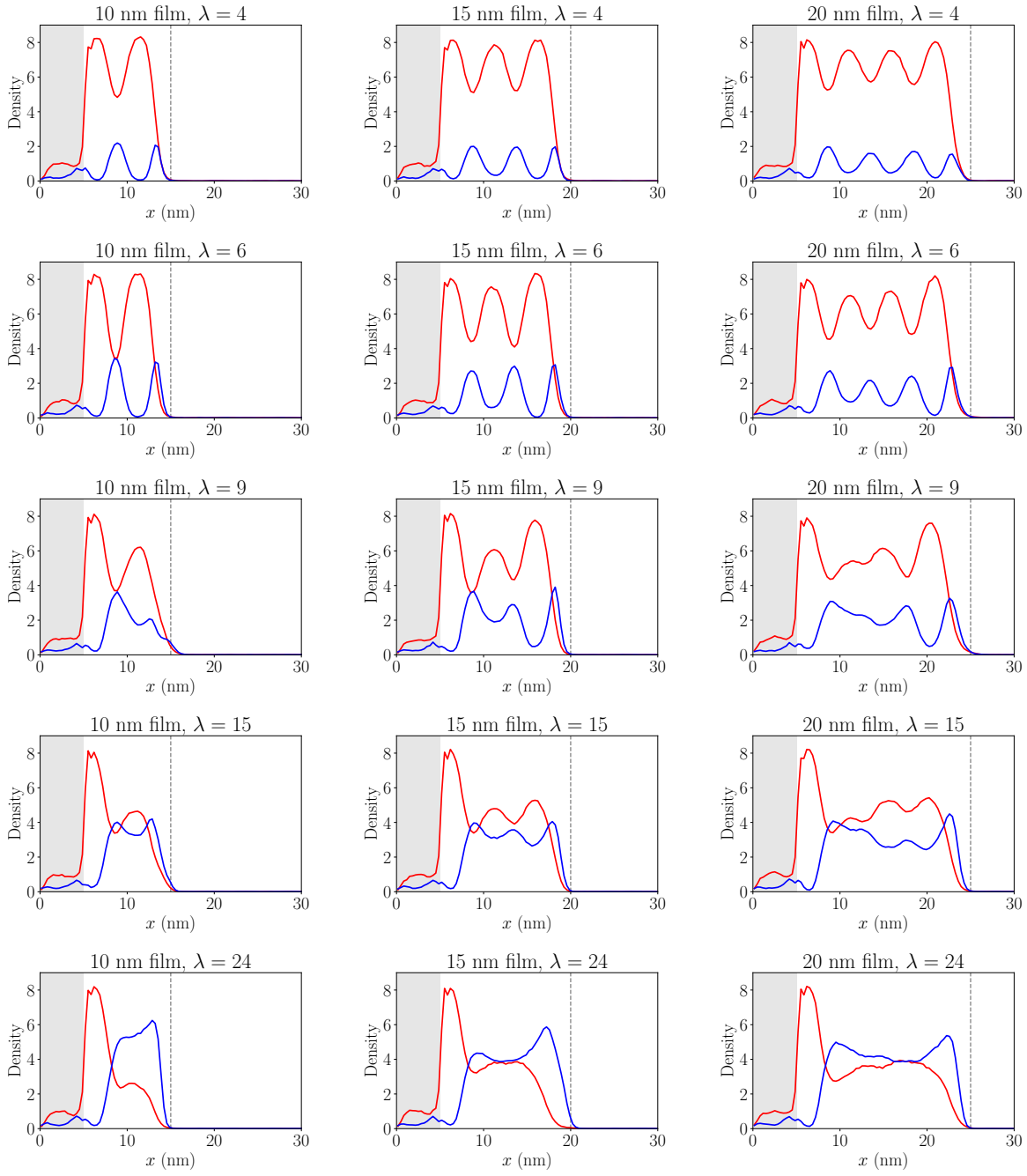

Figure 7.3: Relative density profiles of water (blue) and PTFE backbone (red) along x-axis, showing the coexistence with the vapour phase (free space) for water contents ranging (vertically) between $\lambda = 4$ and 24.

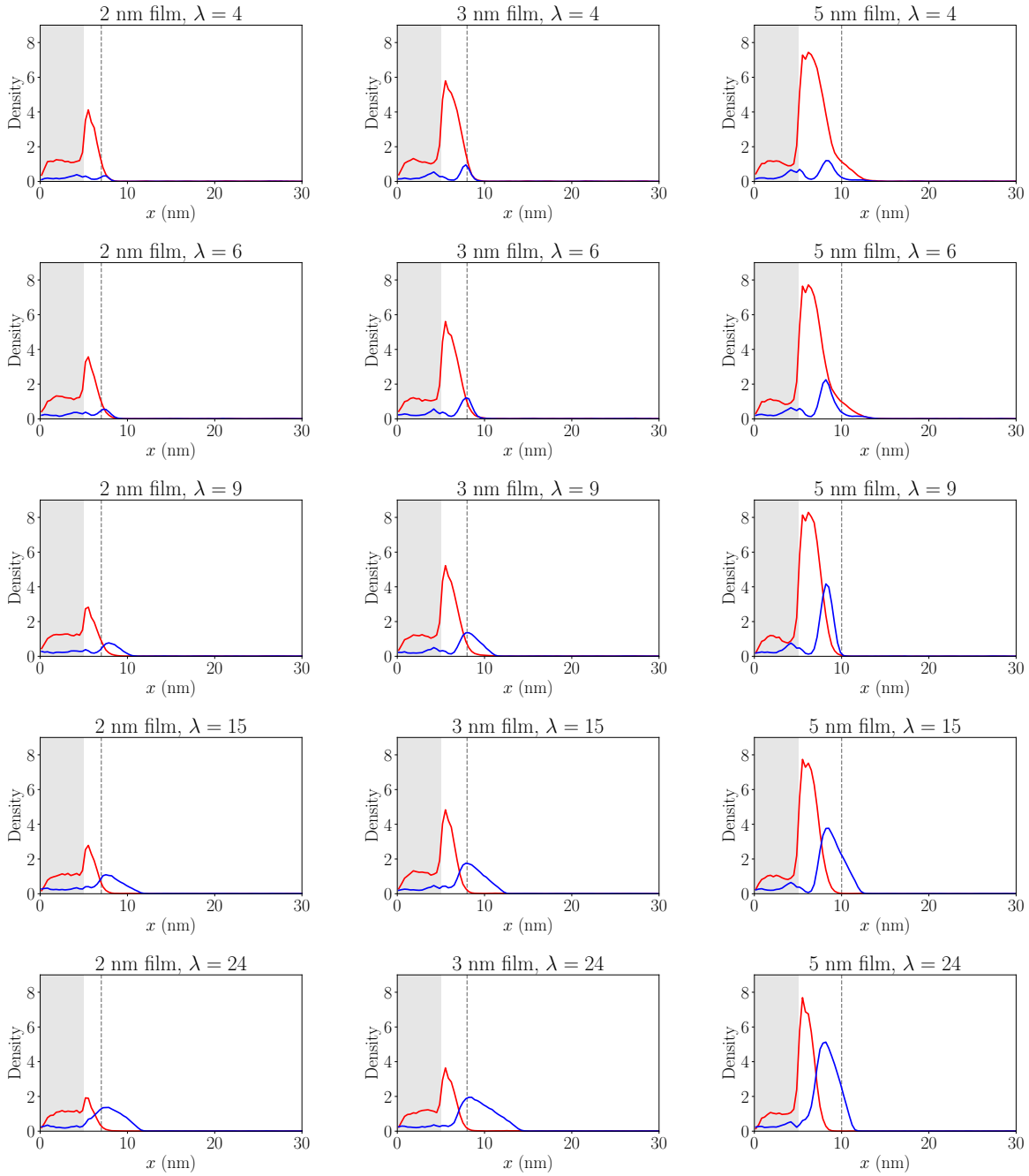

Figure 7.4: Relative density profiles of water (blue) and PTFE backbone (red) along x-axis, showing the coexistence with the vapour phase (free space) for water contents ranging (vertically) between $\lambda = 4$ and 24.

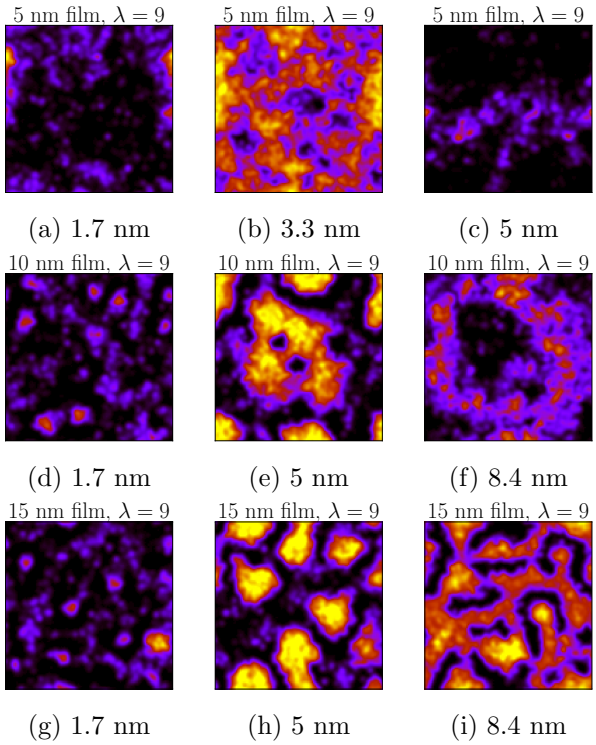

(a) 1.7 nm (b) 3.3 nm (c) 5 nm

(d) 1.7 nm (e) 5 nm (f) 8.4 nm

(g) 1.7 nm (h) 5 nm (i) 8.4 nm

Figure 7.5: Slices through Nafion films depicting water clusters and channels at a varying distance from the substrate at water content $\lambda = 9$.

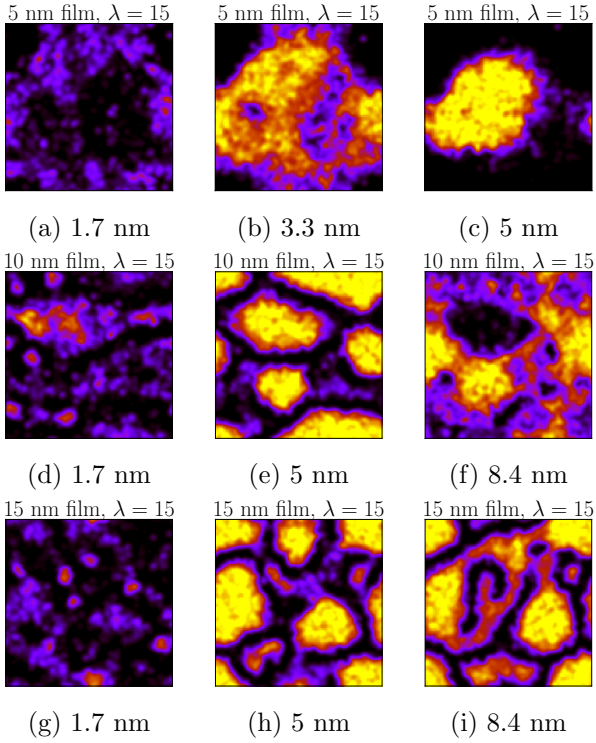

(a) 1.7 nm (b) 3.3 nm (c) 5 nm

(d) 1.7 nm (e) 5 nm (f) 8.4 nm

(g) 1.7 nm (h) 5 nm (i) 8.4 nm

Figure 7.6: Slices through Nafion films depicting water clusters and channels at a varying distance from the substrate at water content $\lambda = 15$.

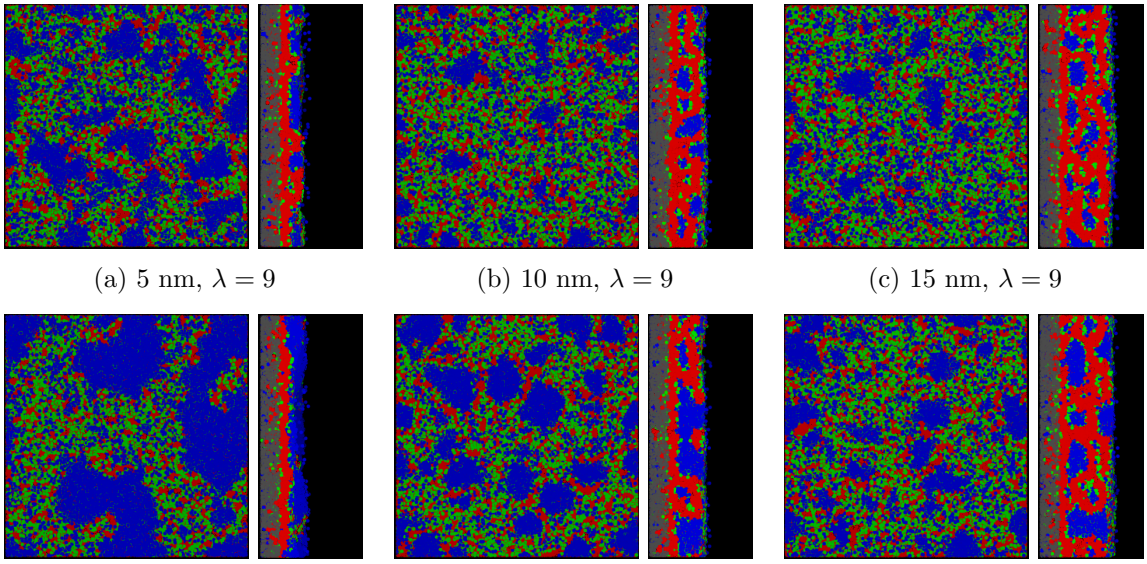

(a) 5 nm, $\lambda = 9$ (b) 10 nm, $\lambda = 9$ (c) 15 nm, $\lambda = 9$

(d) 5 nm, $\lambda = 15$ (e) 10 nm, $\lambda = 15$ (f) 15 nm, $\lambda = 15$

Figure 7.7: VMD screenshots (color coding: water in blue, backbone in red, sulfonic acid groups in green) of large-scale thin ionomer films in a 66 nm simulation cell depicting gradual shift from hydrophilic to hydrophobic behaviour with increasing film width.

a certain threshold lying between 5 and 10 nm. On the other hand, oxygen permeation through the ionomer decreases with increasing film thickness. The need to maximise these two opposing processes suggests an optimal intermediate value of film thickness.

7.5 Conclusions

In this chapter we employed for the first time many-body dissipative particle (MDPD) dynamics in simulations of complex polymers. Firstly, we explored bulk Nafion, which has already been well-studied in the literature. Having verified that MDPD yields plausible results, we investigated thin ionomer films on carbon support, a setting typical for the catalyst layer of a PEMFC. We have explored a wide range of conditions at ambient temperature, varying the ionomer film width and water content λ.

We found out that thin films of thickness below 5 nm cannot accommodate water within and expel it to their outer surface. In other worlds, their surface is hydrophilic, an undesirable effect for fuel cell performance. With increasing film thickness, periodic structures of excess and lack of water are formed at a typical wavelength of 5–6 nm, and the surface becomes hydrophobic. However, with increasing water content above $\lambda \approx 9$, even relatively thicker films of 10 nm and above push water to their outer surface and the hydrophilicity sets on. Considering the internal structure of the film, two-dimensional water density maps reveal a well-established network of clusters and channels at intermediate water contents $\lambda = 9$ a phenomenon desirable for proton transport.

Our results demonstrate that MDPD can provide insight into the mesoscopic structure of the catalyst layer and thus aid performance optimisation of the key constituent of every fuel cell with respect to the structure of water channels and film thickness. Further research could involve

the investigation of the role of the size of PTFE chains, the ordering of side chains, different ionomer types, such as SSC or 3M, the type of support material or the effect of temperature.

Chapter 8

Conclusions and outlook

> Didn't you know that manuscripts don't burn?
>
> *Master and Margarita*

In this thesis we have employed mesoscale simulation methods to gain insight into a pressing industrial problem of the efficiency of hydrogen fuel cells serving as a vehicle engine. As this clean technology gradually gains traction in the automotive market, any improvement in performance or efficiency can increase the interest of consumers and consequently mitigate the emission of CO_2, which impacts climate change.

At the heart of a fuel cell is a proton exchange membrane, such as Nafion, which serves as an electrode separator and electrolyte. Its structure has now been debated for about 50 years and is still far from resolved. More importantly, there is a catalyst layer on both sides of this membrane; on the cathode, protons conducting through the membrane and electrons arriving via the outside circuit recombine with oxygen from air on the surface of catalytic nanoparticles, typically formed from platinum-group metals (PGMs) to form water. The combination of oxygen, electrons and protons is the process known as the oxygen reduction reaction (ORR) and is the most significant efficiency loss. For this reason, ORR has attracted a lot of scientific interest in the past decades.

The catalyst layer is an intricate porous environment with structures and empty spaces (pores) of the order of tens of nanometres. Here, carbon serves as a material that supports PGM nanoparticles as well as delivers the electrons to the nanoparticle surface. Both carbon and PGM nanoparticles are coated by a thin layer of ionomer of thickness of the order of a few nanometres; it is chemically the same material as the bulk membrane and conducts the protons to the nanoparticle surface.

It is very challenging to gain both experimental and theoretical insight into the structure and behaviour of the catalyst layer, especially the ionomer within the layer. Even outside the catalyst layer, it is difficult to prepare and probe polymer films only a few nanometres thick. Theoretically, it is very costly to simulate structures on the scale of tens to hundreds of nm. Hence, the focus of this thesis has been to develop suitable simulation tools to predict the structure and properties of these thin ionomer films.

Our starting point is dissipative particle dynamics (DPD), which has been established in the past 20 years as a useful tool for modelling soft matter systems on the mesoscale. Sadly,

this method is not able to simulate vapour-liquid coexistence or, in plain words, a liquid blob with a free space around it. On the other hand, its extension called many-body DPD (MDPD), which does capture this setting, was not yet suitable for simulating real materials.

This reality motivated the theoretical aspect of this thesis. As a result, in Chapter 6 we presented a parametrisation method for MDPD to simulate materials based on macroscopic experimental quantities, which we chose to be surface tension and compressibility. Together with the Flory-Huggins theory describing unlike particle interaction parameters via the χ-parameter, we showed that this scheme delivers a certain degree of predictive accuracy. We have verified our method on a few binary solvent mixtures and proved that the results can be relied upon. Hence, MDPD is now ready to be applied to a broader range of systems that contain free spaces, notably porous structures.

An excellent example of such a structure with acute industrial importance is the cathode catalyst layer in PEM fuel cells. To test the ability of MDPD to describe complex polymers, in the first part of Chapter 7 we simulated bulk Nafion and showed that the density profiles as well as the structure of water clusters described via the structure factor and its main peak are in qualitative agreement with experiment. Furthermore, in the general exploration of the phase diagram of the MDPD force field we uncovered a solid phase with a thermodynamically stable bcc lattice, which might later be applied to solid-liquid interfaces on the mesoscale.

As an aside, in Chapter 4 we addressed some long-standing theoretical issues in standard DPD about the dependence of simulation parameters as well as experimental observables on the coarse-graining degree, and rederived the variation of the DPD interaction parameter with temperature. These results should lead to improved precision of standard DPD simulations.

On the practical side, we exploited both standard DPD and the newly parametrised MDPD with the aim to shed light on the behaviour of the ionomer within a fuel cell catalyst layer. In Chapter 2, we investigated a thin Nafion film confined on both sides by hydrophobic carbon and hydrophilic quartz via standard DPD for a range of water contents and film widths. The simulations revealed confinement-induced water clustering and thickness-dependent diffusivity anisotropy.

Finally, to fully exploit our MDPD parametrisation from Chapter 6, in Chapter 7 we explored an unconfined thin Nafion film with carbon support on one side and free space on the other, a setting very similar to that in a fuel cell catalyst layer. We investigated the role of thickness and water content on the structure of water in the thin ionomer film in a simulation cell of size about 60 nm, observing the tendency for the ionomer to cluster as well as switch from a hydrophilic to a hydrophobic film surface with decreasing water content and increasing film thickness. We found out that a 5 nm film or thinner repels most of the water to its outer surface, but, as the thickness increases, water is accommodated within the film, forming water clusters and channels suitable for proton transport.

Suggestions for future work

Having developed a tool to simulate water channels and clusters in thin films serving as pathways for proton transport, there still remains the question of oxygen diffusion through the film to the

nanoparticle surface, where it meets protons and electrons to form water, as well as subsequent water diffusion away from the nanoparticle surface. For example, what is the relative importance of water transport out through the film into the catalyst layer pore space vs transport within the ionomer film and into the membrane. As we showed, the thicker the ionomer film is, the better-established water clustering is and the more the ionomer resembles the bulk membrane. On the other hand, if the ionomer is too thick, it will slow down the rate of oxygen transport to the catalytic nanoparticle surface. Hence, we can expect an intermediate film thickness at which the total performance mediated by water, proton and oxygen transport is optimal. In future work therefore the predicted structure of the ionomer as a function of film thickness should be used to derive estimates of oxygen, water and proton transport rates through and within the thin ionomer film.

To start with more straightforward challenges, an obvious extension of the presented work, especially from Chapters 2 and 7, is a full exploration of the parameter space of thin films. Important variables to vary include the degree of polymerisation, equivalent weight, the role of polydispersity of PTFE chains, the ionomer material (trying ionomer types other than Nafion), the ordering of side chains (random vs uniform), different chain topologies, as were explored by, e.g., Dorenbos [24], or the effect of increased temperature. Many of these simulation results could be consequently verified by small-angle x-ray scattering (SAXS) or neutron reflectometry, which has been exploited by the NIST group [56, 57].

A more ambitious research would involve the investigation of oxygen diffusion. This is a formidable challenge for MDPD or generally any mesoscale method, as beads comprising several water molecules are of different size than oxygen molecules. Hence, it is not a priori clear whether this problem can be addressed at all by MDPD. So far, only systems with the same bead radius and mass have been explored by both DPD and MDPD; relaxing this constraint would be a worthwhile pursuit, especially given the industrial motivation. Firstly, however, a thorough investigation similar to the one exposed in Chapter 6 would have to be carried out to ensure that the simulation results are in line with experiment as well as established atomically-resolved models.

Finally, the development of MDPD in this thesis opens up avenues for broader exploration of soft matter in contact with free space, solid phase or vapour phase. There is already a substantial amount of research on soft matter with DPD; this can now be reproduced and extended using MDPD. Notable examples are diblock copolymer phases following the work in Ref. [11], or vesicle formation following Ref. [13]. More broadly, the ability of MDPD to describe porous structures might be beneficial in the oil and gas industry dealing with cracking, where hydrocarbons pass through porous materials such as zeolites. Another possible application involves predicting the properties of thin polymer films that serve as oxygen and moisture barriers used in the packaging industry.

Considering that the total revenue of oil and gas industry amounts to trillions of dollars,[1] and that fuel cell electric vehicles are expected to gain a significant market share in the following decades, the relevance of computer simulations on the mesoscale can only be expected to increase.

[1] https://www.statista.com/statistics/272710/top-10-oil-and-gas-companies-worldwide-based-on-revenue/

Bibliography

[1] G. Gebel. Structural evolution of water swollen perfluorosulfonated ionomers from dry membrane to solution. *Polymer*, 41(15):5829 – 5838, 2000. doi:10.1016/S0032-3861(99)00770-3.

[2] A. R. Leach. *Molecular Modelling: Principles and Applications*. Pearson, 2001.

[3] D. Frenkel and B. Smit. *Understanding Molecular Simulation*. Academic Press, 2002.

[4] P. J Hoogerbrugge and J. M. V. A Koelman. Simulating Microscopic Hydrodynamic Phenomena with Dissipative Particle Dynamics. *Europhysics Letters (EPL)*, 19(3):155–160, 2007. doi:10.1209/0295-5075/19/3/001.

[5] J. M. V. A Koelman and P. J Hoogerbrugge. Dynamic Simulations of Hard-Sphere Suspensions Under Steady Shear. *Europhysics Letters (EPL)*, 21(3):363–368, 1993. doi:10.1209/0295-5075/21/3/018.

[6] P Español and P Warren. Statistical mechanics of dissipative particle dynamics. *Europhysics Letters*, 30(4):191–196, 1995. doi:10.1209/0295-5075/30/4/001.

[7] Robert D. Groot and Patrick B. Warren. Dissipative particle dynamics: Bridging the gap between atomistic and mesoscopic simulation. *The Journal of Chemical Physics*, 107(11):4423, 1997. doi:10.1063/1.474784.

[8] Robert D. Groot, Timothy J. Madden, and Dominic J. Tildesley. On the role of hydrodynamic interactions in block copolymer microphase separation. *The Journal of Chemical Physics*, 110(19):9739–9749, 1999. doi:10.1063/1.478939.

[9] N. A. Spenley. Scaling laws for polymers in dissipative particle dynamics. *Europhysics Letters (EPL)*, 49(4):534–540, 2000. doi:10.1209/epl/i2000-00183-2.

[10] Naoki Kadoya and Noriyoshi Arai. Size dependence of static polymer droplet behavior from many-body dissipative particle dynamics simulation. *Phys. Rev. E*, 95:043109, Apr 2017. doi:10.1103/PhysRevE.95.043109.

[11] Robert D Groot and Timothy J Madden. Dynamic simulation of diblock copolymer microphase separation. *The Journal of Chemical Physics*, 108(3949):4804608–114904, 1998. doi:10.1063/1.1642602.

[12] R D Groot and K L Rabone. Mesoscopic simulation of cell membrane damage, morphology change and rupture by nonionic surfactants. *Biophysical journal*, 81(2):725–736, 2001. doi:10.1016/S0006-3495(01)75737-2.

[13] Satoru Yamamoto, Yutaka Maruyama, and Shi-Aki Hyodo. Dissipative particle dynamics study of spontaneous vesicle formation of amphiphilic molecules. *The Journal of Chemical Physics*, 116(13):5842–5849, 2002. doi:10.1063/1.1456031.

[14] Dongsheng Wu, Stephen J. Paddison, and James A. Elliott. A comparative study of the hydrated morphologies of perfluorosulfonic acid fuel cell membranes with mesoscopic simulations. *Energy & Environmental Science*, 1(2):284, 2008. doi:10.1039/b809600g.

[15] Dongsheng Wu, Stephen J. Paddison, and James A. Elliott. Effect of molecular weight on hydrated morphologies of the short-side-chain perfluorosulfonic acid membrane. *Macromolecules*, 42:3358–3367, 2009. doi:10.1021/ma900016w.

[16] Dongsheng Wu, Stephen J. Paddison, James A. Elliott, and Steven J. Hamrock. Mesoscale modeling of hydrated morphologies of 3m perfluorosulfonic acid-based fuel cell electrolytes. *Langmuir*, 26(17):14308–14315, 2010. doi:10.1021/la102358y.

[17] Satoru Yamamoto and Shi-Aki Hyodo. A Computer Simulation Study of the Mesoscopic Structure of the Polyelectrolyte Membrane Nafion. *Polymer Journal*, 35(6):519–527, 2003. doi:10.1295/polymj.35.519.

[18] Gert Dorenbos and Yoshinori Suga. Simulation of equivalent weight dependence of Nafion morphologies and predicted trends regarding water diffusion. *Journal of Membrane Science*, 330(1-2):5–20, 2009. doi:10.1016/j.memsci.2008.11.056.

[19] Gert Dorenbos and Kei Morohoshi. Chain architecture dependence of pore morphologies and water diffusion in grafted and block polymer electrolyte fuel cell membranes. *Energy & Environmental Science*, 3(9):1326, 2010. doi:10.1039/b924171j.

[20] G. Dorenbos, V. A. Pomogaev, M. Takigawa, and K. Morohoshi. Prediction of anisotropic transport in Nafion containing catalyst layers. *Electrochemistry Communications*, 12(1):125–128, 2010. doi:10.1016/j.elecom.2009.11.004.

[21] Gert Dorenbos and Kei Morohoshi. Modeling gas permeation through membranes by kinetic Monte Carlo: Applications to H2, O2, and N2 in hydrated Nafion. *Journal of Chemical Physics*, 134(4), 2011. doi:10.1063/1.3548663.

[22] G. Dorenbos and K. Morohoshi. Pore morphologies and diffusion within hydrated polyelectrolyte membranes: Homogeneous vs heterogeneous and random side chain attachment. *Journal of Chemical Physics*, 138(6), 2013. doi:10.1063/1.4789805.

[23] G. Dorenbos. Dependence of pore morphology and diffusion on hydrophilic site distribution within hydrated amphiphilic multi block co-polymer membranes. *Polymer (United Kingdom)*, 54(18):5024–5034, 2013. doi:10.1016/j.polymer.2013.07.007.

[24] G. Dorenbos. Searching for low percolation thresholds within amphiphilic polymer membranes: The effect of side chain branching. *The Journal of Chemical Physics*, 142(22):224902, 2015. doi:10.1063/1.4922156.

[25] G. Dorenbos. Morphology and diffusion within model membranes: Application of bond counting method to architectures with bimodal side chain length distributions. *European Polymer Journal*, 69:64–84, 2015. doi:10.1016/j.eurpolymj.2015.05.028.

[26] M. Karttunen I. Vattulainen A. Lukkarinen. *Novel Methods in Soft Matter Simulations*. Springer, 2004.

[27] Pep Español and Patrick B. Warren. Perspective: Dissipative particle dynamics. *The Journal of Chemical Physics*, 146(15):150901, 2017. doi:10.1063/1.4979514.

[28] J. C. Hull. *Options, Futures, and Other Derivatives*. Pearson, 2003.

[29] Fatemeh Sepehr and Stephen J. Paddison. Dissipative Particle Dynamics interaction parameters from ab initio calculations. *Chemical Physics Letters*, 645:20–26, 2016. doi:10.1016/j.cplett.2015.12.032.

[30] Rudolf M. Füchslin, Harold Fellermann, Anders Eriksson, and Hans-Joachim Ziock. Coarse graining and scaling in dissipative particle dynamics. *The Journal of Chemical Physics*, 130(21):214102, 2009. doi:10.1063/1.3143976.

[31] M. Doi. *Soft Matter Physics*. Oxford University Press, 2013.

[32] R. A. L. Jones. *Soft Condensed Matter*. Oxford University Press, 2002.

[33] C. M. Wijmans, B. Smit, and R. D. Groot. Phase behavior of monomeric mixtures and polymer solutions with soft interaction potentials. *Journal of Chemical Physics*, 114(17):7644–7654, 2001. doi:10.1063/1.1362298.

[34] Cun Feng Fan, Barry D Olafson, Mario Blanco, and Shaw Ling Hsu. Application of molecular simulation to derive phase diagrams of binary mixtures. *Macromolecules*, 25(14):3667–3676, 1992. doi:10.1021/ma00040a010.

[35] I. Pagonabarraga and D. Frenkel. Dissipative particle dynamics for interacting systems. *Journal of Chemical Physics*, 115(11):5015–5026, 2001. doi:10.1063/1.1396848.

[36] S. Y. Trofimov, E. L F Nies, and M. A J Michels. Thermodynamic consistency in dissipative particle dynamics simulations of strongly nonideal liquids and liquid mixtures. *Journal of Chemical Physics*, 117(20):9383–9394, 2002. doi:10.1063/1.1515774.

[37] P B Warren. Vapor-liquid coexistence in many-body dissipative particle dynamics. *Physical review. E, Statistical, nonlinear, and soft matter physics*, 68(6 Pt 2):066702, 2003. doi:10.1103/PhysRevE.68.066702.

[38] Safa Jamali, Arman Boromand, Shaghayegh Khani, Jacob Wagner, Mikio Yamanoi, and Joao Maia. Generalized mapping of multi-body dissipative particle dynamics onto

fluid compressibility and the flory-huggins theory. *The Journal of Chemical Physics*, 142(16):164902, 2015. doi:10.1063/1.4919303.

[39] Aziz Ghoufi, Janine Emile, and Patrice Malfreyt. Recent advances in Many Body Dissipative Particles Dynamics simulations of liquid-vapor interfaces. *The European physical journal. E, Soft matter*, 36(1):10, 2013. doi:10.1140/epje/i2013-13010-7.

[40] A. Ghoufi and P. Malfreyt. Calculation of the surface tension from multibody dissipative particle dynamics and monte carlo methods. *Phys. Rev. E*, 82:016706, Jul 2010. doi:10.1103/PhysRevE.82.016706.

[41] A. Ghoufi and P. Malfreyt. Mesoscale modeling of the water liquid-vapor interface: A surface tension calculation. *Physical Review E - Statistical, Nonlinear, and Soft Matter Physics*, 83(5):1–5, 2011. doi:10.1103/PhysRevE.83.051601.

[42] Aziz Ghoufi and Patrice Malfreyt. Coarse grained simulations of the electrolytes at the water-air interface from many body dissipative particle dynamics. *Journal of Chemical Theory and Computation*, 8(3):787–791, 2012. doi:10.1021/ct200833s.

[43] Xin Yong. Hydrodynamic interactions and entanglements of polymer solutions in many-body dissipative particle dynamics. *Polymers*, 8(12), 2016. doi:10.3390/polym8120426.

[44] M. P. Allen and D. J. Tildesley. *Computer Simulation of Liquids*. Clarendon Press, 1989.

[45] Kenneth A. Mauritz and Robert B. Moore. State of understanding of Nafion. *Chemical Reviews*, 104:4535–4585, 2004. doi:10.1021/cr0207123.

[46] Klaus-Dieter Kreuer, Stephen J. Paddison, Eckhard Spohr, and Michael Schuster. Transport in proton conductors for fuel-cell applications: Simulations, elementary reactions, and phenomenology. *Chemical Reviews*, 104(10):4637–4678, 2004. doi:10.1021/cr020715f. PMID: 15669165.

[47] Adam Z. Weber and John Newman. Modeling transport in polymer-electrolyte fuel cells. *Chemical Reviews*, 104(10):4679–4726, 2004. doi:10.1021/cr020729l. PMID: 15669166.

[48] S.J. Paddison. Proton Conduction Mechanisms At Low Degrees of Hydration in Sulfonic Acid-Based Polymer Electrolyte Membranes. *Annual Review of Materials Research*, 33:289–319, 2003. doi:10.1146/annurev.matsci.33.022702.155102.

[49] Ahmet Kusoglu and Adam Z. Weber. New insights into perfluorinated sulfonic-acid ionomers. *Chemical Reviews*, 117(3):987–1104, 2017. doi:10.1021/acs.chemrev.6b00159. PMID: 28112903.

[50] T.D. Gierke, G.E. Munn, and F.C. Wilson. The Morphology in Nafion Perfluorinated Membrane Products, as Determined by Wide- and Small-Angle X-Ray Studies. *Journal of Polymer Science*, 19:1687–1704, 1981. doi:10.1002/pol.1981.180191103.

[51] L. Rubatat, A. L. Rollet, G. Gebel, and O. Diat. Evidence of elongated polymeric aggregates in nafion. *Macromolecules*, 35(10):4050–4055, 2002. doi:10.1021/ma011578b.

[52] Klaus Schmidt-Rohr and Qiang Chen. Parallel cylindrical water nanochannels in Nafion fuel-cell membranes. *Nature materials*, 7(1):75–83, 2008. doi:10.1038/nmat2074.

[53] Klaus Dieter Kreuer and Giuseppe Portale. A critical revision of the nano-morphology of proton conducting ionomers and polyelectrolytes for fuel cell applications. *Advanced Functional Materials*, 23(43):5390–5397, 2013. doi:10.1002/adfm.201300376.

[54] James A. Elliott, Dongsheng Wu, Stephen J. Paddison, and Robert B. Moore. A unified morphological description of Nafion membranes from SAXS and mesoscale simulations. *Soft Matter*, 7(15):6820, 2011. doi:10.1039/c1sm00002k.

[55] J. Larminie and A. Dicks. *Fuel Cell Systems Explained*. SAE International, 2003.

[56] Joseph A. Dura, Vivek S. Murthi, Michael Hartman, Sushil K. Satija, and Charles F. Majkrzak. Multilamellar interface structures in nafion. *Macromolecules*, 42(13):4769–4774, 2009. doi:10.1021/ma802823j.

[57] Steven C. DeCaluwe, Paul A. Kienzle, Pavan Bhargava, Andrew M. Baker, and Joseph A. Dura. Phase segregation of sulfonate groups in nafion interface lamellae, quantified via neutron reflectometry fitting techniques for multi-layered structures. *Soft Matter*, 10:5763–5776, 2014. doi:10.1039/C4SM00850B.

[58] Scott A. Eastman, Sangcheol Kim, Kirt A. Page, Brandon W. Rowe, Shuhui Kang, Christopher L. Soles, and Kevin G. Yager. Effect of confinement on structure, water solubility, and water transport in nafion thin films. *Macromolecules*, 45(19):7920–7930, 2012. doi:10.1021/ma301289v.

[59] Sangcheol Kim, Joseph A. Dura, Kirt A. Page, Brandon W. Rowe, Kevin G. Yager, Hae-Jeong Lee, and Christopher L. Soles. Surface-induced nanostructure and water transport of thin proton-conducting polymer films. *Macromolecules*, 46(14):5630–5637, 2013. doi:10.1021/ma400750f.

[60] Miguel A. Modestino, Devproshad K. Paul, Shudipto Dishari, Stephanie A. Petrina, Frances I. Allen, Michael A. Hickner, Kunal Karan, Rachel A. Segalman, and Adam Z. Weber. Self-assembly and transport limitations in confined nafion films. *Macromolecules*, 46(3):867–873, 2013. doi:10.1021/ma301999a.

[61] James A Elliott and Stephen J Paddison. Modelling of morphology and proton transport in PFSA membranes. *Physical chemistry chemical physics : PCCP*, 9(January):2602–2618, 2007. doi:10.1039/b701234a.

[62] G. Dorenbos. Improving proton conduction pathways in di- and triblock copolymer membranes: Branched versus linear side chains. *The Journal of Chemical Physics*, 146(24):244909, 2017. doi:10.1063/1.4989487.

[63] Ian Kendrick, Dunesh Kumari, Adam Yakaboski, Nicholas Dimakis, and Eugene S. Smotkin. Elucidating the ionomer-electrified metal interface. *Journal of the American Chemical Society*, 132(49):17611–17616, 2010. doi:10.1021/ja1081487. PMID: 21087013.

[64] Amin Nouri-Khorasani, Kourosh Malek, and Michael Eikerling. Molecular Modeling of Hydronium Ion and Water Distribution in Water-Filled Pt Nanochannels with Corrugated Walls. *Electrocatalysis*, 5(2):167–176, 2014. doi:10.1007/s12678-013-0174-x.

[65] Amin Nouri-Khorasani, Kourosh Malek, Ali Malek, Tetsuya Mashio, David P. Wilkinson, and Michael H. Eikerling. Molecular modeling of the proton density distribution in a water-filled slab-like nanopore bounded by Pt oxide and ionomer. *Catalysis Today*, 262:133–140, 2016. doi:10.1016/j.cattod.2015.10.020.

[66] Daiane Damasceno Borges, Gerard Gebel, Alejandro A. Franco, Kourosh Malek, and Stefano Mossa. Morphology of supported polymer electrolyte ultrathin films: A numerical study. *The Journal of Physical Chemistry C*, 119(2):1201–1216, 2015. doi:10.1021/jp507598h.

[67] Daiane Damasceno Borges, Alejandro A. Franco, Kourosh Malek, Gerard Gebel, and Stefano Mossa. Inhomogeneous transport in model hydrated polymer electrolyte supported ultrathin films. *ACS Nano*, 7(8):6767–6773, 2013. doi:10.1021/nn401624p. PMID: 23829411.

[68] Mark K. Debe. Electrocatalyst approaches and challenges for automotive fuel cells. *Nature*, 486(7401), 2012. doi:10.1038/nature11115. Review Article.

[69] Adam Z Weber and Ahmet Kusoglu. Unexplained Transport Resistances for Low-Loaded Fuel-Cell Catalyst Layers. *Journal of Materials Chemistry A*, 2(c):17207–17211, 2014. doi:10.1039/C4TA02952F.

[70] Zhi Wei Seh, Jakob Kibsgaard, Colin F. Dickens, Ib Chorkendorff, Jens K. Nørskov, and Thomas F. Jaramillo. Combining theory and experiment in electrocatalysis: Insights into materials design. *Science*, 355(6321), 2017. doi:10.1126/science.aad4998.

[71] Vojislav R. Stamenkovic, Ben Fowler, Bongjin Simon Mun, Guofeng Wang, Philip N. Ross, Christopher A. Lucas, and Nenad M. Markovic. Improved oxygen reduction activity on pt3ni(111) via increased surface site availability. *Science*, 2007. doi:10.1126/science.1135941.

[72] Vojislav R Stamenkovic, Bongjin Simon Mun, Matthias Arenz, Karl JJ Mayrhofer, Christopher A Lucas, Guofeng Wang, Philip N Ross, and Nenad M Markovic. Trends in electrocatalysis on extended and nanoscale pt-bimetallic alloy surfaces. *Nature materials*, 6(3):241, 2007. doi:10.1038/nmat1840.

[73] J Snyder, T Fujita, MW Chen, and J Erlebacher. Oxygen reduction in nanoporous metal–ionic liquid composite electrocatalysts. *Nature materials*, 9(11):904, 2010. doi:10.1038/nmat 2878.

[74] Deli Wang, Huolin L Xin, Robert Hovden, Hongsen Wang, Yingchao Yu, David A Muller, Francis J DiSalvo, and Héctor D Abruña. Structurally ordered intermetallic platinum–cobalt core–shell nanoparticles with enhanced activity and stability as oxygen reduction electrocatalysts. *Nature materials*, 12(1):81, 2013. doi:10.1038/nmat3458.

[75] Sheng Dai, Yuan You, Shuyi Zhang, Wei Cai, Mingjie Xu, Lin Xie, Ruqian Wu, George W Graham, and Xiaoqing Pan. In situ atomic-scale observation of oxygen-driven core-shell formation in pt 3 co nanoparticles. *Nature communications*, 8(1):204, 2017. doi:10.1038/s41467-017-00161-y.

[76] Chen Chen, Yijin Kang, Ziyang Huo, Zhongwei Zhu, Wenyu Huang, Huolin L. Xin, Joshua D. Snyder, Dongguo Li, Jeffrey A. Herron, Manos Mavrikakis, Miaofang Chi, Karren L. More, Yadong Li, Nenad M. Markovic, Gabor A. Somorjai, Peidong Yang, and Vojislav R. Stamenkovic. Highly crystalline multimetallic nanoframes with three-dimensional electrocatalytic surfaces. *Science*, 343(6177):1339–1343, 2014. doi:10.1126/science.1249061.

[77] Michel Lefèvre, Eric Proietti, Frédéric Jaouen, and Jean-Pol Dodelet. Iron-based catalysts with improved oxygen reduction activity in polymer electrolyte fuel cells. *Science*, 324(5923):71–74, 2009. doi:10.1126/science.1170051.

[78] Jörg Behler and Michele Parrinello. Generalized neural-network representation of high-dimensional potential-energy surfaces. *Phys. Rev. Lett.*, 98:146401, Apr 2007. doi:10.1103/PhysRevLett.98.146401.

[79] Albert P. Bartók, Mike C. Payne, Risi Kondor, and Gábor Csányi. Gaussian approximation potentials: The accuracy of quantum mechanics, without the electrons. *Phys. Rev. Lett.*, 104:136403, Apr 2010. doi:10.1103/PhysRevLett.104.136403.

[80] Jörg Behler. Perspective: Machine learning potentials for atomistic simulations. *The Journal of Chemical Physics*, 145(17):170901, 2016. doi:10.1063/1.4966192.

[81] Ryo Kobayashi, Daniele Giofré, Till Junge, Michele Ceriotti, and William A. Curtin. Neural network potential for al-mg-si alloys. *Phys. Rev. Materials*, 1:053604, Oct 2017. doi:10.1103/PhysRevMaterials.1.053604.

[82] Zhenwei Li, James R. Kermode, and Alessandro De Vita. Molecular dynamics with on-the-fly machine learning of quantum-mechanical forces. *Phys. Rev. Lett.*, 114:096405, Mar 2015. doi:10.1103/PhysRevLett.114.096405.

[83] R D Groot and K L Rabone. Mesoscopic simulation of cell membrane damage, morphology change and rupture by nonionic surfactants. *Biophysical journal*, 81(2):725–736, 2001. doi:10.1016/S0006-3495(01)75737-2.

[84] Michael A. Seaton, Richard L. Anderson, Sebastian Metz, and William Smith. Dl_meso: highly scalable mesoscale simulations. *Molecular Simulation*, 39(10):796–821, 2013. doi:10.1080/08927022.2013.772297.

[85] P. Vanya, J. Sharman, and J. A. Elliott. Mesoscale simulations of confined nafion thin films. *The Journal of Chemical Physics*, 147(21):214904, 2017. doi:10.1063/1.4996695.

[86] Ryosuke Jinnouchi, Kenji Kudo, Naoki Kitano, and Yu Morimoto. Molecular Dynamics Simulations on O2 Permeation through Nafion Ionomer on Platinum Surface. *Electrochimica Acta*, 188:767–776, 2016. doi:10.1016/j.electacta.2015.12.031.

[87] Anusorn Kongkanand and Mark F. Mathias. The priority and challenge of high-power performance of low-platinum proton-exchange membrane fuel cells. *The Journal of Physical Chemistry Letters*, 7(7):1127–1137, 2016. doi:10.1021/acs.jpclett.6b00216. PMID: 26961326.

[88] William Y. Hsu, John R. Barkley, and Paul Meakin. Ion percolation and insulator-to-conductor transition in nafion perfluorosulfonic acid membranes. *Macromolecules*, 13(1):198–200, 1980. doi:10.1021/ma60073a041.

[89] Nicholas R Moloney Kim Christensen. *Complexity and Criticality*. Imperial College Press, 2005.

[90] A. Aharony D. Stauffer. *Introduction to Percolation Theory*. Taylor and Francis, 2003.

[91] Scott Kirkpatrick. Percolation and conduction. *Rev. Mod. Phys.*, 45:574–588, Oct 1973. doi:10.1103/RevModPhys.45.574.

[92] A. Orfanidi, P. Madkikar, H. A. El-Sayed, G. S. Harzer, T. Kratky, and H. A. Gasteiger. The key to high performance low pt loaded electrodes. *Journal of The Electrochemical Society*, 164(4):F418–F426, 2017. doi:10.1149/2.1621704jes.

[93] Amitesh Maiti and Simon McGrother. Bead–bead interaction parameters in dissipative particle dynamics: Relation to bead-size, solubility parameter, and surface tension. *The Journal of Chemical Physics*, 120(3):1594–1601, 2004. doi:10.1063/1.1630294.

[94] Rana A. Fine and Frank J. Millero. Compressibility of water as a function of temperature and pressure. *The Journal of Chemical Physics*, 59(10):5529–5536, 1973. doi:10.1063/1.1679903.

[95] S. Trofimov. *Thermodynamic consistency in dissipative particle dynamics*. PhD thesis, Technische Universiteit Eindhoven, 2003.

[96] Steve Plimpton. Fast parallel algorithms for short-range molecular dynamics. *Journal of Computational Physics*, 117(1):1 – 19, 1995. doi:https://doi.org/10.1006/jcph.1995.1039.

[97] Sergei Izvekov and Betsy M. Rice. Multi-scale coarse-graining of non-conservative interactions in molecular liquids. *The Journal of Chemical Physics*, 140(10):104104, 2014. doi:10.1063/1.4866142.

[98] W. G. Noid. Perspective: Coarse-grained models for biomolecular systems. *The Journal of Chemical Physics*, 139(9):090901, 2013. doi:10.1063/1.4818908.

[99] Robert Zwanzig. Ensemble method in the theory of irreversibility. *The Journal of Chemical Physics*, 33(5):1338–1341, 1960. doi:10.1063/1.1731409.

[100] Hazime Mori. Transport, collective motion, and brownian motion. *Progress of theoretical physics*, 33(3):423–455, 1965. doi:10.1143/PTP.33.423.

[101] Pep Español. Hydrodynamics from dissipative particle dynamics. *Phys. Rev. E*, 52:1734–1742, Aug 1995. doi:10.1103/PhysRevE.52.1734.

[102] Huan Lei, Bruce Caswell, and George Em Karniadakis. Direct construction of mesoscopic models from microscopic simulations. *Physical Review E - Statistical, Nonlinear, and Soft Matter Physics*, 81(2):1–10, 2010. doi:10.1103/PhysRevE.81.026704.

[103] Kevin R. Hadley and Clare McCabe. On the investigation of coarse-grained models for water: Balancing computational efficiency and the retention of structural properties. *The Journal of Physical Chemistry B*, 114(13):4590–4599, 2010. doi:10.1021/jp911894a. PMID: 20230012.

[104] Wendy D. Cornell, Piotr Cieplak, Christopher I. Bayly, Ian R. Gould, Kenneth M. Merz, David M. Ferguson, David C. Spellmeyer, Thomas Fox, James W. Caldwell, and Peter A. Kollman. A second generation force field for the simulation of proteins, nucleic acids, and organic molecules. *Journal of the American Chemical Society*, 117(19):5179–5197, 1995. doi:10.1021/ja00124a002.

[105] Richard L. Anderson, David J. Bray, Andrea S. Ferrante, Massimo G. Noro, Ian P. Stott, and Patrick B. Warren. Dissipative particle dynamics: Systematic parametrization using water-octanol partition coefficients. *The Journal of Chemical Physics*, 147(9):094503, 2017. doi:10.1063/1.4992111.

[106] Maryam Atashafrooz and Nargess Mehdipour. Many-body dissipative particle dynamics simulation of liquid–vapor coexisting curve in sodium. *Journal of Chemical & Engineering Data*, 61(10):3659–3664, 2016. doi:10.1021/acs.jced.6b00586.

[107] Pep Español and Mariano Revenga. Smoothed dissipative particle dynamics. *Phys. Rev. E*, 67:026705, Feb 2003. doi:10.1103/PhysRevE.67.026705.

[108] Sergey Litvinov, Marco Ellero, Xiangyu Hu, and Nikolaus A. Adams. Smoothed dissipative particle dynamics model for polymer molecules in suspension. *Phys. Rev. E*, 77:066703, Jun 2008. doi:10.1103/PhysRevE.77.066703.

[109] Marco Arienti, Wenxiao Pan, Xiaoyi Li, and George Karniadakis. Many-body dissipative particle dynamics simulation of liquid/vapor and liquid/solid interactions. *Journal of Chemical Physics*, 134(20), 2011. doi:10.1063/1.3590376.

[110] C. Vega and E. de Miguel. Surface tension of the most popular models of water by using the test-area simulation method. *The Journal of Chemical Physics*, 126(15):154707, 2007. doi:10.1063/1.2715577.

[111] Patrick B. Warren. No-go theorem in many-body dissipative particle dynamics. *Physical Review E - Statistical, Nonlinear, and Soft Matter Physics*, 87(4):13–14, 2013. doi:10.1103/PhysRevE.87.045303.

[112] J. A. Elliott, S. Hanna, A. M. S. Elliott, and G. E. Cooley. Interpretation of the small-angle x-ray scattering from swollen and oriented perfluorinated ionomer membranes. *Macromolecules*, 33(11):4161–4171, 2000. doi:10.1021/ma991113+.

[113] P. J. James, J. A. Elliott, T. J. McMaster, J. M. Newton, A. M. S. Elliott, S. Hanna, and M. J. Miles. Hydration of nafion studied by afm and x-ray scattering. *Journal of Materials Science*, 35(20):5111–5119, Oct 2000. doi:10.1023/A:1004891917643.